

Continuous Language Diffusion as a Decoder-Interface Problem

Zhicheng Du, Lan Ma

Tsinghua Shenzhen International Graduate School, Tsinghua University

June 8, 2026

Abstract

Gaussian-corrupted sentence embeddings have no direct linguistic interpretation, yet continuous diffusion language models can generate fluent text from them. We study this puzzle through Embedded Language Flows (ELF) and identify a decoder-basin mechanism: denoising succeeds when trajectories reach regions where the native decoder can read stable tokens. We introduce a diagnostic protocol for denoisability, semantic recoverability, order sensitivity, decoder compatibility, and trajectory reliability. It exposes failures hidden by scalar metrics: low mean-squared error can discard linguistic content, low perplexity can reflect low-entropy collapse, and clean latent reconstruction can coexist with a narrow decoder basin. A decoder-margin bound explains why token recovery depends on margin and local decoder sensitivity, not latent error alone. Auditing public ELF checkpoints reveals an interface phase diagram: early predictions are weakly readable, mid-trajectory disagreement marks a competition region, and late predictions enter a high-margin final-token basin. Once inside, token realization is surprisingly simple on generated ELF states: frozen T5 token-embedding lookup recovers 93–96% of native decoder decisions, and a single linear readout reaches 97.9% agreement at 32k samples, leaving about a 1.1 perplexity gap in a structured residual tail. A conservative margin gate exits 17–27% earlier in denoising steps under an explicit diagnostic monitor. Boundary checks on LangFlow, BitstreamDiffusion, and the Continuous Latent Diffusion Language Model (Cola-DLM) show that the same interface questions remain meaningful when the state object and decoder change. Continuous and latent diffusion language models should therefore be evaluated as representation-decoder systems.

1 Introduction

Unlike images, where noisy observations can preserve visible spatial structure, noisy sentence embeddings have no direct linguistic interpretation. So why does continuous diffusion work for language at all? Tokens are discrete, word order is combinatorial, and a Gaussian perturbation of contextual embeddings does not correspond to a readable partial sentence. Yet recent continuous and latent diffusion language models (DLMs) report strong generation quality and attractive parallel sampling behavior [44, 63]. Embedded Language Flows (ELF) [22] is a clean instance of this trend: it denoises in a frozen T5 (Text-to-Text Transfer Transformer) [51] embedding space and maps the final continuous state back to tokens through a nonlinear decoder implemented with shared weights.

This result raises the central question: if Gaussian noise in language embeddings is not linguistically meaningful, why does continuous denoising work? One explanation is the *network hypothesis*: the denoising Transformer learns language generation in a new continuous domain. Another is the *interface hypothesis*: the pretrained representation and its decoder already provide much of the recoverable structure, and the denoiser mainly learns how to traverse this interface over time. These hypotheses make different predictions. If the network is doing most of the work, removing capacity should destroy linguistic recoverability. If the interface matters, simple denoisers should recover some structure, but the recovery should fail in diagnostic ways that reveal what the interface preserves, what it discards, and where its compatibility boundaries lie. We treat the two hypotheses as complementary stress tests: low-capacity denoising and decoder probes stress the interface hypothesis, while trajectory audits measure the transport performed by the denoising network. The resolution is an *asymmetric cooperation*: after successful basin entry, the interface accounts for most final token decisions, but the network still performs the path-dependent transport that brings noisy continuous states into that readable region.

The interface hypothesis is tempting but incomplete. Smooth geometry alone is not enough: a covariance-matched Gaussian can be easy under mean-squared error (MSE) yet linguistically empty; token embeddings can decode while ignoring order; a latent variational autoencoder (VAE) [24] can reconstruct clean inputs yet expose a narrow noisy-latent decoder basin; and low external perplexity (PPL) can come from low-entropy text that disagrees with the native

interface. A diffusion-ready interface must therefore be denoisable, recoverable, order-sensitive, decoder-compatible, and accompanied by trajectory reliability signals.

This work is a controlled diagnostic study of existing checkpoints and interfaces. We remove model capacity with simple denoisers, audit public ELF trajectories, and use the Continuous Latent Diffusion Language Model (Cola-DLM) as a contrasting latent system whose clean reconstruction is strong but noisy decoder basin is narrow. ELF supplies the main mechanism evidence; LangFlow, BitstreamDiffusion, and Cola-DLM are boundary diagnostics rather than parallel benchmark claims. We therefore do not claim that ELF solves the self-bootstrapping problem for continuous language representations. Instead, we ask a more diagnostic question: given a strong pretrained interface, what property makes it usable for diffusion, and how can future learned interfaces be tested? The experiments converge on a “propose, compare, enter basin” view: the denoiser proposes continuous states, self-conditioning disagreement peaks in a middle region statistically consistent with candidate revision, and successful trajectories enter the native decoder’s high-margin basin before final tokenization. Here “compare” denotes an observed trajectory pattern, not a directly observed internal algorithm. The negative controls calibrate scope, but the contribution is positive: we provide a diagnostic protocol that reveals when common metrics validate the wrong object, identify decoder-basin navigation as a fixed-checkpoint mechanism across ELF samplers and model sizes, and turn basin variables into three minimal probes of timing, token alignment, and linear recoverability. Together, these results support an asymmetric division of labor: pretrained decoder geometry supplies a readable target region and determines most final token labels after entry, while the denoising network transports Gaussian states into that region.

Figure 1 outlines the argument. We make the ELF interface explicit (Section 3), define a diagnostic protocol (Section 4), apply it to representations, trajectories, probes, decoder calibration, and boundary systems (Section 5), and discuss implications for future DLM design (Section 6).

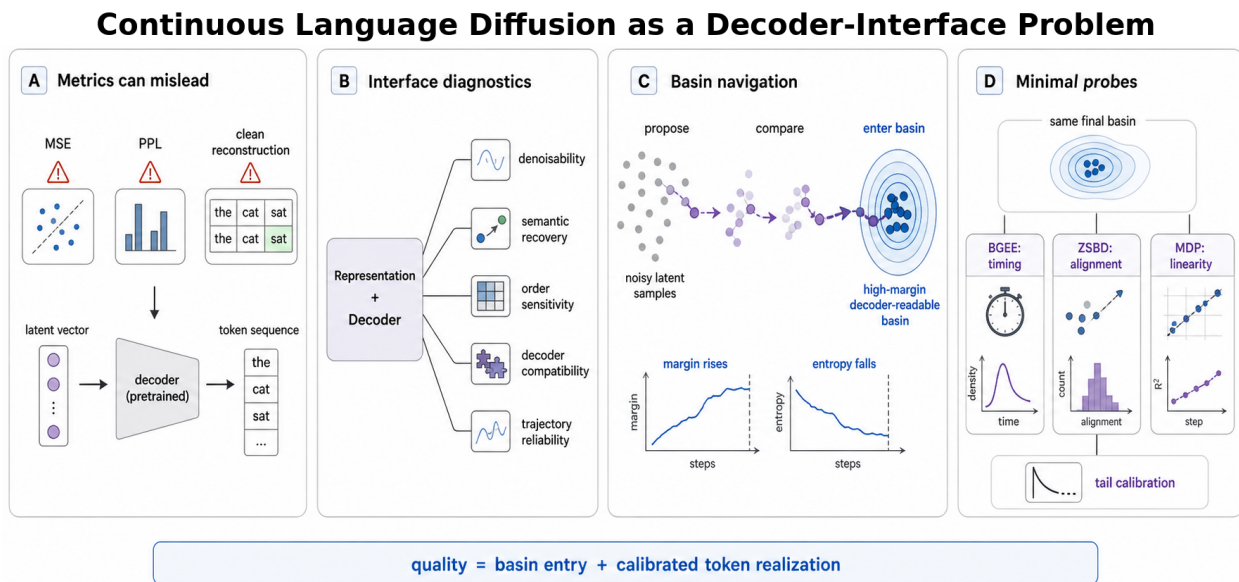


Figure 1: Continuous language diffusion as an interface problem. Unlike noisy images, noisy sentence embeddings do not retain an obvious linguistic interpretation. We therefore diagnose the representation–decoder interface along multiple axes, view denoising as a propose/compare/enter-basin process, and show why MSE, PPL, and clean reconstruction can each be misleading in isolation. The axes are diagnostic measurements, not a claim that any single axis causally determines generation quality.

Contributions.

1. We introduce a diagnostic protocol for continuous and latent DLM interfaces, separating denoisability, semantic recoverability, order sensitivity, decoder compatibility, and trajectory reliability. Its sensitivity is demonstrated through a principal component analysis (PCA) bottleneck failure: variance can be preserved while decoder margins and generation diversity collapse.
2. We provide a theoretical account of why common metrics mislead: linear MSE denoising is governed by second-order statistics, while token recovery depends on decoder margins relative to local Jacobian sensitivity (Theorem 1).

3. We show that ELF denoising trajectories exhibit *basin navigation*—margin grows over denoising time, the delta-margin relation changes sign around basin entry, and the entry phase shifts earlier with model scale. We summarize this as an empirical interface phase diagram with pre-entry, competition, and locked regions. The phenomenon persists across stochastic differential equation (SDE) and ordinary differential equation (ODE) samplers, while preliminary boundary checks expose related interface questions in LangFlow [8] and bitstream diffusion [4].
4. We convert the diagnostic into three minimal probes of the same basin. “Minimal” here means minimal new modeling machinery, not identical computational cost. Basin-Guided Early Exit (BGEE) exits 17–27% earlier in denoising steps under conservative held-out gates and an explicit monitoring caveat. Zero-Shot Basin Decoding (ZSBD) recovers 93–96% of the native decoder’s token decisions with no newly trained readout but with the frozen T5 token-embedding table. The Minimal Decoder Protocol (MDP) reaches 97.9% agreement on generated final ELF states at 32k samples, suggesting that the native decoder’s remaining role on this generated manifold is concentrated in tail calibration rather than bulk token realization.
5. We add mechanism stress tests around the probes: cross-decoder decoding within the ELF family, paired basin/anti-basin trajectory interventions, token-wise basin-entry timing, ZSBD geometry ablations, residual-tail targeting, and long-form coherence boundary checks. These tests sharpen the boundary of the central claim without recasting the probes as standalone methods.

2 Related Work

Continuous diffusion language models. Diffusion language models began largely in discrete or masked-token spaces [3], where the state can be interpreted as a partially corrupted token sequence. Early continuous and simplex-based language diffusion systems, including Diffusion-LM, DiffuSeq, SSD-LM, and latent language diffusion [16, 18, 33, 37], showed that iterative denoising can be adapted to text generation and control, while later masked diffusion work such as MDLM and scaled masked DLMs [43, 55] improved the discrete-token recipe. Continuous DLMs move the corruption process into an embedding or latent space instead. Because this area is moving quickly, several 2025–2026 references below are recent arXiv preprints; we cite them for positioning and convergent evidence, not as settled benchmark consensus. ELF [22] performs flow matching in a frozen T5 [51] contextual embedding space and discretizes only at the final step [35]. This design is intentionally close to the image diffusion recipe [21]: stay continuous during denoising, then decode once. It also makes ELF an especially clean interface test: the representation space is supplied by a pretrained encoder rather than bootstrapped end to end, so the central question becomes why this fixed representation–decoder pair is diffusion-ready. Cola-DLM [17] makes a different choice: it learns a compact Text VAE and trains a block-causal diffusion Transformer (DiT) [47] prior over VAE latents. TextLDM [23] similarly imports latent diffusion ingredients into text, including alignment and latent modeling components. Bitstream diffusion [4] explores another route by removing the $\mathcal{O}(V)$ vocabulary bottleneck and using entropy-gated continuous bitstreams. Tooling work such as dLLM [70] reflects the same trend toward reproducible DLM training and evaluation. These systems agree that non-autoregressive denoising can be useful for language, but they leave open a more basic question: what property of the state space makes it useful, and when does the decoder become the bottleneck?

Recent work also tries to remove the frozen-interface limitation rather than only analyze it. Latent Diffusion Language Model (LDLM) [40] jointly trains a latent encoder, diffusion prior, and decoder, and reports that decoder-input noise, MSE decoder loss, warmup, and adaptive timestep sampling are all important for robust latent diffusion. DiHAL [26] asks where diffusion should enter a pretrained transformer, using geometry-based layer scores and hidden-state replacement to avoid direct token-level recovery. RePlaid [64] shows that likelihood-trained continuous diffusion can scale competitively with discrete diffusion when the architecture and training protocol are modernized, while DiLaDiff [30] adds a distilled latent-augmented prior to accelerate masked diffusion language modeling. The Flow Map Language Models (FMLM) work [29] studies flow-map distillation toward one-step language generation, while Categorical Flow Maps and their scaled variants [10, 54] show that Gaussian-to-categorical flow maps can reach few-step text generation at much larger scale. Consistent Diffusion Language Models (CDLM) [1] adapt consistency ideas to discrete diffusion through multi-path training. Coevolutionary Continuous-Discrete Diffusion (CCDD) [69] argues that continuous diffusion has strong expressive power but that practical trainability and token decoding remain obstacles. Together, these papers provide convergent evidence that the central difficulty is not simply “continuous versus discrete”, but how the latent state, prior dynamics, and token realization are made compatible. Table 1 summarizes this literature through the interface lens used in this paper: each family exposes a different part of the state–decoder

compatibility problem, and only ELF supplies the fixed-checkpoint trajectory needed for our time-resolved basin audit.

Table 1: Related systems viewed through the representation–decoder interface. The table is not a benchmark comparison; it separates which part of the interface problem each line primarily exposes and how it is used in this diagnostic study.

Work family	Interface question	Role in this paper
Discrete or masked DLMs [3, 43, 55]	Token or mask states avoid Gaussian hidden-state corruption, but logits still cross a token boundary.	Background for trajectory reliability and PPL-only evaluation pitfalls.
Early continuous or latent DLMs [16, 18, 33, 37]	Embeddings, simplex states, or latents can be denoised, but often need per-step token losses, rounding, or a separate decoder.	Motivates separating denoisability from decoder compatibility.
ELF [22]	Frozen T5 contextual states plus a shared native decoder define a clean fixed interface.	Main testbed for time-resolved decoder-basin entry, scale/sampler audits, and minimal probes.
Learned or co-evolved latent interfaces [17, 23, 40, 64]	Clean reconstruction or latent alignment may not imply robustness under the prior’s noisy states.	Boundary and convergent evidence for evaluating learned representations by basin width, not reconstruction alone.
Alternative native interfaces [4, 8]	Latent-step margins and bit-level recovery use different native units from ELF’s T5 decoder.	External checks showing that the same diagnostic questions remain meaningful without claiming benchmark rank.
Decoder-bottleneck and representation-first views [5, 56, 66]	Final projection, decoder readability, or tokenizer geometry can dominate what downstream generation can recover.	Closest conceptual context; this paper adds fixed-checkpoint, time-resolved basin diagnostics and BGEE/ZSBD/MDP probes.

Latent interfaces and decoder bottlenecks. In image latent diffusion, the decoder maps continuous latents to pixels, and small pixel-level errors often remain visually tolerable [53]. Text is different. The decoder crosses a discrete boundary, so local changes in latent space can abruptly change token identity, syntactic role, or lexical frequency. CoDAR [56] studies this issue from an architectural angle, identifying token rounding and final projection as bottlenecks and replacing the final projection with a contextual autoregressive (AR) decoder. Our work studies the same broad interface problem from a diagnostic angle. We do not introduce a stronger decoder; we ask how to measure whether a representation and native decoder are already compatible, how PPL can be misleading, and whether the denoising trajectory exposes reliability before decoding. Our decoder calibration and Cola-DLM boundary experiments are motivated by this difference. They ask whether a low reconstruction error, low PPL, or clean latent recovery actually indicates that the prior is handing states to the decoder in the right region.

A contemporaneous technical report by Zhang [66] studies a related decoder-readability failure mode from another angle. Its setting is draft-conditioned latent refinement with a frozen BERT [12] encoder on ROCStories [42]: a draft latent is refined by a DraftPrior, FlowNet, and MetricNet, and the report observes that high latent cosine similarity need not yield reliable token distributions. It provides supporting context but covers a narrower slice of the problem studied here. It does not audit released ELF checkpoints, full denoising from Gaussian noise, native-margin basin entry over time, cross-scale/sampler phase diagrams, or the residual-tail structure after entry. Our contribution is diagnostic and time-resolved: we define decoder-basin entry through native margins, measure when ELF trajectories enter that basin, and test what becomes simple after entry through BGEE, ZSBD, and MDP.

Several recent results in vision suggest that generative modeling depends strongly on representation geometry. REPA aligns diffusion Transformer representations with pretrained encoders to make training easier [65]. Dispersive regularization improves image generation by shaping hidden representations [60]. Noise-conditioning ablations and masked-autoencoding-style simplification studies challenge assumptions that once seemed necessary [58]. Drifting Models [11] go further by moving iterative distribution evolution from inference to training, naturally yielding one-step generation. These studies share a methodological pattern: simplify the system, identify which representation property matters, and then strip away machinery only when the evidence supports it. Our work follows that representation-first pattern for language diffusion, but with an additional decoder-margin issue created by discrete tokenization.

Contextual representation geometry. The geometry of contextual language representations is itself highly structured. Prior analyses show that contextual embeddings are anisotropic and occupy narrow regions of representation space rather than behaving like isotropic semantic vectors [13]. This background motivates, but does not settle, our controls. A covariance spectrum can make denoising easy under MSE, while whitening or covariance matching can preserve second-order structure without preserving linguistic recoverability. Our diagnostic therefore treats covariance and anisotropy as possible confounders to control, rather than as explanations by themselves.

Recent theory also gives a complementary reason to care about latent prediction itself. Korchinski et al. [27] show in a hierarchical grammar model that predicting learned latents can recover hidden compositional structure with far fewer samples than token-level prediction. Our experiments are not a sample-complexity proof, but they add a practical constraint to this latent-first view: a latent can be statistically useful and still fail if the denoising trajectory does not enter the native decoder’s basin.

TokenOpt [5] provides a useful analogy from vision: a highly compressed 1D image tokenizer can support generation and editing through simple test-time token manipulations, without training a generative model. The lesson is not that language should copy the same pipeline, but that a good tokenizer or representation can make a crude downstream procedure powerful. Our BGEE, ZSBD, and MDP experiments follow the same diagnostic-to-minimal-probe philosophy in a different domain. They are three probes of one object, the decoder basin: BGEE measures when the trajectory reaches it, ZSBD asks whether final states align with token-embedding Voronoi cells, and MDP asks whether the native token decisions are locally linearly recoverable on the generated-state manifold. The resulting procedures are intentionally modest. Their role is not to define standalone decoding methods, but to expose what the representation-decoder interface has already made easy for a cheap downstream readout.

Representation alignment work shows that pretrained autoregressive models can be adapted to diffusion-style generation without full retraining [48]. This supports the broader idea that existing language representations contain useful structure for non-autoregressive generation. However, reusing a representation is not the same as validating an interface. A representation can be aligned with a source model while still being hard for a target decoder to recover from noisy states. Our diagnostic protocol is therefore complementary: it can be used before training to decide whether a proposed encoder, tokenizer, or VAE latent is a plausible state space for diffusion.

Classifier-free guidance [20], entropy-aware reward guidance [59], and progress-aware policies such as Prophet, SchED, Fast-dLLM, Just on Time, DAWN, DMax, AHD, Dystruct, locally coherent parallel decoding, and DCDM [9, 19, 25, 32, 39, 41, 57, 63, 71, 72] all exploit the fact that diffusion trajectories contain information before the final output. These works often optimize inference behavior directly through confidence thresholds, token freezing, dependency-aware unmasking, history-stable decoding, dynamic structure, semantic chunking, or cache-aware parallel decoding. Our trajectory-reliability experiments are narrower: we ask whether internal signals from the existing checkpoint predict final sample quality and whether a small time-region intervention validates the signal. This distinction matters because an optimized sampler can improve metrics without explaining why a representation-decoder interface works.

The PPL illusion in diffusion language models. Generated-text PPL (Gen. PPL) has known failure modes in diffusion language modeling. In discrete masked diffusion, Zheng et al. [68] show that masked diffusion training and sampling can be interpreted as time-agnostic masked modeling, and identify a numerical issue in Gumbel-based categorical sampling: finite-precision truncation effectively lowers sampling temperature, reducing diversity and making PPL-only comparisons unfair. Our setting is different, but the warning is the same. A continuous or latent DLM can also obtain low PPL by moving into a low-entropy decoder region, by repeating high-frequency text, or by changing calibration at the final token boundary. The common structure is that a single scalar can indicate fluency while hiding diversity, fidelity, or interface failure. This is why our evaluation pairs PPL with entropy, repetition, MAUVE score (for measuring the gap between neural and human text distributions) [49], Jensen-Shannon (JS) divergence [34], decoder agreement, and margin recovery.

AR-integrated diffusion and self-speculation. Nemotron-Labs-Diffusion [14] unifies autoregressive, diffusion, and self-speculation decoding in a single model. Such systems may blur the line between AR and diffusion language modeling, but they do not remove the need for diagnostics. If diffusion becomes an operating mode inside a larger model, one still needs to know when the diffusion state is reliable, when a decoder or verifier is calibrated, and which objective frontier is being optimized. Our results suggest a useful future audit for tri-mode models: test whether their diffusion branch exposes similar trajectory-reliability signals and whether their speculative decoder has a broad or narrow decision basin.

Mechanistic diagnostic studies. Recent work on transformer internals, such as the finding that adjacent layers systematically correct each other’s predictions [46], demonstrates the value of diagnostic studies: identify a surprising phenomenon, rule out trivial explanations, localize where and when it appears, and synthesize the evidence into a compact mechanism. Closest to our trajectory analysis, Lu [38] measures when token commitment, linguistic probes, confidence, entropy, and re-masking sensitivity emerge in LLaDA [44] trajectories. Our study asks a complementary interface question in continuous ELF-style latents: when does the trajectory enter a decoder-readable basin, and what does the native decoder still contribute after entry? What the above work leaves open is not which sampler or architecture is best, but a simpler diagnostic question: does the denoising trajectory enter a decoder-readable basin, and

how would we know? We next make the ELF interface explicit and turn that question into a measurable protocol.

3 Preliminaries: The ELF Interface

ELF is a useful testbed because it separates the continuous state space from the final token decision. For a token sequence y , a frozen T5 encoder produces contextual clean states $x = E(y)$. Flow matching trains a denoiser to recover x from Gaussian-corrupted states,

$$z_t = tx + (1-t)\varepsilon, \quad \varepsilon \sim \mathcal{N}(0, I).$$

At inference time, the sampler starts from noise, repeatedly predicts clean states \hat{x}_t , and maps the final state to token logits through ELF’s native decoder. In the released PyTorch checkpoints, this decoder is not a bare unembedding matrix; it is a learned nonlinear readout implemented with shared model weights.

We use three decoder-facing objects throughout the paper. The *native decoder* is the trained ELF readout just described, or the corresponding trained decoder for another state space such as Cola-DLM. The *token-embedding lookup* used by ZSBD is different: it is a nearest-neighbor rule in the frozen T5 token-embedding table with no newly trained readout and is used only as a geometry probe. This lookup is not prior-free: it uses the labeled T5 token table tied to ELF’s own interface. The *MDP readout* is a learned token-wise linear classifier trained after generation to imitate the native decoder’s argmax labels on generated final states. Keeping these objects separate is important: BGEE monitors the native decoder margin, ZSBD tests token-embedding alignment, and MDP measures how linearly recoverable the native decision boundary is on the generated-state manifold.

This interface view matters for our diagnostics. A predicted clean state can be close to the target under MSE while still lying outside the decoder’s decision basin. Conversely, a state can be easy to decode while preserving little diversity or order information. Continuous language generation is therefore a question of interface compatibility: the representation must carry linguistic structure, the trajectory must transport noisy states into the decoder basin, and the decoder must assign stable token decisions once the trajectory arrives. The next section decomposes this compatibility into five measurable axes that together define a diagnostic protocol for evaluating candidate state spaces.

4 Diagnostic Protocol

4.1 Five Axes of Readiness

Given the interface above, we evaluate the representation-decoder interface along five axes. For a clean representation x and ELF-style corruption

$$z_t = tx + (1-t)\varepsilon, \quad \varepsilon \sim \mathcal{N}(0, I),$$

we use the following tests. These axes are not assumed to be independent. In practice they can trade off against one another: denoisability and decoder compatibility are connected through margins, and semantic recoverability often changes together with order sensitivity. The protocol identifies which axis becomes the bottleneck for a proposed state space rather than reducing the axes to a single score.

Denoisability asks whether x can be recovered from z_t under simple denoisers. We fit scalar, diagonal, low-rank, and full linear maps and report normalized MSE (NMSE) and cosine similarity. The denoisers are intentionally weak: if a finding requires a large Transformer, it cannot isolate the state-space geometry.

Semantic recoverability asks whether linguistic attributes remain accessible after corruption and recovery. We use token recovery, semantic cosine similarity, and lightweight attribute probes. These probes are not meant to solve language understanding; they test whether a denoised state still carries information that a simple classifier can read.

Order sensitivity asks whether contextual states distinguish real text from word-shuffled controls. This axis is important because a token embedding matrix can be easy to decode while ignoring contextual order. A continuous DLM that relies on contextual embeddings should fail when the same tokens are presented in a shuffled order.

Decoder compatibility asks whether the state remains safely decodable by its intended native decoder. We use *basin* operationally, not as an undefined geometric metaphor. For decoder logits $g(h) \in \mathbb{R}^V$ and token i , define the token margin

$$m_i(h) = g_i(h) - \max_{j \neq i} g_j(h),$$

and the margin- τ decoder basin for token i as the super-level set

$$\mathcal{B}_{i,\tau}(g) = \{h : m_i(h) \geq \tau\}.$$

For a decoded sequence $y = (y_1, \dots, y_L)$, we summarize basin entry by lower-tail statistics of $\{m_{y_\ell}(h_\ell)\}_{\ell=1}^L$, especially the 10th-percentile margin. This definition does not assume the set is convex, bounded, or shared across architectures; it is a measurable proxy for local decoder stability. We measure token agreement to the native decoder, decoder entropy, margin under latent corruption, and calibration against small learned decoders. Nearest-neighbor token lookup is reported separately as a frozen-embedding alignment probe with no newly trained readout, not as the native basin definition.

The later probes are not alternative definitions of the same mathematical set. BGEE uses the margin super-level set above to measure native decoder stability. ZSBD asks whether states inside that region are also close to labeled T5 token-embedding Voronoi cells. MDP asks whether the native decoder’s labels are locally linearly recoverable on the generated-state manifold. These probes are related because they are all decoder-facing, but they are not equivalent. We use *basin navigation* as shorthand for trajectories entering a high-margin native-decoder region, while reporting the other two probes as geometric shadows of that entry in the token-embedding Voronoi space and on the linear-readout manifold.

This margin-based basin is also high-dimensional and anisotropic. The sufficient radius in Theorem 1 is local and direction-agnostic only because it uses a worst-case Lipschitz constant. Directional reverse-basin navigation (RBN) later shows that random, sentiment, PCA, and decoder-gradient directions have very different effective sensitivities. Thus “wide basin” should never be read as a spherical low-dimensional picture; it is a decoder-margin super-level set intersected with the generated-state manifold.

Trajectory reliability asks whether the denoising trajectory exposes signals correlated with its final outcome. For ELF we record self-conditioning delta, agreement with zero-self-conditioned predictions, decoder entropy, and effective-rank proxies over time. These signals are correlated with final sample quality and then perturbed through shuffled, delayed, clipped, and reversed-time controls. We call them reliability signals rather than certificates: they are useful diagnostics under the reported metrics, not formal guarantees and not a substitute for task or human evaluation.

Protocol. The protocol follows a fixed order. First, remove capacity by fitting simple denoisers on candidate spaces and controls. Second, add decoder-facing tests, because a low-MSE state may still cross token boundaries. Third, audit the real model trajectory and test whether internal signals predict final quality. Fourth, only after the above signals are present, apply a minimal inference intervention. This order prevents a sampler result from being mistaken for a mechanism.

Controls. Each axis uses controls that preserve one property while breaking another:

- *Covariance-matched Gaussian* preserves first- and second-order statistics while removing linguistic content.
- *Whitened contextual embeddings* test whether recovery depends on anisotropy rather than semantic organization.
- *Token-shuffled contextual embeddings* preserve the multiset of words while breaking order.
- *Sequence-shuffled embeddings* preserve marginal embedding statistics while mismatching text and representation.
- *Random T5 controls* preserve architecture and dimensionality while removing pretrained geometry.

These controls are essential because many plausible explanations are too broad: a result that vanishes when the easy statistical property is preserved but the linguistic property is removed is a result that isolates the right mechanism.

Readiness scores. We avoid collapsing the axes into a single score in the main text, but internally each axis can be written as a normalized diagnostic. Denoisability is $1 - \text{NMSE}$ under a fixed denoiser family. Recoverability is a probe or nearest-neighbor recovery score relative to clean states. Order sensitivity is the gap between real and shuffled inputs. Decoder compatibility is the fraction of tokens whose native-decoder margin remains positive under corruption. Trajectory reliability is the absolute Spearman correlation between an internal trajectory statistic and final quality under permutation controls. Reporting the vector is more informative than reporting the mean, because the failure modes are qualitatively different and a collapsed score can hide which specific axis has broken.

4.2 Why MSE Is Not Enough

Our linear diagnostic is simple on purpose: it separates geometry from model capacity. That same simplicity exposes why MSE can mislead.

Proposition 1 (Linear MSE denoising is second-order). *Let x and ε be zero-mean independent random vectors with covariances Σ_x and I . For $z_t = tx + (1-t)\varepsilon$, the population-optimal linear MSE denoiser $A^* z_t$ is*

$$A^* = t\Sigma_x (t^2\Sigma_x + (1-t)^2I)^{-1}.$$

The proof follows from the normal equations: $A^* = \mathbb{E}[xz_t^\top] \mathbb{E}[z_t z_t^\top]^{-1}$, with $\mathbb{E}[xz_t^\top] = t\Sigma_x$ and $\mathbb{E}[z_t z_t^\top] = t^2\Sigma_x + (1-t)^2I$. Thus a space can be easy to linearly denoise because of its covariance spectrum, even if the recovered state contains little linguistic information. This is the reason our diagnostic always pairs MSE with semantic, order, and decoder tests.

4.3 Decoder Compatibility as a Basin Property

Token decoding is a margin problem. Let a decoder choose token i when logit $g_i(h)$ exceeds all alternatives. A perturbation δ preserves the token only if

$$g_i(h + \delta) - g_j(h + \delta) > 0 \quad \forall j \neq i.$$

For a locally linear decoder this margin is controlled by $(w_i - w_j)^\top \delta$; for a nonlinear decoder the same idea holds locally through the Jacobian. This gives a simple bound.

Theorem 1 (Decoder margin bound). *Let $g : \mathbb{R}^d \rightarrow \mathbb{R}^V$ be a differentiable decoder logit map, and let $i = \arg \max_k g_k(h)$. Define the clean margin*

$$m(h) = \min_{j \neq i} (g_i(h) - g_j(h)).$$

Assume that in a neighborhood of h , every pairwise margin function $g_i - g_j$ is $L(h)$ -Lipschitz. Then any perturbation δ with $\|\delta\|_2 < m(h)/L(h)$ preserves the decoded token. If δ is random, then

$$\Pr[\text{decode}(h + \delta) \neq i] \leq \Pr\left[\|\delta\|_2 \geq \frac{m(h)}{L(h)}\right].$$

For isotropic $\delta \sim \mathcal{N}(0, \sigma^2 I_d)$, this becomes

$$\Pr[\text{change}] \leq \Pr\left[\chi_d^2 \geq \left(\frac{m(h)}{L(h)\sigma}\right)^2\right].$$

Proof. For any $j \neq i$, Lipschitz continuity gives

$$(g_i - g_j)(h + \delta) \geq (g_i - g_j)(h) - L(h)\|\delta\|_2.$$

If $\|\delta\|_2 < m(h)/L(h)$, every pairwise margin remains positive, so token i remains the argmax. The probability bound follows by taking the complement of this deterministic sufficient condition. The Gaussian statement follows from $\|\delta\|_2^2/\sigma^2 \sim \chi_d^2$. \square

Theorem 1 explains why decoder compatibility is not reducible to MSE. Two states with the same latent error can have different recovery probabilities if their margins or local Jacobians differ. It also motivates a measurable diagnostic: as a final latent is corrupted away from the decoder-compatible basin, positive-margin fraction and token recovery should collapse together. We test exactly this in Section 5.11. The bound is intentionally local and sufficient rather than a tight decoder theory: we do not estimate the full local Lipschitz spectrum of ELF’s nonlinear decoder, and the isotropic Gaussian form ignores the anisotropy measured later. Its role is qualitative and diagnostic. It identifies the variables a decoder-basin analysis must measure—margin, local sensitivity, and perturbation scale—rather than providing a calibrated probability model for ELF’s contextual decoder.

A small Euclidean error can therefore cross a decoder boundary, while a learned decoder can obtain low PPL by moving to a low-entropy high-frequency region. Decoder compatibility is a basin and calibration property, not simply reconstruction loss.

From local basin to interface transition. The margin bound is pointwise, but a diffusion trajectory is dynamic. For any decoder-facing signal $q(\tau)$ measured along normalized denoising phase $\tau \in [0, 1]$, define the crossing phase

$$\tau_q(a) = \inf\{\tau : q(\tau) \geq a\}.$$

For an agreement-like signal, such as ZSBD agreement to the native decoder, we define a transition width

$$W_q(a, b) = \tau_q(b) - \tau_q(a), \quad a < b,$$

and an empirical entry sharpness $S_q(a, b) = (b - a)/W_q(a, b)$ when the width is positive. For margin signals, the same definition applies with thresholds such as $m = 2$ and $m = 8$. These quantities do not assert a thermodynamic phase transition. They turn basin entry into measurable timing variables: when token alignment begins, how long the competition region lasts, and how abruptly the trajectory becomes decoder-stable.

Proposition 2 (Corrupted-latent cross-entropy applies local margin pressure). *Consider a decoder with logits $g(h)$ trained by cross-entropy (CE) loss on a latent h and correct token i . The gradient in logit space increases $g_i(h)$ and decreases competing logits in proportion to their softmax probabilities. If training includes corrupted latents $h + \delta$ sampled from a neighborhood of the clean state, then the same update is applied throughout that neighborhood. Consequently, decoder-side corruption training applies margin-increasing pressure not only at h , but on the latent region through which the prior or denoiser is expected to pass.*

Proposition 3 (Dispersion increases a prototype decoder basin). *Consider a nearest-prototype decoder with token prototypes $\{\mu_k\}$ and logits $g_k(h) = -\|h - \mu_k\|_2^2$. If h is assigned to token i , then the margin against j is*

$$g_i(h) - g_j(h) = \|\mu_j - \mu_i\|_2^2 - 2(h - \mu_i)^\top (\mu_j - \mu_i).$$

For latents h in a fixed radius around μ_i , and when prototype separation is larger than that local radius, increasing the pairwise separation $\|\mu_j - \mu_i\|_2$ increases a lower bound on the margin and therefore enlarges the sufficient recovery radius in Theorem 1.

This simplified prototype is not intended as a literal model of ELF’s nonlinear decoder. It serves as a geometric bridge: dispersing token-conditioned representations can widen local decision basins when the representation remains near the correct prototype, while collapsed representations make small latent errors more likely to cross token boundaries. The connection to the margin bound suggests a training principle: decoder branches should apply margin-increasing pressure on plausible noisy latents, not only reconstruct clean ones. ELF’s mixed denoising/decoding training and LDLM’s decoder-input noise [40] can both be read in this light. The open question is how to widen the basin without encouraging low-entropy collapse.

SDE noise as basin exploration. Theorem 1 also gives a geometric interpretation of SDE gamma. Larger stochasticity increases the effective perturbation scale σ , which can lower token recovery probability if the trajectory is already inside a high-margin basin. But extra noise can also help escape a wrong low-margin basin before final decoding. This creates an exploration–exploitation trade-off: gamma is not merely a numerical sampler knob; it changes how often the trajectory crosses decoder boundaries. This is why we pair gamma and guidance sweeps with entropy, repetition, and MAUVE rather than relying on PPL as the sole quality indicator.

4.4 Trajectory Reliability Signals

We audit the released ELF checkpoints through the official PyTorch implementation, without modifying checkpoint weights or source behavior. During sampling we record self-conditioning (SC) delta, agreement with zero-self-conditioned predictions, decoder entropy, layer-similarity proxies, and effective-rank proxies. For each generated sample we then compute GPT-2-Large [50] PPL and correlate internal trajectory summaries with final quality. These signals are not used to train a new model; they test whether the model exposes when its own trajectory is reliable.

Signal controls. Following the logic of mechanistic diagnostic studies, we do not stop at a positive correlation. We perturb the proposed signal in three ways. A *delayed* signal uses the same values but shifts them to the wrong time region. A *clipped* signal removes its dynamic range. A *random* signal preserves the marginal distribution but breaks the sample-trajectory association. We also compare front-loaded and back-loaded schedules to test whether the useful region is temporally localized.

Why not learn a policy directly. It is natural to ask whether trajectory signals could be fed into a learned policy that adjusts guidance strength or step allocation. We avoid this path on purpose. A learned policy would conflate three separate questions: whether the signal carries information, whether the policy class is adequate, and whether the reward is well-specified. Our approach separates them. We first verify that the signal predicts quality, then test localization with a hand-designed schedule. Learning an optimal policy is a natural next step, but it belongs after the diagnostic evidence has been established.

4.5 Basin-Navigation Audit

Trajectory-reliability correlations say that a trajectory exposes useful signals, but not what the signal means. We therefore add a decoder-facing trajectory audit. At every SDE step, we decode the predicted clean latent \hat{x}_t through the native ELF decoder and record top-1-vs-top-2 margins, decoder entropy, and the token-level self-conditioning disagreement

$$\Delta_t(i) = \frac{\|\hat{x}_{t,i}^{\text{SC}} - \hat{x}_{t,i}^0\|_2}{\|\hat{x}_{t,i}^{\text{SC}}\|_2 + \epsilon}.$$

At selected steps we also compare the intermediate argmax tokens with the final decoded sequence and compute the margin of those final tokens under the intermediate decoder logits. This distinguishes three questions: whether an intermediate state is readable by the decoder, whether it agrees with the final sequence, and whether it lies inside the final-token margin basin. The audit is still training-free; it is a mechanism probe for the existing checkpoint.

5 Experiments

Experiment roadmap. The experiments are organized as a causal reading path rather than as independent ablations. First, representation diagnostics show why denoisability, semantics, order, and decoder compatibility must be measured together (Section 5.1–Section 5.3; Figure 2–Figure 5). Second, trajectory and layer-wise basin audits show that ELF states move into a high-margin native decoder basin, expose phase-dependent reliability signals, and depend on the exact decoder-facing layer/interface (Section 5.4–Section 5.8; Figure 6–Figure 18). Third, a small schedule intervention, three minimal basin probes, and fixed-checkpoint stress tests ask where the measured basin variables are actionable and where their explanatory boundary lies, including long-form coherence (Section 5.9–Section 5.10; Figure 19–Figure 36; Table 5). Finally, multi-metric calibration, Cola-DLM boundary tests, and short training ablations rule out PPL-only, clean-reconstruction-only, and clean-decoder-only explanations (Section 5.11–Section 5.14; Figure 37–Figure 41, with training curves in Figure S19–Figure S23). Table 2 summarizes the evidence level and sample scale for each group.

Models and data. We evaluate the public ELF-B, ELF-M, and ELF-L checkpoints on OpenWebText (OWT) [15] generation. ELF-B and ELF-M provide the main diagnostic coverage; ELF-L is used for scale confirmations with smaller batches. We use T5 [51] contextual embeddings, T5 token embeddings, random T5 controls, BERT [12], RoBERTa [36], GPT-2 [50], Gaussian/covariance controls, and Cola-DLM VAE latents for representation diagnostics. Yelp Polarity and AG News [67] provide lightweight semantic probes. GPT-2-Large [50] is used for Gen. PPL to remain comparable with ELF and related DLM papers, not because it is a complete evaluator of 2026-level coherence or reasoning. OWT reference samples are used for JS divergence and MAUVE [49].

Why these controls. The controls are chosen to isolate different claims. Gaussian and covariance-matched Gaussian controls test whether MSE recovery is explained by second-order statistics alone. Token-shuffled and sequence-shuffled contextual embeddings test whether contextual order matters beyond token identity. T5 token embeddings test a decoder-friendly but non-contextual interface. BERT, RoBERTa, and GPT-2 test whether the phenomenon is specific to T5-style span-corruption pretraining or appears across encoder and decoder families. Cola-DLM tests a learned VAE latent interface rather than a frozen pretrained embedding interface.

Metrics. We report Gen. PPL because it is the standard ELF metric, but we never treat it as a complete objective. We pair it with unigram entropy, distinct/repetition statistics [31], JS divergence to reference token distributions, MAUVE [49], token agreement, decoder logit entropy, and margin recovery under latent corruption. For the long-form boundary audit, we additionally compute adjacent- and first-to-last sentence cosine with a sentence-embedding model [52]. This multi-metric design is necessary because many of our negative results are metric failures: a method can improve one scalar while degrading the property the scalar was meant to measure.

Hardware and scope. All experiments use a workstation with four graphics processing units (GPUs), each with 24 GB memory. ELF-B and ELF-M trajectory audits and decoder diagnostics run with moderate batch sizes; ELF-L is used for smaller-batch scale confirmations, including the two-seed trajectory-reliability check. This setup reflects the central premise: the diagnostic protocol is designed to be cheap enough to run before committing large-scale training.

Sample counts differ by experimental role. Mechanism audits use hundreds of generated sequences with per-token or per-step statistics; trajectory-reliability and schedule experiments use multiple 1024-sample seeds; MDP uses up to 32k generated final states because it estimates a readout on the generated-state manifold. Each subsection reports its

own sample count, and Table 2 separates fixed-checkpoint diagnostics, minimal probes, short training ablations, and external boundary checks.

Table 2: Experiment scale and claim level. Sample counts differ because the experiments answer different questions: mechanism audits need per-step or per-token statistics, readout probes need many generated final states, and external systems are used only as boundary diagnostics.

Claim level	Main evidence	Scale reported	Intended use
Representation readiness	T5 contextual/token, BERT, RoBERTa, GPT-2, Gaussian controls, Cola VAE latents, and PCA rank sweep	held-out OWT latent subsets; five PCA ranks; semantic probes on Yelp Polarity/AG News	diagnose candidate state spaces before relying on a denoiser
Trajectory reliability	trajectory signals correlated with GPT-2-Large log PPL; shuffled and time-region controls	ELF-B/M: three 1024-sample seeds; ELF-L: two 512-sample seeds	test whether checkpoints expose reliability signals
Basin-navigation mechanism	step-wise margin, entropy, self-conditioning delta, final-token agreement, and shard standard errors of the mean (SEM)	ELF-B 32-step SDE: 512 samples; B/M/L and ODE/SDE confirmations: 512 samples per run	fixed-checkpoint mechanism evidence, not a training-seed scaling law
Minimal probes and stress tests	BGEE, ZSBD, MDP, RBN, same-start path selection, and long-form topic boundary	BGEE: 512 ELF-B and 256 M/L confirmations; ZSBD: 4k B/M/L plus 8k/16k ELF-B checks; MDP: 1k–32k ELF-B saturation and 1k/4k M/L confirmations; RBN: 1024 ELF-B plus cross-scale confirmations; topic audit: 1000 texts per main group plus 512 ODE32 samples	measure timing, token alignment, linear recoverability, final-basin robustness, and discourse-level boundary cases
Training ablations	decoder-noise, decoder-branch frequency, and margin-loss variants in the official PyTorch ELF-B implementation	short 5k/10k runs on four RTX 3090 GPUs; 1024-sample basin sweeps	mechanism-side training evidence, not a final recipe
External boundaries	Cola-DLM VAE/DiT, LangFlow, and BitstreamDiffusion checks	Cola DiT: 512 samples per guidance value; Bitstream: structured proxy plus 512 real-code subset; LangFlow: small trajectory audits	show interface questions beyond ELF, not benchmark ranking

Evaluation order. The experimental order mirrors the diagnostic logic of the paper. We first test representations without the ELF denoiser. We then test ELF trajectories without changing the sampler. We then test a minimal schedule and three basin probes. We finally test decoder calibration, Cola-DLM boundary behavior, and short training-side basin widening. If any earlier stage failed, the later probe would be unmotivated. This ordering is what distinguishes the study from a collection of ablations.

5.1 Denoisability and Recoverability Decouple

Figure 2 shows the central diagnostic result. Denoisability and linguistic recoverability are not the same. Color separates the state-space family: blue points are language-model embedding spaces, while orange points are Cola-DLM VAE latents. Circle area encodes token recovery after denoising at $t = 0.5$, not model size; the size legend is shown at the right of the plot. Some spaces are easy under MSE but weak under semantic or decoder tests; other spaces preserve semantics while being poorly matched to a particular decoder. This explains why “continuous” alone is not enough for language diffusion.

The most useful reading is not as a ranking of encoders, but as a rejection of an overly broad hypothesis. If continuous diffusion worked merely because the state distribution is smooth or Gaussian-like, then covariance-matched controls should behave like contextual T5. They do not. Conversely, if token recovery alone were sufficient, token embeddings would be enough. They are not, because order-sensitive contextual structure is lost. The diagnostic

therefore points to a narrower requirement: the state must be smooth enough to denoise and structured enough to preserve linguistic distinctions relevant to the decoder.

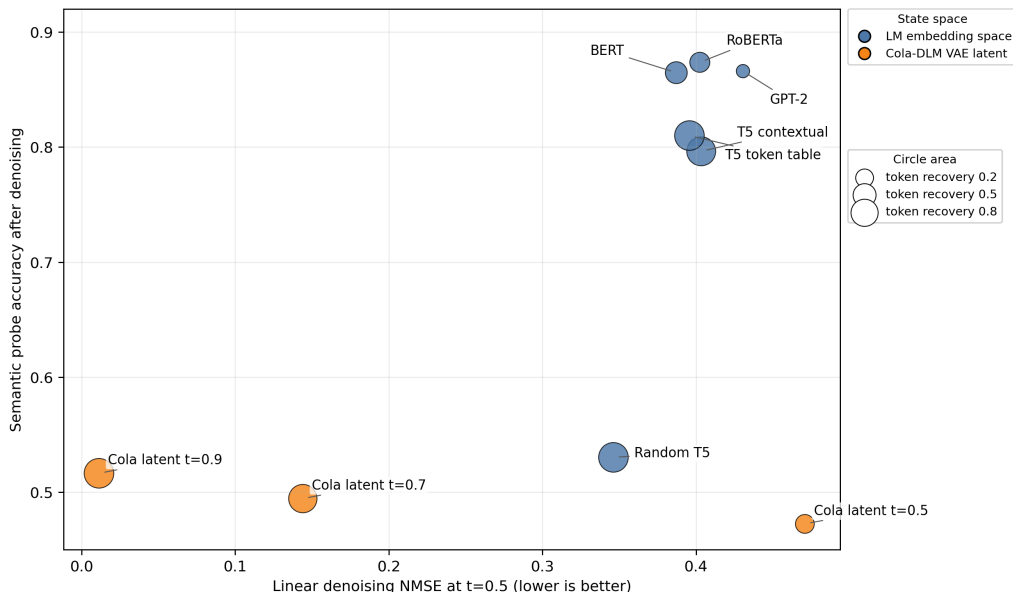


Figure 2: MSE can be misleading: denoisability and semantic recovery decouple. Color indicates state-space family (blue: language-model embeddings; orange: Cola-DLM VAE latents), and circle area indicates token recovery after denoising at $t = 0.5$, not model size. The size legend maps circle area to representative recovery values. The diagnostic must include linguistic and decoder-facing axes.

5.2 Controlled Degradation: PCA Bottlenecks Break the Interface

A diagnostic protocol is more convincing if it flags an interface problem before one invests in a new training run. We therefore construct a controlled degradation inside the same T5 contextual family. We fit PCA on T5 contextual latents, project the latents to rank r , and project back to the native 512-dimensional ELF interface. This preserves the official denoiser and decoder shapes, but removes low-variance directions that may be important for order or decoder margins.

This is a narrow controlled test. PCA is not meant to simulate a nonlinear VAE or a learned tokenizer; it is an intervention inside the same ELF/T5 coordinate system. Its value is that the diagnostic axes are sensitive to interface degradation while the checkpoint, decoder, and text distribution remain fixed. A protocol that catches this failure is better positioned to flag problematic state spaces encountered in practice.

High-rank PCA should preserve denoisability and decoder compatibility. Low-rank PCA may still preserve a large amount of variance and a nontrivial latent cosine, but should lose decoder margin. If the bottleneck is inserted only at the final endpoint, the decoder may partially tolerate it. If the bottleneck is imposed at every denoising step, the trajectory itself should move into a different operating region.

Figure 3 confirms the protocol’s sensitivity to a degraded interface. Rank 256 keeps 85.3% of variance and high decoder agreement. Rank 128 keeps 64.8% of variance and still preserves most native decoder decisions. Rank 64 is the first clear boundary: agreement falls to 0.938, the 10th percentile margin falls to 1.90, and generation begins to move along a repetition frontier. Rank 32 is the failure flagged by the diagnostic: agreement falls to 0.478 and the median margin becomes negative. When rank 32 is applied at every step, GPT-2-Large PPL becomes misleadingly low (7.53), but unigram entropy drops to 3.87, distinct-2 drops to 0.074, and bigram repetition rises to 0.926. The failure is diagnostic: low PPL can hide a collapsed state-space interface.

Figure 4 shows that the same bottleneck also changes the order-sensitivity axis. Under full word shuffling, full-rank T5 pooled representations fall to cosine 0.777, while rank-32 PCA remains at 0.966. In other words, the bottleneck makes the representation more order-invariant under the pooled diagnostic: it smooths away directions that carry contextual order differences. This is the desired controlled failure. A lower-dimensional projection can preserve enough variance to look geometrically benign while suppressing linguistic distinctions that the interface needs.

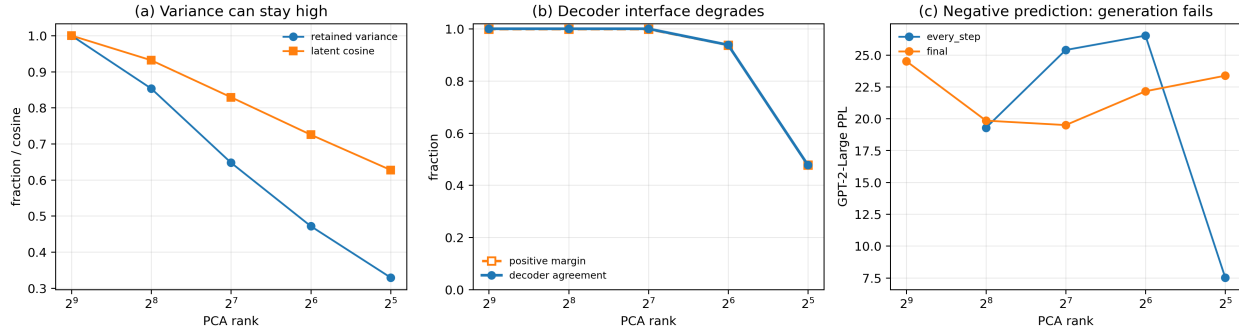


Figure 3: Controlled interface degradation through a PCA bottleneck. Left: retained variance and latent cosine remain high at moderate ranks. Middle: decoder agreement and margin degrade as the interface rank is reduced. Right: imposing the bottleneck along the generation trajectory yields low-PPL but low-diversity text. The every-step point at rank 2^9 is omitted because full-rank PCA is the identity map and duplicates the no-bottleneck baseline. The diagnostic flags the degraded interface even when variance appears adequate.

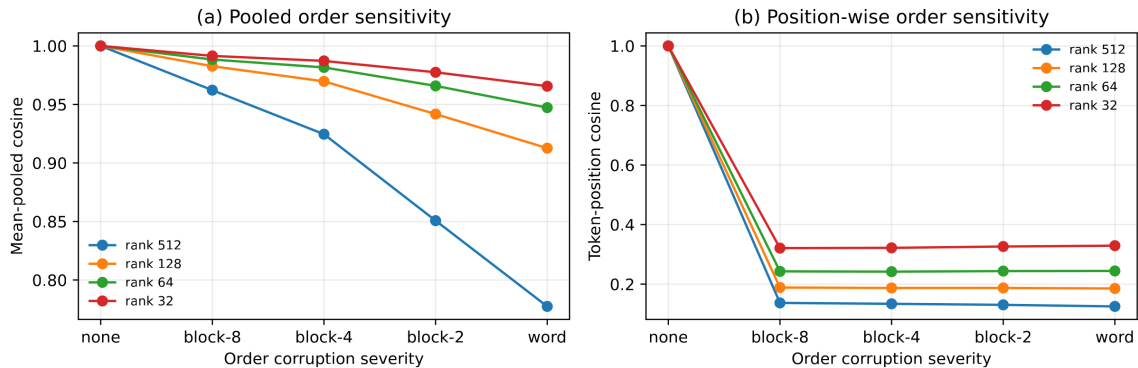


Figure 4: PCA bottlenecks reduce order sensitivity. Left: mean-pooled representations become less sensitive to stronger order corruption as rank decreases. Right: position-wise cosine shows the same effect at token locations. Low-rank variance preservation can therefore erase contextual order directions even when denoisability remains high.

5.3 Order Sensitivity Is Graded

The original order-sensitivity diagnostic used a binary real-vs-shuffled comparison. We strengthen it with graded block shuffling: keep words intact but shuffle blocks of length 8, 4, 2, or 1. The result is not merely that contextual encoders notice order. The shape of the degradation curve reveals what kind of order each state space preserves.

Figure 5 gives the graded order curve. T5 contextual embeddings degrade smoothly from cosine 0.906 under block-8 shuffling to 0.729 under full word shuffling. BERT shows a similar but slightly stronger degradation, from 0.890 to 0.724. T5 token embeddings, by contrast, remain nearly flat around 0.90 in mean-pool cosine because they largely preserve a bag-of-words signal; their first-token cosine collapses, but the pooled representation does not encode contextual order in the same way. GPT-2 and RoBERTa pooled states are more invariant under this particular pooling metric, which is itself informative: order sensitivity should be measured with a representation and pooling choice that matches the proposed decoder interface.

This graded curve strengthens the interface claim. A state space can be easy to denoise and easy to decode while still failing to expose the word-order distinctions a language generator needs. Diffusion-readiness is therefore not a scalar smoothness property that can be verified by inspecting the covariance spectrum in isolation.

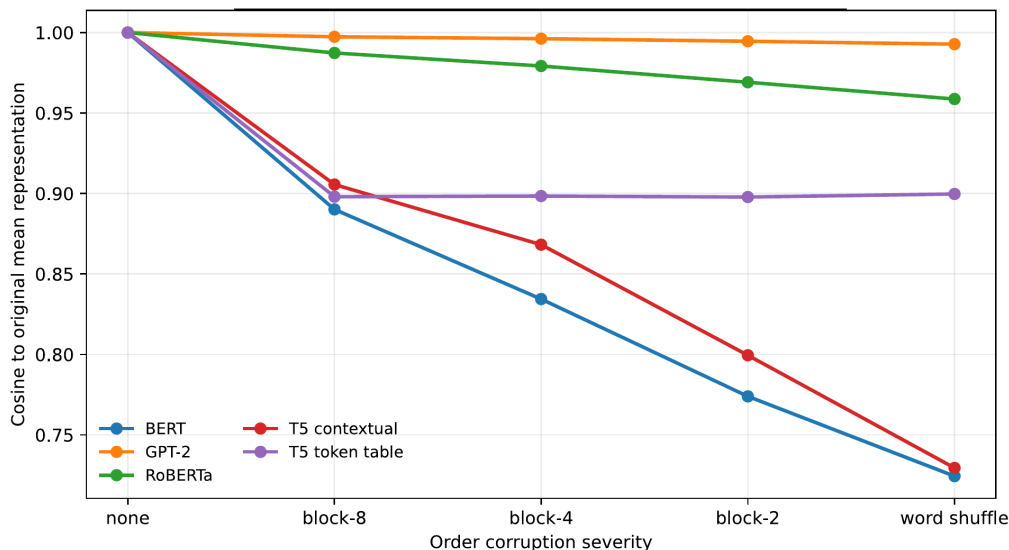


Figure 5: Order sensitivity is graded. The horizontal axis increases order corruption from none to full word shuffle; the vertical axis is cosine similarity to the original mean representation, so lower values mean stronger order sensitivity. Contextual T5 and BERT degrade progressively, whereas T5 token embeddings remain nearly flat under mean pooling, exposing a bag-of-words failure mode.

5.4 ELF Trajectories Expose Reliability Signals

Across three 1024-sample seeds, ELF’s internal trajectory signals are predictive under the standard ELF GPT-2-Large PPL evaluator. For ELF-B fixed SC=3, the peak relative self-conditioning change has Spearman correlation -0.417 ± 0.009 with per-sample log PPL, while the minimum agreement with the zero-SC prediction has 0.411 ± 0.009 . For ELF-M, the corresponding correlations are weaker but stable: -0.253 ± 0.017 and 0.239 ± 0.016 . Shuffled-signal permutation tests give $p \leq 0.005$ for these core signals. A two-seed ELF-L confirmation with 512 samples per seed and 64 SDE steps shows that reliability signals persist at 652M parameters, but the strongest region shifts. For seed 0, the mid-trajectory mean SC change has $\rho = 0.359$ and the mid-trajectory zero-SC agreement has $\rho = -0.356$ with log PPL. For seed 1, the same mid-trajectory signals remain significant with $\rho = 0.224$ and $\rho = -0.225$, while the full-trajectory SC-change peak reaches $\rho = -0.336$. All three ELF-L core correlations have permutation $p = 0.002$. These are not formal certificates of text quality; they are trajectory statistics that remain informative under the reported automatic metrics and signal controls.

We use per-sample GPT-2-Large PPL here because it is the most sensitive cheap scalar for within-checkpoint trajectory correlations. This does not contradict the PPL critique above. The claim in this subsection is narrow: under a fixed checkpoint and a fixed sampler family, PPL is a useful *relative proxy* for ranking samples from the same operating regime, and internal signals correlate with the standard evaluator used by ELF. It is not a sufficient cross-model, cross-sampler, or cross-temperature quality objective. Later calibration and boundary experiments therefore pair PPL with entropy, repetition, MAUVE, JS divergence, decoder agreement, and margin precisely because PPL alone can validate the wrong operating region.

The sign of the correlation is less important than its existence and localization. ELF-B and ELF-M expose reliable extrema over the full trajectory, whereas ELF-L exposes a clearer mid-trajectory average. This is consistent with a scale-dependent schedule: larger denoisers may stabilize earlier or distribute correction differently across time, but they still reveal reliability before final decoding. This observation argues against a purely final-decoder explanation of generation quality, in which the denoiser merely minimizes latent error and the decoder resolves all linguistic structure at the last step.

Figure 6 shows the main ELF-B/M reliability curves: a per-sample scatter makes one signal concrete, and a correlation summary shows that several trajectory statistics predict the standard GPT-2-Large PPL evaluator. Figure 7 summarizes the two-seed ELF-L check with the shifted mid-trajectory signals.

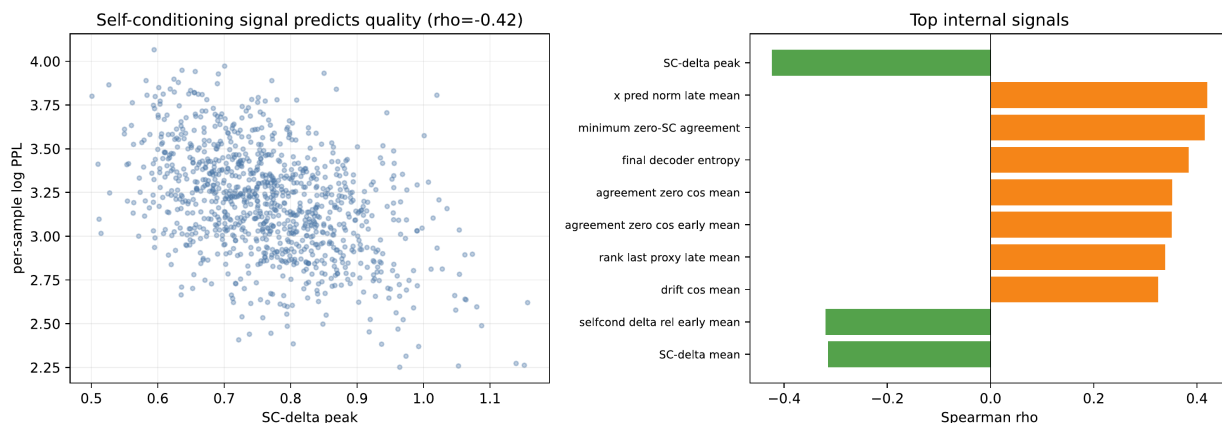


Figure 6: ELF internal signals predict the standard PPL evaluator. Left: each point is one generated sample; the x-axis is the peak relative self-conditioning change along the trajectory, and the y-axis is per-sample GPT-2-Large log PPL. Lower PPL tends to occur when this internal change is larger, giving a negative Spearman correlation. Right: the x-axis is Spearman ρ between each trajectory statistic and log PPL; the y-axis lists candidate statistics. Multiple internal signals correlate with the evaluator before external scoring, motivating the later basin-navigation audit.

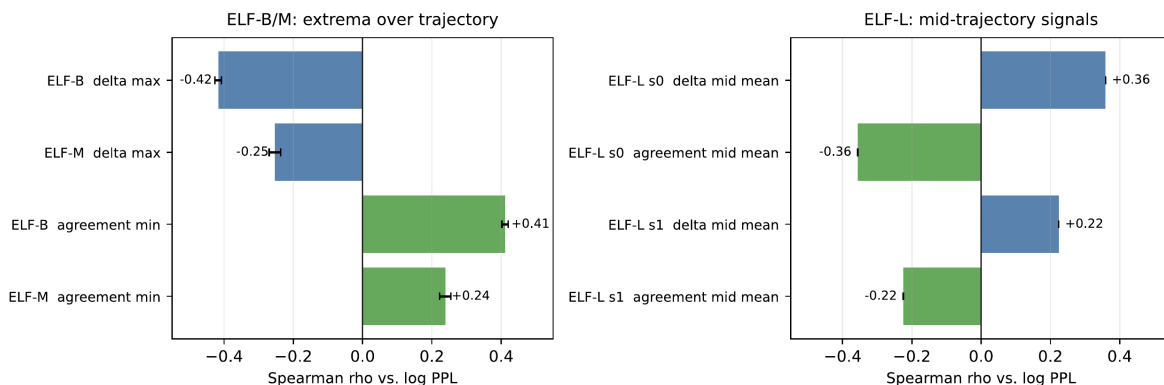


Figure 7: ELF-L trajectory reliability at larger scale. The x-axis in both panels is Spearman ρ with per-sample log PPL; bars to the left mean the statistic is larger for lower-PPL samples, and bars to the right mean it is larger for higher-PPL samples. The left panel repeats the strongest whole-trajectory extrema from ELF-B/M, while the right panel reports two independent ELF-L seeds using mid-trajectory summaries. The correlations persist, but the strongest time region shifts, so the signal is phase-dependent rather than a universal confidence scalar.

5.5 Mechanism: Denoising as Basin Navigation

The correlation result above leaves a mechanistic ambiguity. Do these reliability signals simply correlate with final PPL, or do they reflect how the trajectory approaches the decoder interface? We answer this by measuring decoder margins at every denoising step. For each step, we decode the predicted clean latent \hat{x}_t through the native decoder and record top-1-vs-top-2 margins, decoder entropy, and self-conditioning disagreement. We then run a smaller selected-step audit that asks whether intermediate predictions already agree with the final decoded tokens.

Figure 8 gives a compact picture. This single-checkpoint audit uses raw denoising steps to show the actual SDE32 chronology; the cross-scale and sampler-comparison plots below use normalized phase so that 32- and 64-step trajectories can be compared. The 10th-percentile decoder margin of \hat{x}_t grows from 0.049 at step 0 to 12.30 at step 31, while decoder entropy falls from 6.18 nats to 0.018 nats. Self-conditioning disagreement is not monotone. It rises from zero, peaks around steps 16–18 at about 0.47, and then falls. The delta-margin correlation is also phase-dependent: it is near zero early, becomes positive in the middle region where disagreement peaks, and then becomes strongly

negative late (mean Spearman $\rho = -0.31$ after step 24). Thus self-conditioning disagreement is not a universal confidence score. It becomes a margin proxy only once the trajectory has approached the decoder basin. A post-hoc GPT-2-Large evaluation on the same 512 samples connects the mechanism back to quality: maximum mid-trajectory self-conditioning delta correlates with log PPL at $\rho = -0.499$, early 10th-percentile margin mean at $\rho = -0.445$, and late decoder-entropy minimum at $\rho = 0.409$.

We use “compare” as a compact description of this statistical pattern, not as a directly observed internal algorithm. The measurements are consistent with a comparison-then-commitment transition: candidate clean predictions differ most in the middle, while final-token margins and agreement appear later. They do not by themselves reveal the exact computation performed inside the denoiser.

Basin-entry timing. The selected-step audit makes the basin interpretation sharper. At step 0, the margin of the final decoded tokens under the intermediate logits is strongly negative (p10 = -19.4), and agreement with the final decode is only 1.0%. At step 20, agreement has risen to 76.2% but the final-token margin is still negative (p10 = -10.4). The boundary is crossed around step 24: final-token p10 margin becomes positive (0.76), and agreement reaches 89.5%. By step 31, final-token p10 margin is 12.57 and agreement is 99.96%. Intermediate decodes become diverse earlier than this: decoded sample entropy reaches about 5.0 by step 16, but high-margin final compatibility arrives later. This separates *readability* from *basin entry*.

This is the empirical counterpart of Theorem 1. As the trajectory enters the decoder basin, the relevant margin-to-sensitivity ratio should increase, making residual perturbations less likely to change tokens. We do not estimate the full local sensitivity spectrum here, but the measured part of the prediction is direct: lower-tail final-token margin moves from a large negative value to a large positive value, while final-token agreement rises from 1.0% to 99.96%. This is the mechanism layer on top of the diagnostic layer. The first layer says what fails: MSE, PPL, and clean reconstruction can each validate the wrong thing. The second layer says why ELF succeeds when it succeeds: the denoiser transports predictions through a phase of proposal, self-conditioning disagreement is statistically consistent with candidate revision, and the final phase enters a high-margin decoder-readable basin.

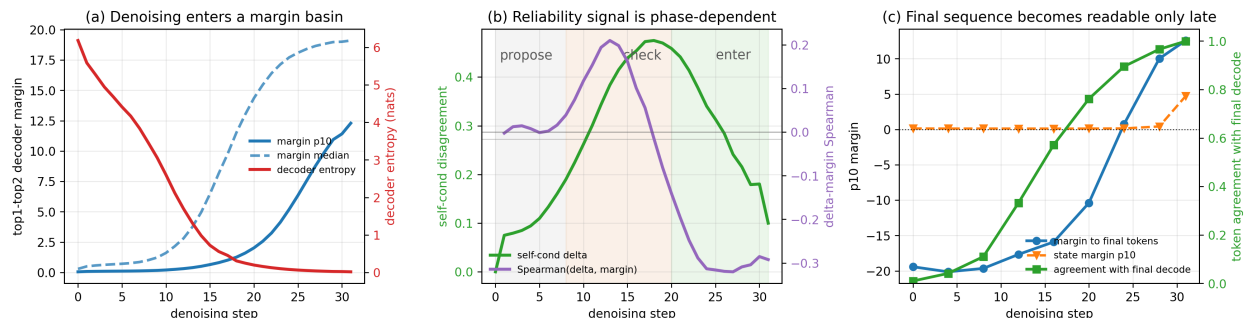


Figure 8: Denoising as basin navigation. (a) Decoder margins widen while decoder entropy collapses. (b) Self-conditioning disagreement is phase-dependent: it peaks in the middle region and becomes a negative margin proxy only late. (c) The final sequence enters a positive-margin basin late in the trajectory; readability and final-token compatibility are not the same.

5.6 Interface Phase Diagram

The basin-navigation plot above is a trajectory audit; the same measurements can be summarized as an empirical interface phase diagram. The horizontal coordinate is normalized denoising phase. The vertical coordinates are decoder-facing reliability signals: native margin, ZSBD agreement, final-token agreement, entropy, and token-wise entry. We use three region names only as diagnostic shorthand. In the *pre-entry* region, token-embedding alignment is weak and final-token agreement is low. In the *competition* region, candidate basin labels become readable but are not yet stable; ZSBD agreement rises rapidly and token positions enter asynchronously. In the *locked* region, the lower-tail native margin is high and most token decisions persist.

Figure 9 makes this dynamic view explicit. For ELF-B SDE32, ZSBD agreement rises from 10% to 90% over a width of 0.635 normalized phase units, crossing the midpoint at phase 0.460 and reaching 90% at phase 0.858. ODE32 has a similar ZSBD transition width (0.631) but reaches Margin-8 later (phase 0.923 rather than 0.853). Scale shifts entry earlier: in the cross-scale audit, the Margin-8 phase moves from 0.871 for ELF-B SDE32 to 0.746 for ELF-B SDE64, 0.667 for ELF-M SDE64, and 0.587 for ELF-L SDE64. This earlier entry is consistent with the BGEE

frontier, where the conservative Margin-12 gate saves 17.1%, 23.0%, and 27.3% of denoising steps (number of function evaluations, NFEs) on B/M/L respectively.

The token-wise panel explains why sample-level early exit has a ceiling. In the 512-sample audit, stable Margin-8 entry is reached by 94.7% of token positions, with shard-p90 phase 0.819, while persistent native-token entry reaches 99.96%. The hard tail is structured rather than uniform: numeric tokens reach stable Margin-8 only 79.8% of the time, and rare tokens reach it 81.4% of the time. Thus the interface transition is not a single global event. It is a mostly shared sequence-level transition with an asynchronous token tail. This phase-diagram view is the main conceptual object of the paper. A static readability observation says that some final states are easy for a decoder and others are not. Our evidence asks the stronger time-resolved question: how does an existing ELF trajectory enter the native decoder basin, how does the entry shift with scale and sampler, and which token classes remain outside the early locked region? The supported claim is dynamic and diagnostic: basin entry is a measurable transition summarized by crossing phases and transition widths, not merely a final-state label.

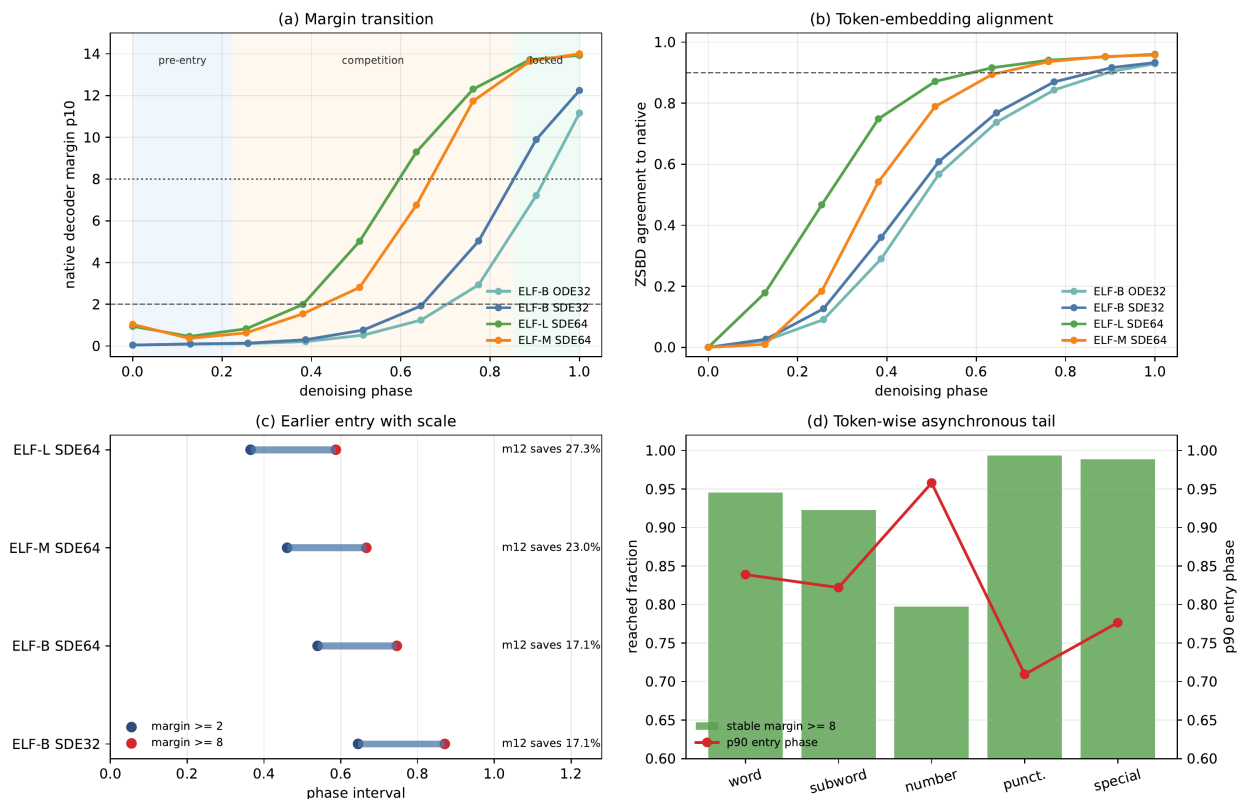


Figure 9: Interface phase diagram for ELF basin entry. (a) Native decoder margins trace pre-entry, competition, and locked regions. The region names are empirical diagnostics rather than thermodynamic phases. (b) ZSBD agreement follows the same transition, rising from weak token alignment to a high-agreement locked region. (c) Cross-scale entry shifts earlier under stronger models and longer SDE sampling; text at right reports conservative BGEE Margin-12 savings from the existing held-out summary. (d) Token-wise entry is asynchronous: most tokens lock early, but numeric and subword-like tail positions remain harder.

5.7 Scale, Sampler, and Architecture Checks

Robustness checks. A useful mechanism should survive obvious perturbations. We therefore rerun the basin-navigation audit across ELF-B, ELF-M, and ELF-L; compare SDE32, SDE64, and ODE32 on ELF-B; and run analogous boundary probes on LangFlow [8] and BitstreamDiffusion [4]. These checks are not meant to make the paper a benchmark suite. They test whether the margin-basin story is an artifact of one checkpoint, one sampler, or one specific decoder implementation.

Figure 10 shows the cross-scale result. All ELF scales widen the decoder margin over denoising time, but the phase at which a strong basin is reached shifts with scale. For ELF-B SDE32, the 10th-percentile margin crosses 2.0 around

phase 0.65 and 8.0 around phase 0.87. With 64 SDE steps, the same model reaches these thresholds earlier (phase 0.54 and 0.75). ELF-M and ELF-L reach them earlier still. A shard-level robustness audit (Figure 11) confirms that these basin-entry shifts are larger than variation across four independent 128-sample sampling shards: the Margin-8 entry phase moves from 0.863 ± 0.008 for ELF-B SDE32 to 0.675 ± 0.010 for ELF-M SDE64 and 0.587 ± 0.017 for ELF-L SDE64. These error bars measure sampling/shard-level robustness under fixed checkpoints, not training-seed uncertainty or a scaling law. The delta-margin sign flip remains visible as a mid-trajectory positive peak followed by a negative late correlation, but its shape is scale-dependent. We therefore use the sign flip as evidence of a revision-to-commit transition, not as a universal scalar confidence law that generalizes across architectures without recalibration.

We report two complementary correlation estimates. Step-wise correlations use per-sample Spearman statistics within a single denoising step; they have high temporal resolution and identify where the sign flip happens, but are noisy at 128 samples. The shard-level audit first aggregates each 128-sample shard over coarse trajectory regions and then reports the standard error of the mean (SEM) across shards; it loses some temporal resolution but establishes sampling robustness. Apparent numerical differences between the two estimates should therefore be read as a resolution–variance trade-off, not as conflicting measurements.

Figure 12 shows that the qualitative mechanism is not specific to SDE noise. ODE32 has a different entropy trajectory, but it still exhibits margin growth and a late delta-margin sign change. This separates basin entry from a purely stochastic-sampler artifact. The sampler changes how the trajectory explores the interface; it does not remove the need to enter the decoder basin.

The external checks in Figure 13 test the same concept outside ELF under a stricter hierarchy of evidence. LangFlow exposes a weaker latent-step margin trajectory: its native margins become positive but do not reach the high ELF lower-tail margins, and sparse final-token probes remain negative in the lower tail on both OWT and the One Billion Word Benchmark (LM1B) [7]. Figure 14 places these external signals beside ELF’s final-basin margins and Cola-DLM target-recovery diagnostics to show that the state objects differ even when the interface questions are shared. A direct ELF-to-LangFlow cross-decoder test would not isolate basin transfer, because the released LangFlow checkpoints use GPT-2 or BERT tokenizers with learned 768-dimensional token embeddings rather than ELF’s T5 decoder interface; without a separately trained adapter, such a test would confound decoder geometry with vocabulary and coordinate-system mismatch. A direct LangFlow delta-margin audit (Figure 15) makes the analogy more precise: on LM1B and OWT, the mid-trajectory Spearman peak between self-conditioning delta and native margin is positive (0.18 and 0.32), while the late average becomes negative (-0.35 and -0.53). BitstreamDiffusion exposes a bit-level analogue: structured proxy codes and real OWT code ids show nearly identical sigma-sweep behavior (Figure 16); for example, at $\sigma = 0.5$ the bit recovery is 0.822 for the structured proxy and 0.828 for real OWT codes. These observations support the interface language but do not independently prove ELF’s mechanism. Figure 17 makes this hierarchy explicit: ELF carries the main mechanism evidence, while LangFlow, BitstreamDiffusion, and Cola-DLM are boundary checks that ask whether denoisability, decoder compatibility, and trajectory reliability remain meaningful when the state object and decoder change.

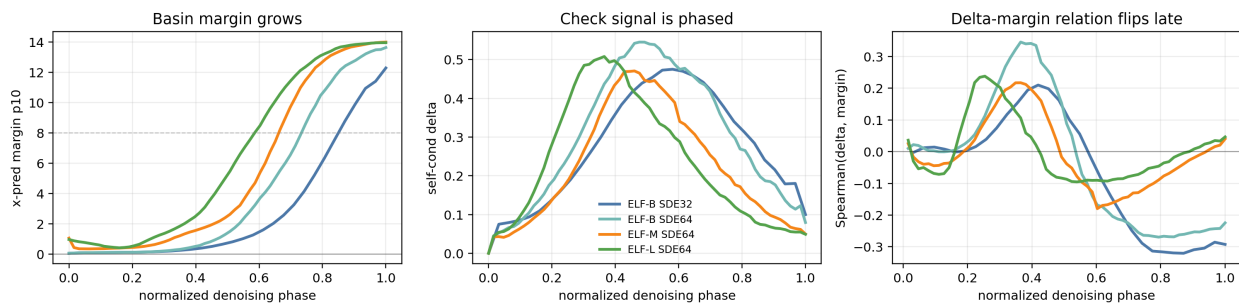


Figure 10: Basin-navigation signals across ELF scale. Left: 10th-percentile native decoder margin over normalized denoising phase. Middle: self-conditioning disagreement over the same phase axis. Right: step-wise Spearman correlation between self-conditioning disagreement and decoder margin. Margin growth is shared by ELF-B/M/L, while the strongest self-conditioning–margin relation shifts with scale.

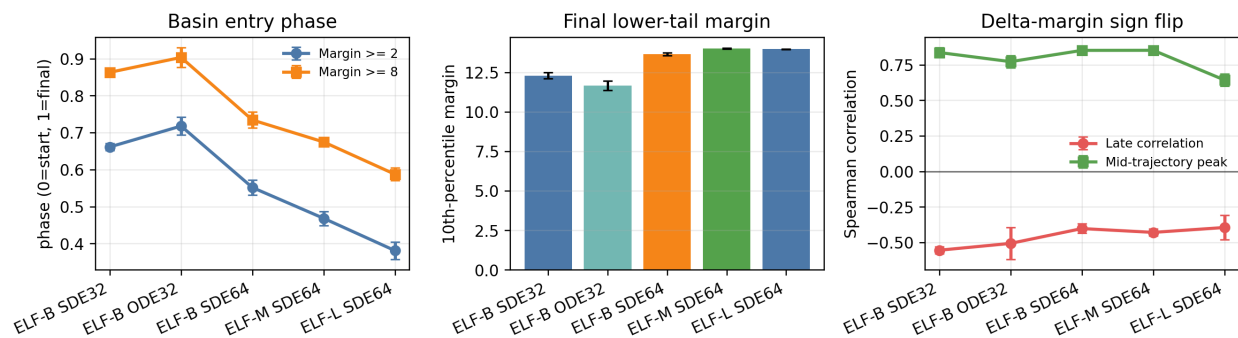


Figure 11: Shard-level robustness of the basin-navigation audit. Left: basin-entry phase under two margin thresholds. Middle: final lower-tail decoder margin. Right: mid-to-late delta-margin sign-flip strength. Each condition contains four independent 128-sample GPU shards; error bars show SEM across sampling shards under fixed public checkpoints, not training-seed uncertainty. Basin entry shifts earlier with model scale, while the self-conditioning–margin relation remains scale-dependent rather than a universal scalar law.

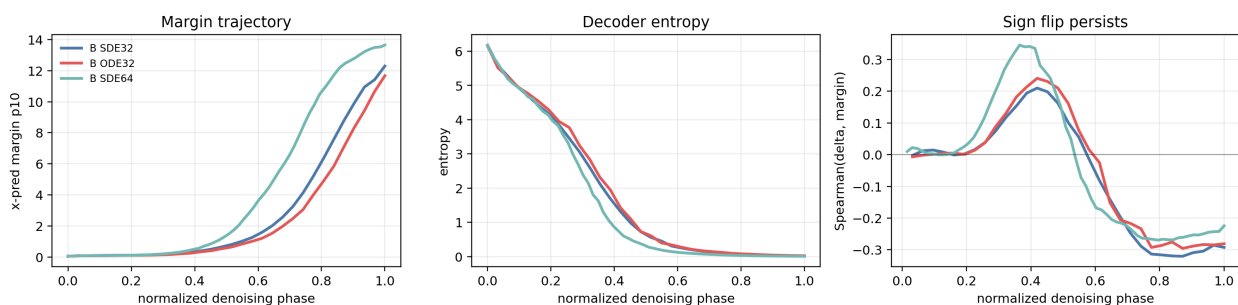


Figure 12: ODE and SDE sampler comparison. Left: native decoder margin grows under both samplers. Middle: decoder entropy follows a different schedule-dependent trajectory. Right: the delta–margin correlation still changes sign late. Basin entry is therefore not only an artifact of SDE noise injection.

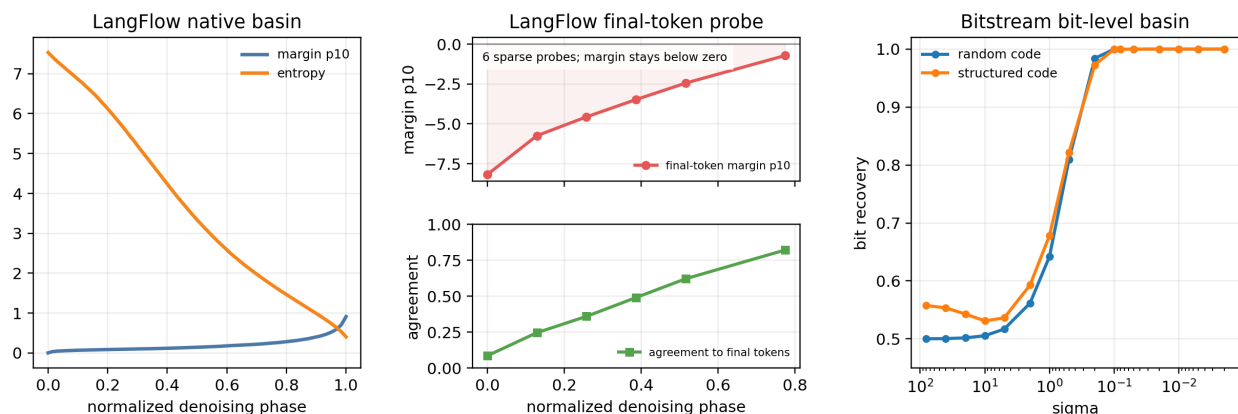


Figure 13: External boundary checks. Left: LangFlow native step margins provide a weaker latent-step analogue of ELF’s decoder-margin audit. Middle: sparse LangFlow final-token probes show rising agreement but a lower-tail final-token margin that remains below zero. Right: BitstreamDiffusion produces a bit-level basin analogue through recovery and margin under increasing code noise. Axes use each model’s native interface units and should be compared qualitatively, not as a shared numerical scale.

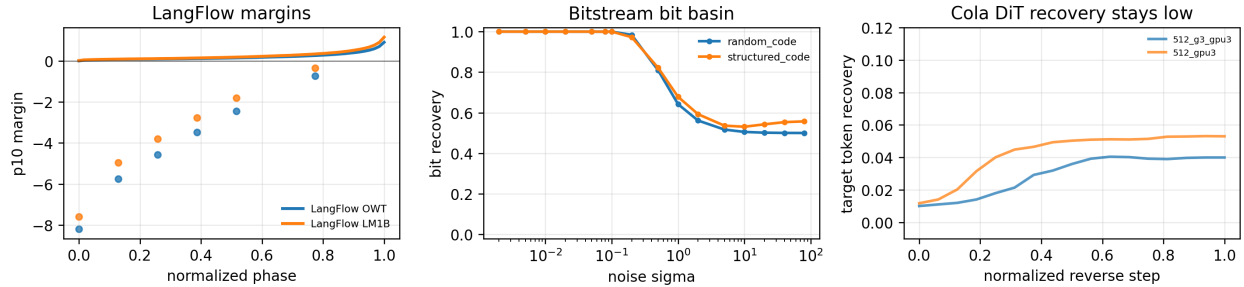


Figure 14: External interface overlay. Left: LangFlow native step margins rise, while sparse final-token commitment probes remain stricter. Middle: BitstreamDiffusion shows a bit-level basin analogue rather than a full text-generation reproduction. Right: Cola-DLM DiT target-token recovery remains low, matching the VAE boundary interpretation. The panel compares interface diagnostics, not benchmark rank.

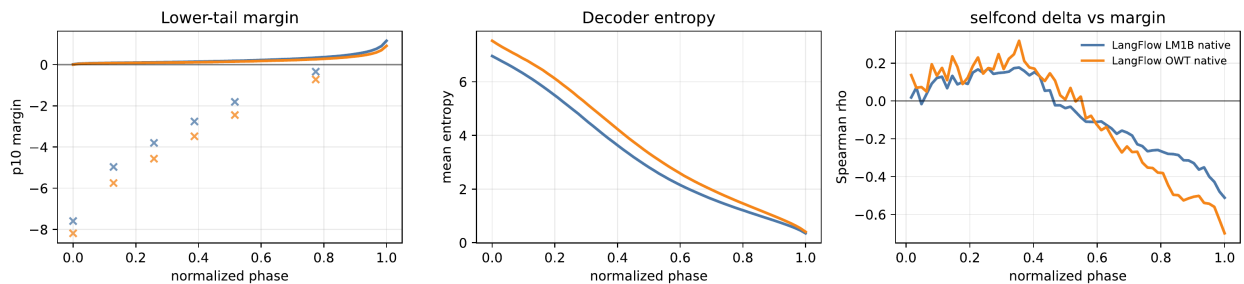


Figure 15: LangFlow delta-margin audit. Left: native lower-tail margins rise along the trajectory; the sparse cross markers show final-token margin probes and remain lower because they ask whether the intermediate logits already support the eventual final tokens. Middle: decoder entropy falls as the latent state becomes more committed. Right: the self-conditioning delta/margin relation is positive in the middle and negative late. The qualitative revision-to-commit pattern is ELF-like, but LangFlow margins remain smaller and final-token commitment is stricter.

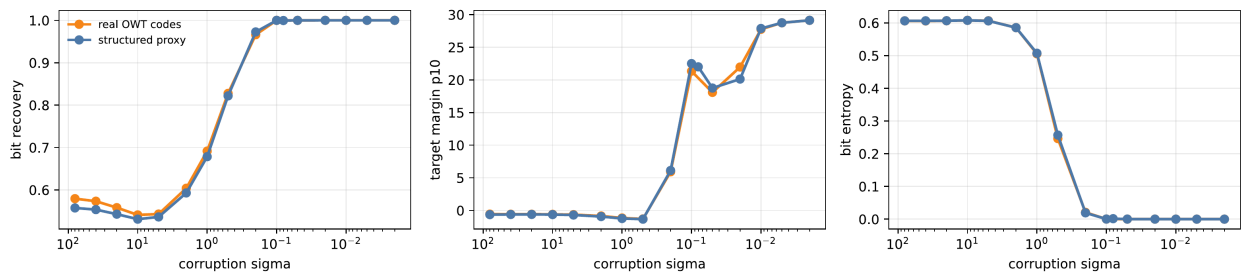

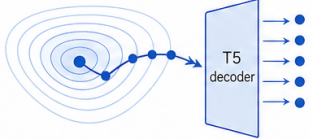
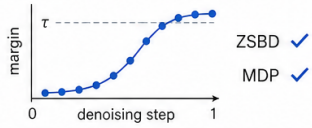



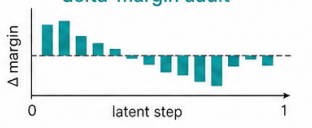



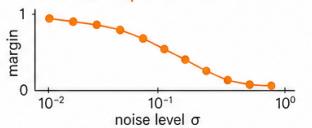
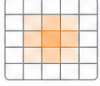

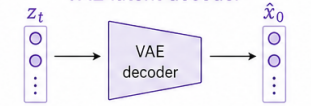
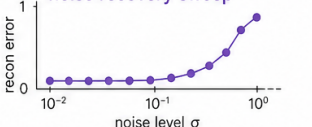



Figure 16: BitstreamDiffusion real-code validation. A 512-sample real OWT code sweep matches the earlier structured-code proxy closely, so the bit-level basin analogue is not an artifact of synthetic code ids.

5.8 Layer-Wise Decoder Basins

The preceding experiments test trajectories. A complementary question is whether decoder compatibility is a generic property of hidden states or a precise interface property. We therefore run a layer-wise margin sweep. For T5, we feed normalized hidden states from layers 0–6 and the final encoder state into the native ELF decoder. For BERT, RoBERTa, and GPT-2 we use their own native language-modeling heads, because cross-decoder comparisons would mostly test vocabulary and scale mismatch rather than a meaningful interface.

Figure 18 shows that decoder compatibility is layer-local. After applying ELF’s latent normalization, the T5 final state is highly readable by the ELF decoder: clean token recovery is 0.99996, the 10th-percentile target margin is 15.42, and recovery at $t = 0.7$ remains 0.99993. Earlier layers are not uniformly better or worse. Layers 0–3 are sharply decodable, layers 4–5 form a margin valley, and the final normalized encoder state re-enters the native decoder basin.

Model family	Interface object	Diagnostic probe	Lesson
 ELF	T5 decoder basin 	margin trajectory + ZSBD + MDP 	strong basin entry 
 LangFlow	latent-step margin 	delta-margin audit 	stricter final-token commitment 
 BitstreamDiffusion	bit-level posterior 	noise sweep over code bits 	bit-level basin analogue 
 Cola-DLM	VAE latent decoder 	noise recovery sweep 	clean reconstruction is not enough 

diagnostic mapping, not benchmark ranking

Figure 17: Interface diagnostics beyond ELF. The external checks do not turn the paper into a benchmark suite; they show how denoisability, decoder compatibility, and trajectory reliability map onto different state objects: ELF’s T5 decoder basin, LangFlow’s latent-step margins, BitstreamDiffusion’s bit-level posterior, and Cola-DLM’s VAE latent decoder under noise corruption.

Native BERT and RoBERTa heads also concentrate positive margin in their final layers, while GPT-2’s next-token head is not directly comparable under a same-position recovery test and remains a useful negative control. This result is small but important. It rules out the idea that any contextual hidden state with high lexical information is automatically diffusion-ready, regardless of which layer or normalization scheme produced it. The decoder basin depends on the exact layer, normalization, and readout. This is the same lesson as the PCA controlled-degradation experiment at a finer resolution: preserving information is not equivalent to entering the right tokenization basin where the decoder can assign stable decisions.

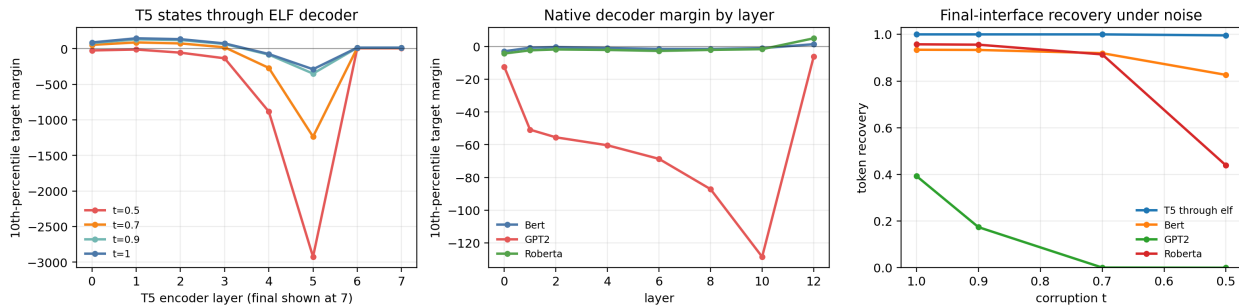


Figure 18: Layer-wise decoder-basin tests. Left: clean token recovery for hidden states decoded through their native or matched readout. Middle: 10th-percentile target margin at the clean point. Right: token recovery after a fixed corruption level. T5 states must be normalized into ELF’s native latent interface, and compatibility is layer-local rather than a generic property of contextual representations.

5.9 A Minimal Schedule Validates the Signal

The trajectory-reliability signal suggests a minimal schedule: use stronger self-conditioning early, default self-conditioning in the middle, and weaker self-conditioning late. Table 3 shows three-seed results. Front-loading is consistently slightly better than fixed SC=5 in terms of PPL, while preserving similar entropy. It is not an optimized sampler; it is a small intervention validating the diagnostic.

Figure 19 places this schedule in the PPL–entropy plane, and Figure 20 shows the more important time-region control: moving the same guidance strength to the wrong part of the trajectory degrades quality. On the same seed and 512 samples, front-loading gives PPL 23.45, while reversing the schedule (strong SC late, weak SC early) gives PPL 26.48. This is the most controlled intervention because it keeps the same guidance values but swaps when they are applied. In contrast, simple online delta-gating is not yet a reliable sampler: true, delayed, randomized, and clipped gates all remain within a narrow band. We therefore make a conservative claim: ELF exposes trajectory information that can validate a time-region schedule, but converting this into a generally superior adaptive policy remains future work.

We also tested even more literal one-line interventions suggested by the diagnostics. We averaged final states with late clean predictions, applied token-level margin-aware temperature scaling, and used a dispersive logit scaling control. Across four low-memory runs (front-loaded 256 samples, a second front-loaded seed with 128 samples, and fixed SC=3/5 with 128 samples each), late clean-prediction averaging gives only small PPL changes: last-two-clean averaging improves by 0.03–0.13 PPL, while a non-adjacent clean-prediction average improves by 0.18–0.36 PPL. This suggests a weak smoothing effect near the final predicted-clean states rather than a strong adaptive policy. Margin-aware temperature is more decisive as a negative result: it consistently worsens PPL by 0.20–0.23, and a shuffled-margin control is similarly bad. Averaging the final state with initial noise hurts strongly (+0.68–0.98 PPL). These controls strengthen the diagnostic framing: internal signals and decoder margins are meaningful measurements, but local one-line rules are not yet robust methods that can be trusted without further validation.

Table 3: Three-seed 1024-sample confirmation of the front-loaded self-conditioning schedule. The table reports corpus-level GPT-2-Large PPL and generated-text entropy across three sampling seeds for ELF-B and ELF-M.

Model	Setting	PPL mean \pm std	Entropy mean \pm std
ELF-B	fixed SC=3	24.01 \pm 0.24	5.158 \pm 0.006
ELF-B	fixed SC=5	22.99 \pm 0.23	5.135 \pm 0.008
ELF-B	front-loaded	22.82 \pm 0.23	5.135 \pm 0.008
ELF-M	fixed SC=3	26.35 \pm 0.31	5.244 \pm 0.008
ELF-M	fixed SC=5	23.85 \pm 0.41	5.202 \pm 0.011
ELF-M	front-loaded	23.77 \pm 0.40	5.202 \pm 0.011

5.10 Three Minimal Basin Probes

Three probes, one basin. The basin view naturally suggests three minimal probes. They measure the same mechanism from three views rather than define three separate decoding products. Unless otherwise specified, *basin* below refers to the native decoder margin basin defined in Section 4; ZSBD and MDP measure geometric and linear shadows of that basin, not new basin definitions. The word *minimal* refers to the added modeling machinery: BGEE is a rule over an existing margin, ZSBD uses a frozen lookup, and MDP uses one linear readout. Their sample counts and monitoring costs differ, and those costs are reported separately. BGEE is a *basin-timing probe*: if the trajectory has already entered a high-margin decoder basin, stop. ZSBD is a *token-alignment probe*: once inside the basin, ask whether final states are already close to frozen T5 token embeddings. MDP is a *linear-recoverability probe*: ask how much of the native decoder interface can be recovered by a single readout trained on generated final states. Figure 21 summarizes this structure and makes the relationship among the three probes visually explicit.

BGEE: a basin-timing probe. The previous schedule experiment validates that the signal matters, but it still uses a fixed number of denoising steps. A natural diagnostic question is whether the measured basin can support a minimal action: if the trajectory has already entered a high-margin decoder basin, stop. We implement *Basin-Guided Early Exit* (BGEE), a training-free rule that monitors the 10th-percentile native decoder margin of the predicted clean latent. Once the margin exceeds a threshold for a short run of consecutive steps, we decode immediately. No policy is learned, no new model is trained, and the rule uses the same decoder-margin quantity used by the diagnostic.

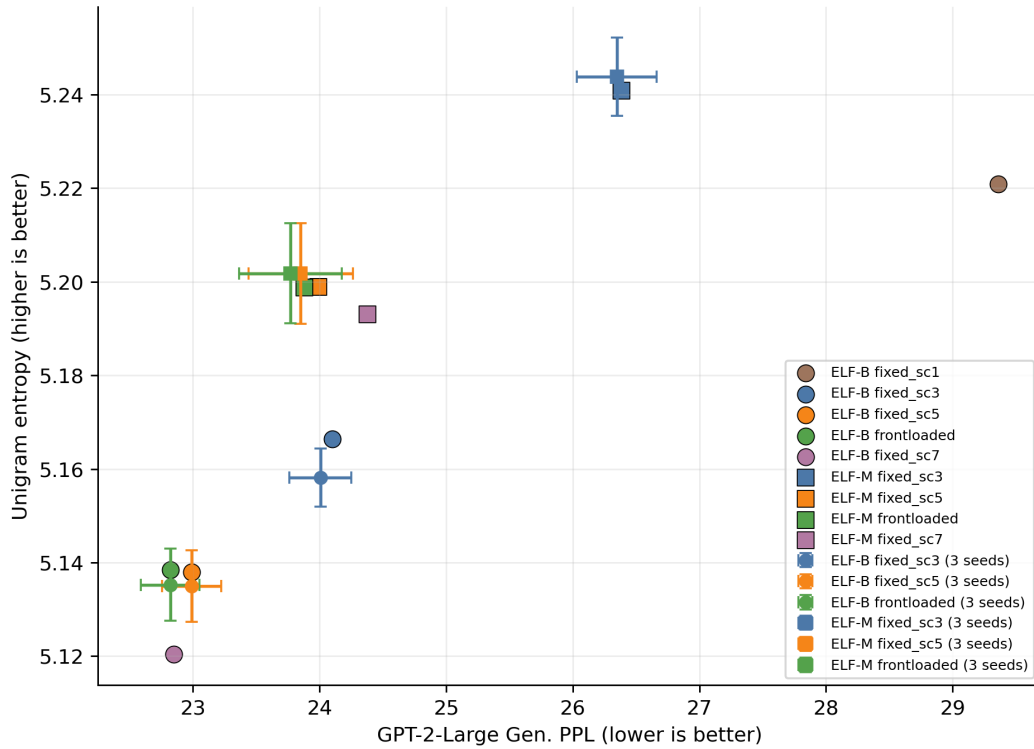


Figure 19: PPL–entropy frontier for fixed and front-loaded self-conditioning schedules. Each point is a sampling configuration evaluated with GPT-2-Large PPL and sample entropy. Front-loading moves slightly toward lower PPL without the large entropy collapse caused by stronger fixed guidance.

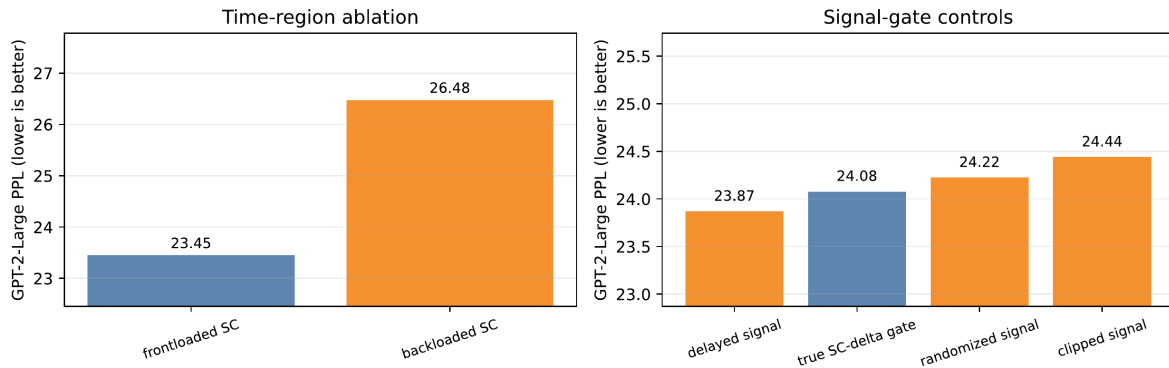
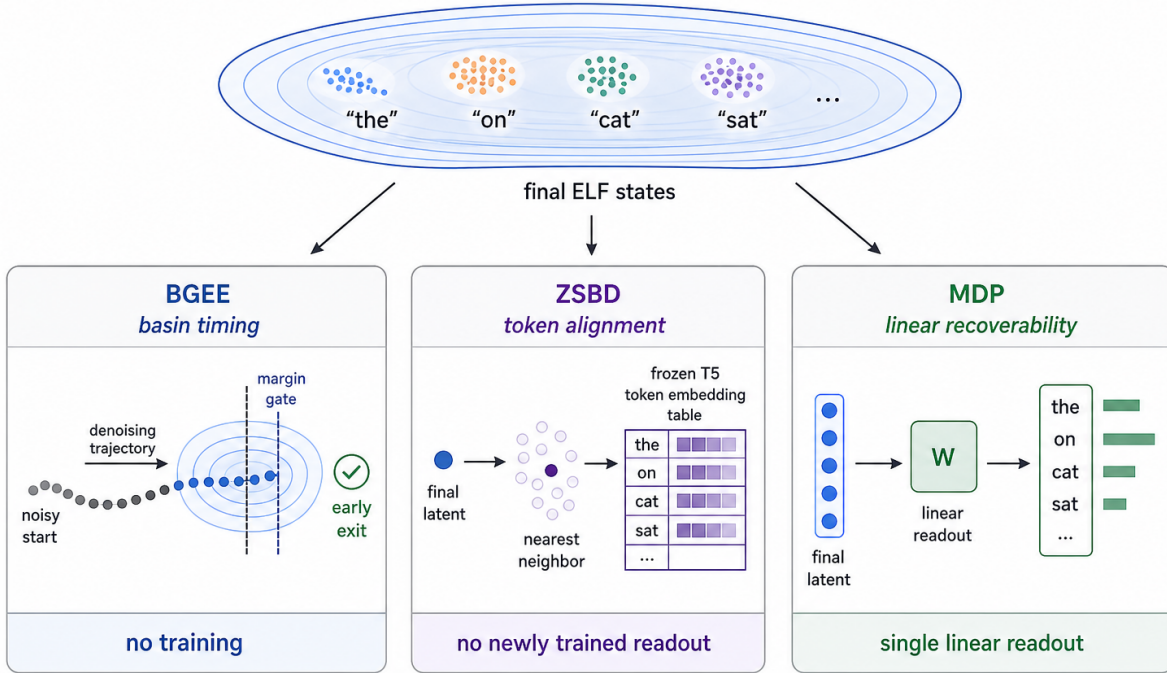


Figure 20: Time-region and signal-gate controls. Left: front-loading self-conditioning improves over the reversed schedule, confirming that the discovered time region is not arbitrary. Right: online delta-gating variants remain close to each other and do not form a mature adaptive sampler. The schedule result validates the phase signal, while the gate controls keep the method claim limited.



three probes of one basin, not three separate products

Figure 21: Three minimal probes of the decoder basin. BGEE measures basin-entry timing, ZSBD measures frozen token-embedding alignment with no newly trained readout, and MDP measures local linear recoverability. They are probes of one basin-navigation mechanism, not three separate products.

Figure 22 shows the speed-quality curve on ELF-B SDE64 with 512 samples. The conservative Margin-12 threshold exits at an average number of function evaluations (NFE) of 53.1, saving 17.1% of denoising steps while essentially matching full decoding (geometric PPL 18.45 vs. 18.38, mean PPL 19.24 vs. 19.21, and token agreement 0.969 to the full decode). These geometric PPL values come from the single early-exit audit and should not be compared directly with the multi-seed arithmetic PPL table above. A more aggressive Margin-8 threshold exits at average NFE 45.4, saving 29.1% with moderate degradation (geometric PPL 19.28, agreement 0.925). Fixed exits can also save compute and sometimes lie on a similar frontier. BGEE contributes a decoder-facing timing criterion: it exits when the measured interface has been reached rather than at a hand-picked step.

The cross-scale confirmation in Figure 23 makes the same point more strongly. The conservative Margin-12 gate saves 23.0% NFEs on ELF-M and 27.3% on ELF-L while preserving high agreement to the full decode (0.965 and 0.972). The Margin-8 gate saves 32.2% and 41.2% NFEs with the expected moderate degradation. We do not interpret the absolute PPL values across model sizes as scaling claims, since these public checkpoints and evaluation settings are not a controlled training sweep. The robust trend is narrower: the larger checkpoints enter the measured decoder basin earlier, and BGEE converts that earlier entry into a larger compute saving.

BGEE is not presented as a final sampler. It is a simple timing probe that follows from the mechanism. To check that the result is not purely hand-picked on the reporting set, we also perform a deterministic half-split validation: margin gates are selected on one half of generated samples using an agreement-and-PPL constraint and then evaluated on the held-out half. The selected held-out gates save 16.6%, 23.4%, and 27.6% NFEs on ELF-B/M/L SDE64 respectively, with token agreement above 0.96 and small geometric-PPL changes relative to full decoding. This monotonic increase with checkpoint size is an empirical trend rather than a fitted law: the three checkpoints were not produced as a controlled scaling suite. It nevertheless gives a concrete hypothesis for future larger DLMs: earlier basin entry should either keep improving with denoiser scale, saturate at a representation-limited floor, or break under a different training recipe. We also test a random-time control that scans the same eligible denoising steps in a shuffled temporal order before applying the same margin rule. At matched compute on a 512-sample control run, ordered Margin-12 saves

15.9% NFEs with geometric-PPL change $+0.13$ and agreement 0.967, while random-time Margin-5 saves 15.5% with geometric-PPL change $+0.44$ and agreement 0.958. The gate therefore uses both the margin threshold and the ordered denoising trajectory.

The NFE numbers are algorithmic, not an optimized systems claim. The literal monitor used here decodes each predicted-clean state to compute a lower-tail margin, which adds overhead. A small wall-clock smoke test confirms the caveat: on four 32-sample GPU shards, unmonitored 64-step sampling takes 25.3 seconds on average, per-step monitoring takes 45.5 seconds, and a conservative batch-level early-exit implementation takes 44.0 seconds. We also audited the simplest cheap proxy, the self-conditioning delta. It is informative but phase-dependent: it is positively related to margin early, becomes a strong negative proxy late, and is less stable across scales. It is therefore not a drop-in replacement for native-margin monitoring. An efficient implementation would need a learned cheap proxy, sparse monitoring, or dynamic batching. In this paper BGEE is diagnostic: decoder-basin entry becomes an actionable stopping criterion once a cheap monitor exists.

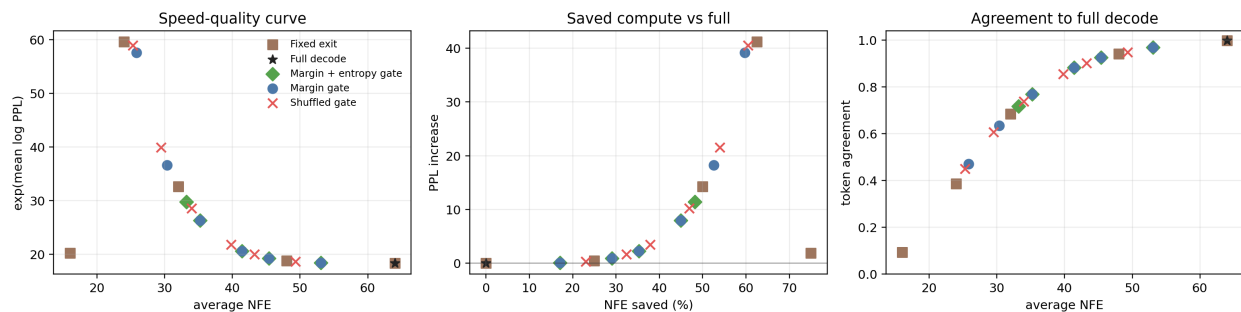


Figure 22: Basin-Guided Early Exit (BGEE) as a basin-timing probe. Left: speed-quality curve for fixed exits, margin gates, and shuffled controls. Middle: compute saved relative to the full 64-step decode. Right: token agreement with the full decode. Margin gates are not claimed to dominate every fixed exit; they show that measured native-decoder basin entry can act as an interpretable stopping signal.

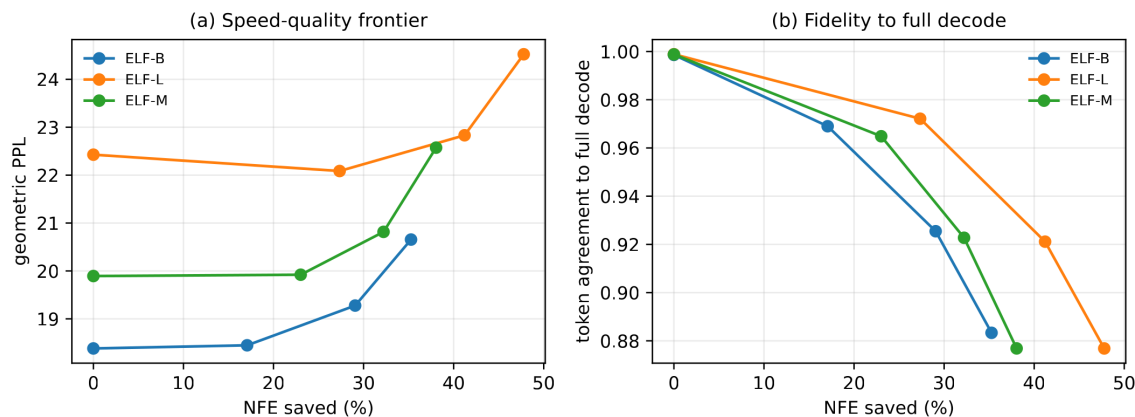


Figure 23: Cross-scale BGEE confirmation. Left: geometric PPL versus denoising compute saved for margin-gated exits across ELF-B/M/L. Right: token agreement with the full 64-step decode under the same exits. Larger checkpoints tolerate earlier exits at comparable fidelity, matching the diagnostic finding that they enter the final decoder basin earlier.

MDP: a linear-recoverability probe. We present MDP before ZSBD because it first estimates how linearly recoverable the native interface can become when a small matching set is allowed; ZSBD then asks the stricter no-new-readout question. Once ELF has navigated into the final basin, how much of the native decoder is still essential? We define *Minimal Decoder Protocol* (MDP). We freeze the ELF denoiser, sample generated final states, decode them with the native decoder to obtain target tokens, and train a single token-wise linear readout from late latent states to those native tokens. Unless otherwise specified, MDP reports the best late-state variant on this generated-state manifold; the appendix lists the separate z_T , \hat{x}_T , and last-two-clean variants. This is not meant to replace the official decoder in a deployed model. It is a controlled interface test: if a small readout fails, the native decoder is doing substantial nonlinear work; if it succeeds, then the denoiser has already concentrated final states into a nearly linearly separable

region of the native basin where simple classifiers can recover most token identities.

Figure 24 shows that both statements are partly true. With only 1024 generated latents, the best linear readout reaches about 81.6% token agreement to the native decoder and remains far worse in PPL (36.1 vs. 21.7 on the held-out split). With 4096 generated latents and 1.2M token-position training examples, the same protocol reaches 93.9–94.1% token agreement and reduces geometric PPL to 28.0–28.4, compared with 23.9 for the native decoder on the same split. The best 4k readout also closely matches the native decoder’s diversity: sample unigram entropy is 5.06, distinct-2 is 0.714, and 4-gram repetition is 0.0676. Pushing the same protocol further reveals that 4k is not the saturation point: with 8192 generated latents, agreement rises to 97.0% and PPL falls to 25.5; with 16384 generated latents, agreement reaches 97.6% and PPL falls to 24.8; with 32768 generated latents, agreement reaches 97.9% and PPL stays around 24.8, compared with native PPL 23.6 on the same held-out split. The 16k–32k gain is smaller than the 4k–8k gain, suggesting that the linear readout is approaching the native interface while retaining a stable residual calibration gap.

The cross-scale confirmation in Figure 25 shows the same qualitative behavior on ELF-M and ELF-L. With only 1024 generated latents, a linear readout recovers most native tokens (84.6% on ELF-M and 86.7% on ELF-L), but the PPL gap remains large. Increasing the matching set to 4096 generated latents produces the same jump observed on ELF-B: ELF-M reaches 93.7% agreement with PPL 33.1 versus native PPL 26.2, and ELF-L reaches 94.5% agreement with PPL 38.1 versus native PPL 30.3. The margin lower tail widens in tandem, with p10 margin moving from roughly 0.41 at 1k to roughly 1.4 at 4k on both larger checkpoints. We therefore interpret MDP as an interface-complexity probe rather than as a recommendation to remove the native decoder.

The result sharpens our decoder claim. A direct unembedding baseline is overly stringent, and small learned decoders can be misleading when evaluated only by PPL. MDP gives a cleaner intermediate: a single readout trained to imitate the native interface can recover most of the final-token basin from generated latents, and the remaining gap shrinks steadily with more matching examples. Even at 32k, however, the native decoder retains a measurable calibration advantage. The residual-tail analysis below shows why: the remaining errors concentrate in low-margin, rare, numeric, subword, and token-embedding-hard cases. Most token decisions are therefore linearly recoverable after basin entry; the native decoder calibrates a small structured tail that simple linear readouts cannot fully capture.

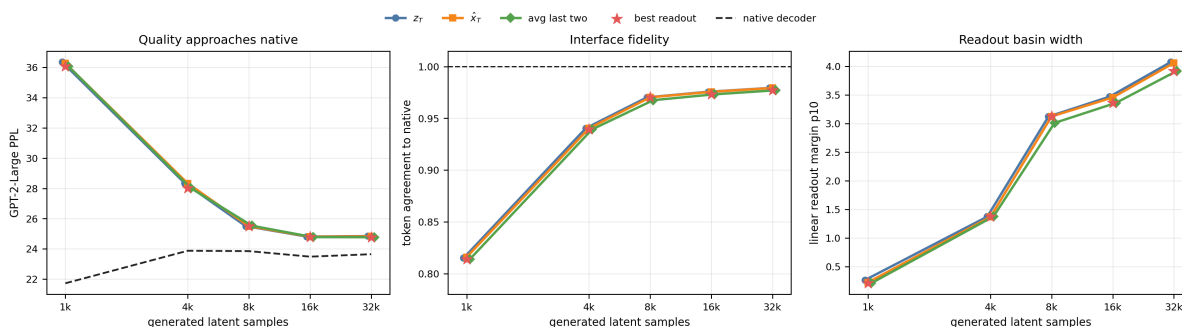


Figure 24: Minimal Decoder Protocol (MDP). Left: GPT-2-Large PPL of linear readouts trained on 1k–32k generated final latents, with the dashed line showing native decoding on the same held-out split. Middle: token agreement between the linear readout and the native decoder. Right: 10th-percentile margin of the learned linear readout, measuring the width of the recovered readout basin. A single linear readout recovers most of the native interface, while the remaining PPL gap shows that the native decoder still calibrates the tail.

ZSBD: a token-alignment probe. MDP still trains a readout. We next ask a stricter minimal-readout question: after ELF has entered the final basin, can the state be decoded with *no newly trained readout at all*? In *Zero-Shot Basin Decoding* (ZSBD), we normalize each final latent vector and each frozen T5 token embedding, then choose the nearest token by cosine similarity. This is not the native contextual decoder; it is a frozen Voronoi lookup in the original token-embedding table. It is therefore a strong interface-specific prior, not a prior-free decoder: success means that ELF has transported final states toward its own tied T5 token-embedding geometry.

The result in Figure 26 is compelling, though it does not replace native decoding. On 4096 ELF-B generated latents, nearest-neighbor lookup from either z_T or the final clean prediction recovers 93.45% of the native decoder’s tokens. Evaluated on 1024 samples with GPT-2-Large, ZSBD obtains PPL 32.56. This is worse than the native decoder and worse than the best MDP readout, but it is far from failure: ELF final states have moved close enough to token-embedding Voronoi cells that a frozen lookup recovers most native decisions. A 16384-sample sanity check gives the same conclusion (93.34% agreement for z_T and \hat{x}_T). The cross-scale check is stable and slightly stronger

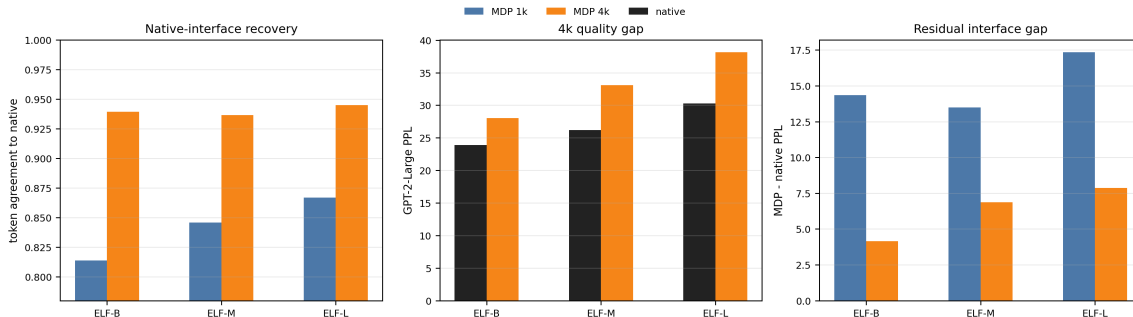


Figure 25: MDP cross-scale confirmation. Left: native-token agreement for 1k and 4k matching sets across ELF-B/M/L. Middle: GPT-2-Large PPL for the corresponding linear readouts where evaluated. Right: residual gap to native decoding. The 4k readout recovers roughly 94% of native tokens across checkpoints, making MDP a probe of decoder-interface complexity rather than a replacement decoder.

at larger checkpoints: using the same protocol on 4096 generated latents, ELF-B/M/L obtain 93.45%, 95.22%, and 95.57% agreement, respectively (Figure 27). ZSBD therefore sharpens the basin-navigation picture. The denoiser is not merely producing arbitrary continuous vectors that require a complex decoder to interpret; it is transporting states toward a token-aligned region. The native decoder still matters for the remaining tokens and for calibration, but the final basin has a simple geometric shadow.

We then ask whether this token-embedding alignment is a final-state accident or a trajectory phenomenon. Figure 28 decodes intermediate predicted-clean states by the same frozen nearest-neighbor lookup. The agreement rises with basin entry. On 512 ELF-B SDE32 samples, ZSBD-to-native agreement is essentially zero at step 0, reaches 0.61 around phase 0.52, 0.87 around phase 0.77, and ends at 0.93. On 512 ELF-M SDE64 samples, it reaches 0.79 around phase 0.51 and 0.96 at the final step. On 256 ELF-L SDE64 samples, it reaches 0.75 already around phase 0.38 and ends at 0.96. The ELF-B ODE32 control follows the same qualitative curve and ends at 0.93. The mean nearest-neighbor cosine increases in parallel with the native decoder margin. This directly links ZSBD to basin navigation: token-embedding Voronoi alignment emerges during the same process that makes the native decoder readable, and the transition moves earlier with model scale. The overview in Figure 29 places this trajectory-level ZSBD curve beside basin-entry timing and held-out BGEE savings, showing that the three probes are different projections of the same basin state, with BGEE measuring timing, ZSBD measuring geometric alignment, and MDP measuring local linearity.

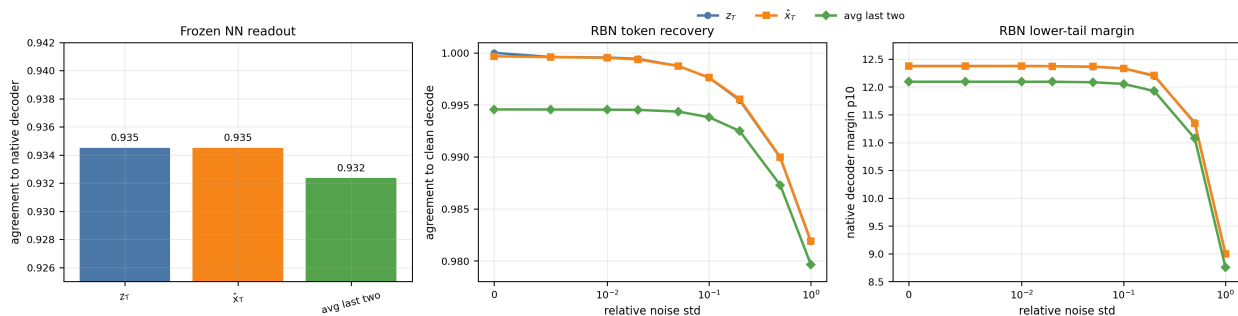


Figure 26: Zero-shot and reverse-basin tests. Left: ZSBD decodes final ELF states by nearest-neighbor lookup in frozen T5 token embeddings and recovers over 93% of the native decoder’s token decisions with no newly trained readout, while using the tied T5 token table. Middle/right: RBN corrupts final states and decodes with the native decoder; token recovery and margins degrade slowly under isotropic noise, showing that the final basin is wide but absorbing under random perturbations.

Basin geometry after entry. We also run reverse-basin navigation (RBN), the reverse experiment. Starting from generated final states, we add isotropic Gaussian noise and decode with the native ELF decoder. If final-state editing under a Basin-Constrained Decoding (BCD) sentiment direction failed only because the final basin were extremely tight, small random perturbations should immediately destroy token recovery. The opposite happens. For ELF-B z_T , relative noise standard deviation 0.5 still gives 98.99% agreement to the clean native tokens, and even noise 1.0 leaves 98.19% agreement with 10th-percentile margin around 9.0. The effect is stronger at larger scale: at noise standard deviation 1.0, ELF-M and ELF-L retain 99.21% and 99.43% agreement, respectively, with 10th-percentile margins

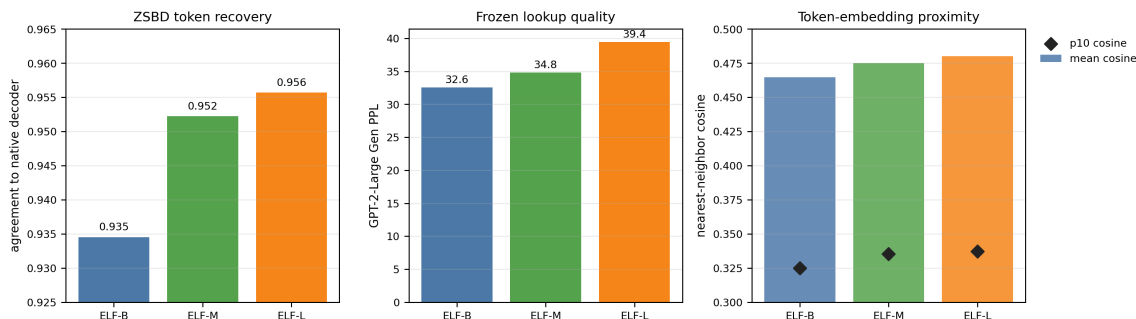


Figure 27: ZSBD cross-scale confirmation. Left: frozen nearest-neighbor agreement with the native decoder, using the T5 token-embedding table and no newly trained readout. Middle: GPT-2-Large PPL of the ZSBD outputs where evaluated. Right: stability of the lookup as sample count increases. Agreement improves slightly with model scale, but PPL remains worse than native decoding; ZSBD is evidence for token-aligned basin entry, not for removing the decoder.

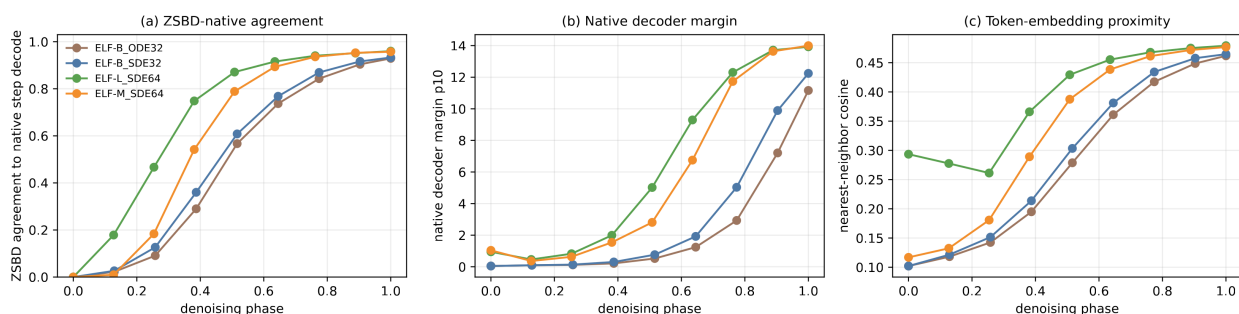


Figure 28: Intermediate-step ZSBD at larger scale. Left: ZSBD-native agreement over normalized denoising phase. Middle: native lower-tail decoder margin over the same phase axis. Right: nearest-neighbor cosine to frozen T5 token embeddings. Frozen token lookup becomes reliable as the trajectory enters the decoder basin, and the transition appears earlier for larger checkpoints and under both SDE and ODE sampling.

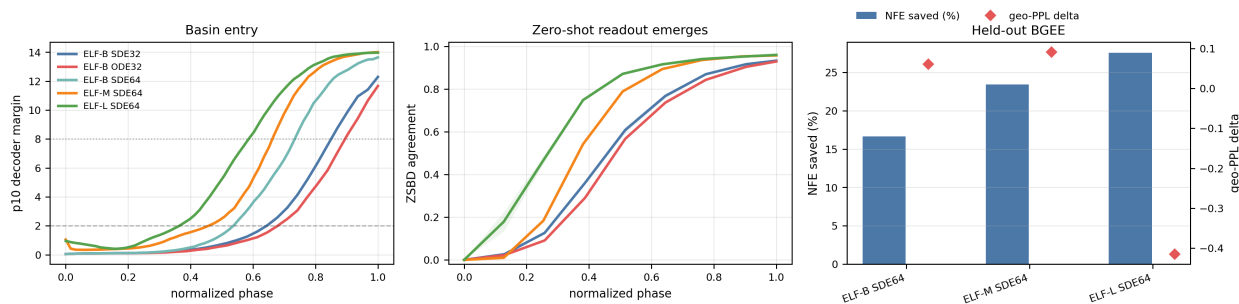


Figure 29: Basin probes in one view. Left: ELF checkpoints enter the decoder basin at different normalized phases. Middle: frozen ZSBD readout emerges along the same trajectory, with shard-level SEM where independent shards are available. Right: a held-out BGEE gate turns earlier basin entry into algorithmic NFE savings under a margin monitor.

above 10 (Figure 31). Thus the final basin is not locally fragile under isotropic noise.

Wide but anisotropic. Figure 32 compares matched-norm directions on ELF-B final states. Isotropic noise, one fixed random direction, and the BCD sentiment direction all retain about 98.2% token agreement at scale 1.0, with p10 margins near 8–9. In contrast, the first two PCA directions of the generated latent cloud cross the basin boundary: agreement falls to 64.0% and 44.1%, and p10 margins collapse to 0.46 and 1.14. The cross-scale check in Figure 33 confirms the qualitative pattern while showing that the fragile principal direction is checkpoint-dependent. ELF-M is especially fragile along its first PCA direction (agreement 0.015 at scale 1.0), whereas ELF-L is more fragile along its second PCA direction (agreement 0.489); isotropic and sentiment directions remain above 0.99 on the same checkpoints. This raises a natural question: is the extreme ELF-M PC1 a linguistic attribute direction, or a decoder-interface direction? The follow-up audit in Figure S6 answers the question in favor of the second interpretation:

ELF-M’s fragile PC1 is not a clean sentiment, tense, or formality axis, but aligns with the frozen T5 token table’s punctuation and token-boundary anisotropy. This explains why final-basin sentiment editing is a boundary result rather than a contradiction. Late ELF states are robust under many perturbations, but high-variance data-manifold directions can leave the native decoder basin. The final state is therefore excellent for stopping and readout probes, but poor as a generic semantic editing canvas.

Figure 30 summarizes the mechanism that emerges from these probes. Entry is measurable: margins and frozen token lookup rise during denoising. Readout is simple inside the final basin: a single linear readout recovers nearly all native token decisions on the generated manifold. But the basin is not a license for arbitrary latent editing. It is wide in random directions, absorbing along the simple sentiment direction, and fragile along certain high-variance directions. The remaining quality gap is concentrated in a structured residual tail that the native decoder calibrates better than a frozen lookup or linear readout, especially on rare and out-of-domain tokens.

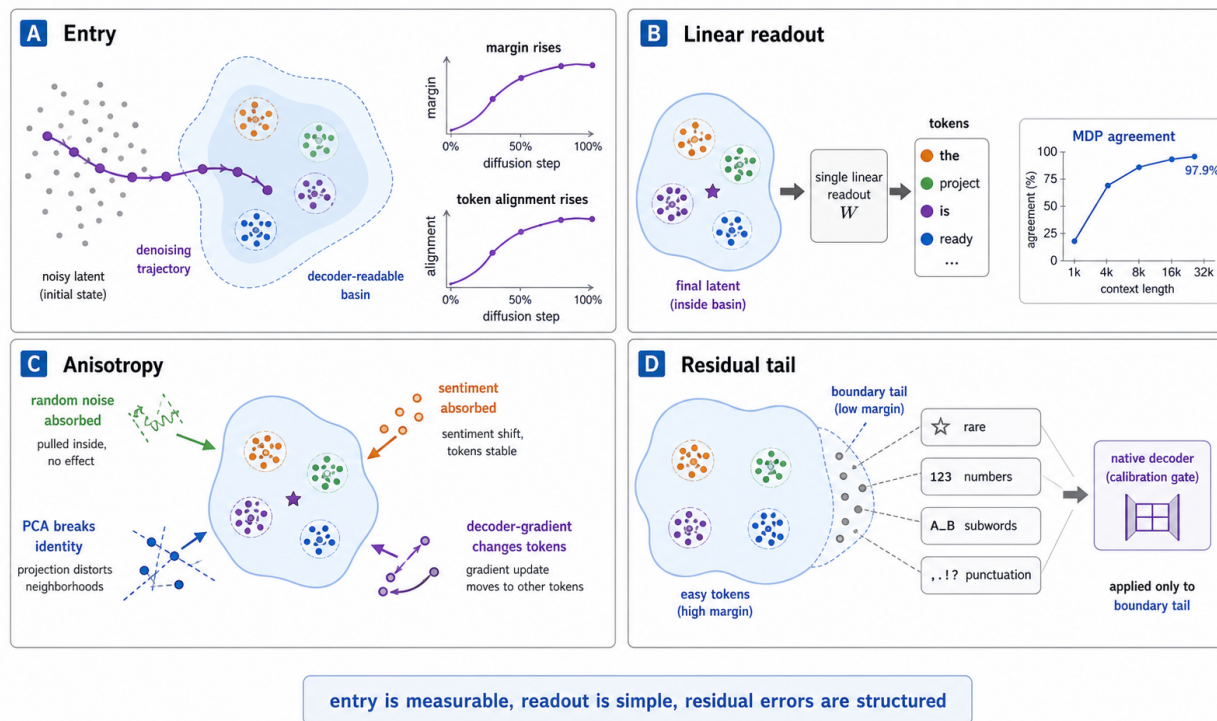


Figure 30: Inside the decoder basin. Panel A illustrates basin entry: margin and frozen token-embedding alignment rise together as denoising proceeds. Panel B summarizes MDP: inside the final basin, most native token decisions are recoverable by a single linear readout as the generated-latent matching set grows. Panel C shows anisotropy: random and sentiment-direction perturbations are largely absorbed, while PCA and decoder-gradient directions expose the fidelity-control trade-off. Panel D explains the residual tail: the native decoder still calibrates low-margin, rare, numeric, subword, and punctuation cases that simple readouts handle less reliably.

Residual tail. The ZSBD/MDP gap is concentrated in a fragile lower tail rather than spread uniformly. Figure 34 repeats the residual analysis on the 32k MDP saturation run, using 4096 held-out generated samples and 4.19M valid token positions. The single linear readout agrees with the native decoder on 97.89% of tokens, but its errors are not random. The native 10th-percentile margin over all tokens is 12.49, whereas the 10th-percentile margin among MDP-mismatched tokens is only 0.37. Very-low native-margin tokens have a 9.69% MDP error rate, compared with 0.45% or less once the native margin leaves the bottom quintile. ZSBD-hard tokens are also MDP-hard: when frozen token-embedding lookup is wrong, the MDP error rate is 23.36%, versus only 0.60% when ZSBD is correct. Frequency and type give a complementary view. Rare tokens have an 8.06% MDP error rate, numbers have 8.69%, and subwords have 5.21%, while punctuation and common word-start tokens are much easier. Position bins are nearly flat. The operational implication is sharp. Most token decisions are already made easy by basin entry; the remaining quality gap is dominated by a small, structured tail of low-margin, token-embedding-hard, and lexical-boundary cases that the native decoder calibrates better than a single linear readout.

Same-token clean-manifold gap. The residual tail could mean either that ELF final states are intrinsically hard

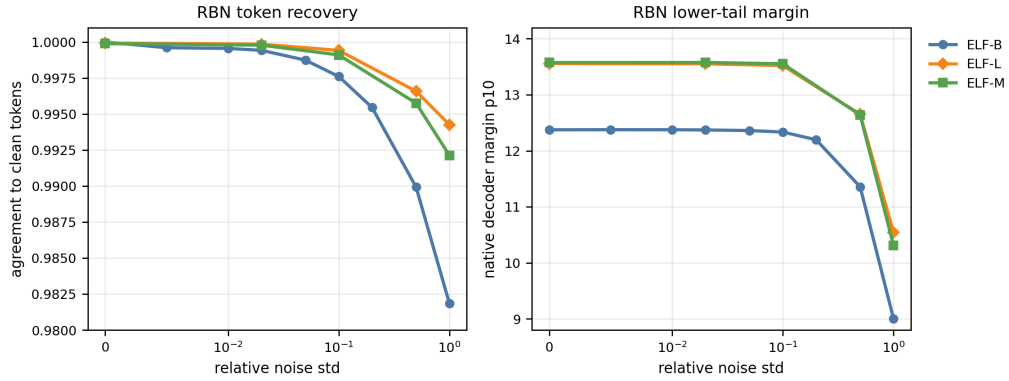


Figure 31: RBN cross-scale confirmation. Left: token agreement after adding isotropic noise to final ELF states. Right: corresponding native decoder margin under the same perturbations. Across ELF-B/M/L, token identity remains stable under large random perturbations, ruling out the explanation that failed final-state steering is caused by a tiny local basin.

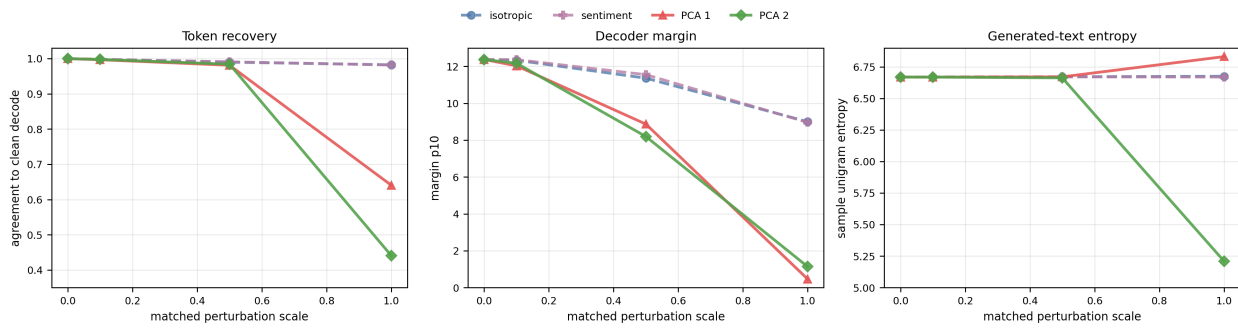


Figure 32: Directional reverse-basin navigation. Left: token agreement under isotropic and matched-norm directional perturbations. Middle: native margin under the same directions. Right: decoder entropy or quality proxy for the perturbed decodes. The final ELF basin is robust to isotropic and random directions but much narrower along dominant PCA directions, revealing anisotropy rather than a uniformly wide or tight basin.

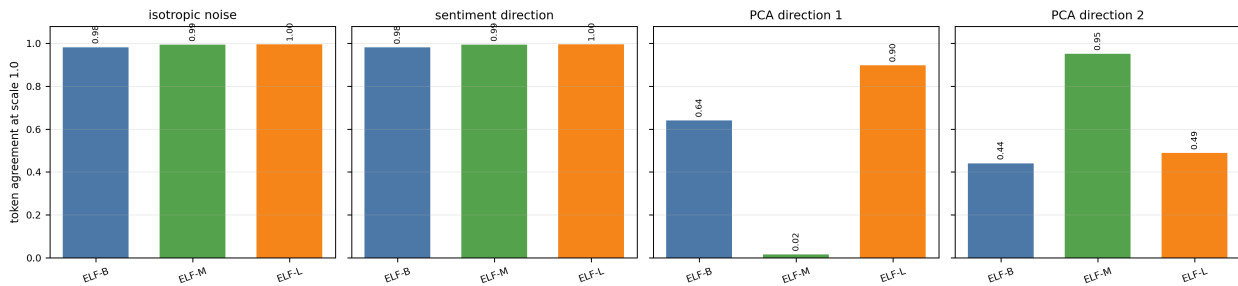


Figure 33: Cross-scale directional RBN. From left to right, the panels compare isotropic noise, a sentiment direction, the first PCA direction, and the second PCA direction at matched perturbation scale across ELF-B/M/L. Isotropic and sentiment directions remain mostly inside the final basin, while at least one high-variance PCA direction sharply reduces native-token agreement. The fragile direction changes with checkpoint scale, but anisotropy persists.

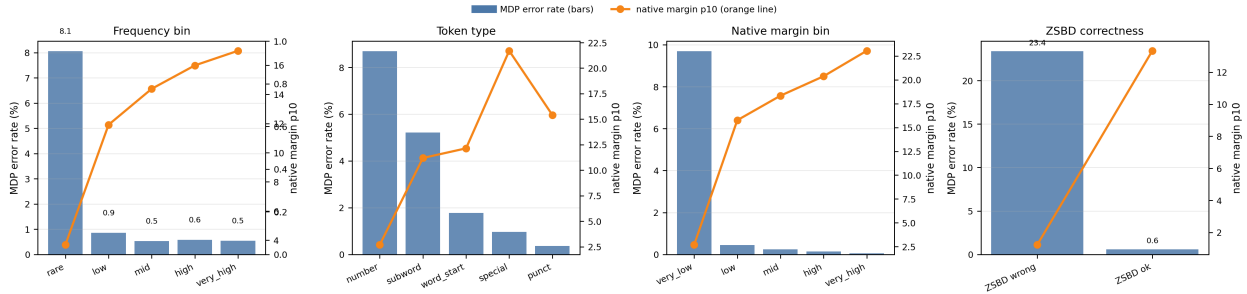


Figure 34: 32k MDP residual-tail analysis. Left: error rate by native margin bucket. Middle-left: overlap between MDP errors and ZSBD-hard tokens. Middle-right: token-frequency and token-type buckets. Right: position bucket effects. A single linear readout recovers 97.89% of native tokens on 4096 held-out generated samples, but the remaining errors concentrate in low-margin, ZSBD-hard, rare, numeric, and subword cases.

to decode, or that they are readable but do not fully return to the clean T5 interface manifold. We separate these explanations with a paired audit on 1024 generated ELF-B samples. For each native-decoded token sequence, we feed the exact token ids through the frozen T5 encoder, apply ELF’s latent normalization, and compare native-decoder target margins for this clean interface state, the last predicted clean state \hat{x}_T , the average of the last two clean predictions, and the final latent z_T . Figure 35 shows a lower-tail gap, not a global confidence collapse. Clean T5 states recover the same target tokens at 99.996% and have much deeper target-margin lower tails: their p01, p05, and p10 margins exceed z_T by 7.98, 4.53, and 1.56 margin units, respectively. The median gap is negative (-0.85), so generated states can be more confident on easy positions while remaining shallower in the fragile tail. Thus final ELF states are decoder-readable but still off the clean T5 manifold in the part that matters for residual calibration.

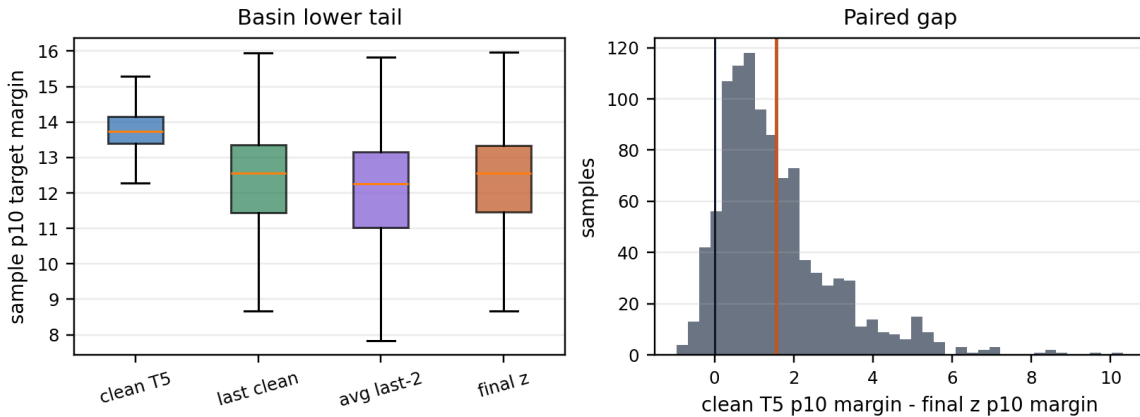


Figure 35: Paired clean-vs-generated decoder-basin depth. For the same generated token sequences, clean T5 interface states have a tighter and deeper lower tail than generated final states. Left: sample-level p10 target margin for clean T5, last predicted clean state, average of the last two clean predictions, and final latent. Right: paired p10 gap between clean T5 and z_T ; the orange line marks the mean gap (1.56) and the black line marks zero. The effect is concentrated in the lower tail rather than the median, supporting the view that the residual PPL gap is a tail-calibration issue rather than a failure of bulk readability.

Tail-gating check. A final check asks whether this residual tail is predictable enough to route selectively, rather than replacing the native decoder everywhere. We train the same 32k MDP linear readout and then form hybrid outputs: use the linear readout for bulk tokens, but route suspected tail positions to the native token decision. The oracle upper bound routes only the MDP errors; practical gates use only deployable signals such as low linear-readout confidence, MDP–ZSBD disagreement, and predicted rare/numeric/subword token types. Figure 36 shows the result. MDP alone has PPL 24.82 and 98.01% agreement on the 4096-sample held-out split. Routing the lowest-confidence 5% of token positions covers 94.6% of MDP errors and improves PPL to 23.85; routing the lowest-confidence 10% covers 98.8% of errors and reaches PPL 23.82, close to the oracle-tail upper bound (23.80) and native decoding (23.65). The broader practical gate routes 33.9% of positions and reaches PPL 23.81, but this is less parsimonious than the confidence gate. This tail-gated readout is a diagnostic, not a new decoder: most decisions are linearly readable inside the final basin, and the native decoder is most valuable on a small, predictable residual tail that can be targeted with lightweight routing heuristics.

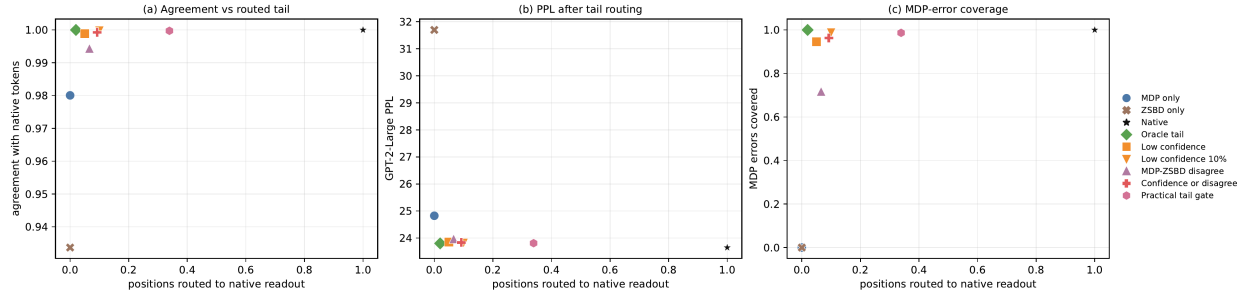


Figure 36: Tail-gated readout as a tail-calibration check. Left: native-token agreement versus the fraction of token positions routed from the linear readout to the native decision. Middle: GPT-2-Large PPL under the same routing policies. Right: fraction of MDP errors covered by each gate. Low MDP-confidence gates route only 5–10% of token positions yet cover most MDP errors and nearly close the PPL gap, supporting the view that the native decoder primarily calibrates a predictable residual tail on generated final ELF states.

5.11 PPL, MAUVE, and Decoder Calibration

Metric cross-checks. Figure 37 adds objective checks that prevent overclaiming. First, MAUVE does not perfectly track GPT-2 PPL, but the 2048-sample MAUVE estimate supports the qualitative schedule story: front-loading improves MAUVE for ELF-B (0.956 vs. 0.950 for fixed SC=3) and ELF-M (0.961 vs. 0.955 for fixed SC=5 and 0.945 for fixed SC=3). Second, entropy-matched decoder calibration shows that low PPL can be a decoder artifact. A learned linear decoder produces low-PPL argmax text, but only moderate token agreement with the official decoder; when sampled at a temperature chosen to approach the official decoder’s entropy, PPL worsens sharply. Third, the Cola-DLM VAE noise sweep shows a narrow decoder-compatible basin: clean recovery is almost perfect, but token recovery collapses rapidly around mid-noise corruption levels, exposing a sharp boundary in decoder compatibility.

The decoder results refine the direct-unembedding baseline. A direct linear map may be overly stringent, so we train small learned decoders from final ELF latents to the official decoder’s argmax tokens. This is a more targeted baseline because the target interface is the official decoder itself. With a 1024-latent matching set, the two-layer multi-layer perceptron (MLP) decoder obtains lower GPT-2-Large PPL than the official decoder (16.29 vs. 18.25), but token agreement to the official decoder is only 0.737. After entropy-matched sampling, its PPL rises to 46.34 and agreement drops to 0.631. Figure 38 shows the per-sample operating regions behind this effect: schedules and decoders occupy clouds in the PPL–entropy plane rather than a single scalar ranking. This does not contradict the later 32k MDP result. MDP uses many generated final states to imitate the native argmax interface and is judged primarily by agreement; the small-decoder calibration test shows that low external PPL alone can validate the wrong operating region. The result is more subtle than direct failure: small decoders can reduce PPL, but they do so by changing the operating region. This supports the claim that the official decoder is not an incidental readout. It defines the basin in which the denoiser’s final states are meaningful.

We also run a model-level entropy calibration against GPT-2-small (Figure 39). This is a conservative check prompted by the known PPL failure mode in diffusion LMs. We decode the same ELF final logits under temperatures $T \in \{0.4, 0.6, 0.8, 1.0, 1.2, 1.5\}$ and generate GPT-2-small samples under a temperature sweep. ELF’s final decoder is already extremely sharp: for front-loaded ELF-B, increasing decoder temperature from 0.4 to 1.5 changes GPT-2-tokenized unigram entropy only from 6.891 to 6.895, while token agreement to argmax remains above 0.991. At the closest GPT-2-small entropy point ($T = 0.8$, entropy 6.858), GPT-2-small has lower GPT-2-Large PPL (12.23 vs. 24.90 for front-loaded ELF-B) and higher distinct-2 (0.488 vs. 0.324). At lower GPT-2 temperatures, PPL becomes extremely small but repetition rises sharply, reproducing a PPL artifact in a simple AR baseline. This result prevents a misleading claim: our front-loaded schedule is not an entropy-matched replacement for AR generation. It is evidence that ELF trajectories expose reliability signals, while PPL/entropy frontiers must be reported explicitly.

Figure 40 gives the aggregate margin sweep supporting Theorem 1. Clean final latents have token recovery 0.989 and a positive-margin fraction 0.989. With only a mild corruption, token recovery drops to 0.870 at $t = 0.95$ and 0.767 at $t = 0.90$. At $t = 0.50$, recovery is 0.532, and the 10th percentile margin is strongly negative. A first-order boundary estimate on sampled token positions gives a median distance of 3.00 but a 10th percentile distance of only 0.063, indicating that many positions sit close to a decoder boundary even when average margins look large.

The per-token view is even more diagnostic. Figure 41 bins 663,552 token positions by clean margin and latent

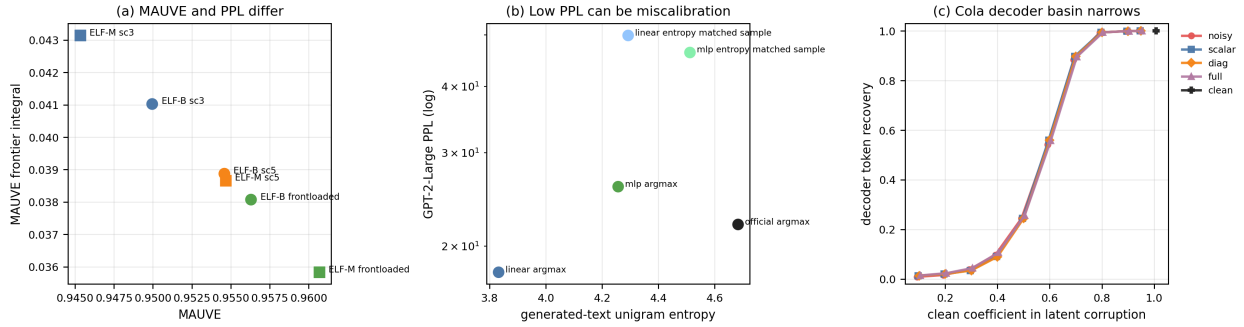


Figure 37: Multi-metric and boundary evidence. (a) MAUVE and PPL can rank schedules differently. (b) A small decoder can obtain low PPL by miscalibration; entropy matching exposes the issue. (c) Cola-DLM latents have a narrow decoder-compatible basin under noise.

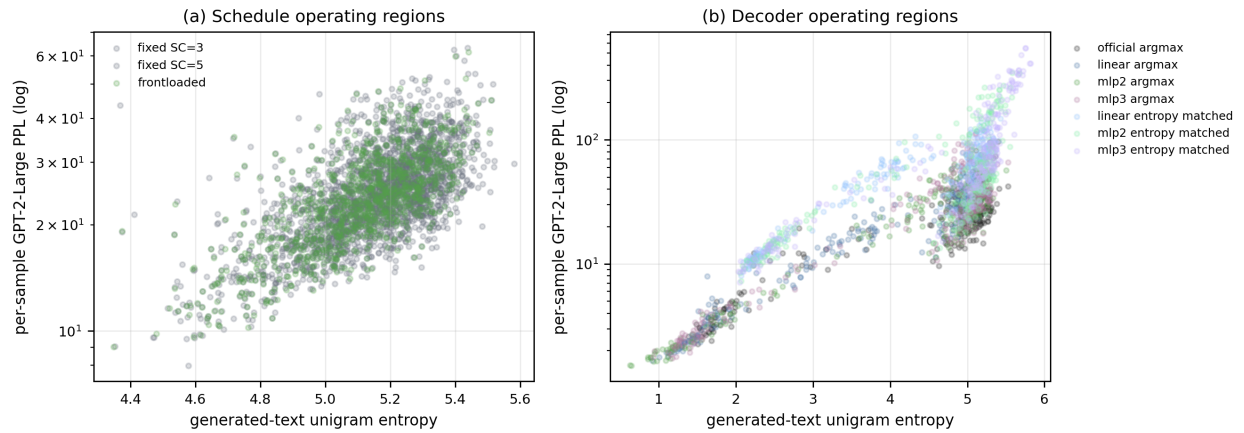


Figure 38: Per-sample operating regions. Left: schedule choices move samples along a PPL-entropy cloud rather than a single scalar. Right: learned decoders occupy different entropy/PPL regions from the official decoder, so low PPL is not sufficient evidence of decoder fidelity.

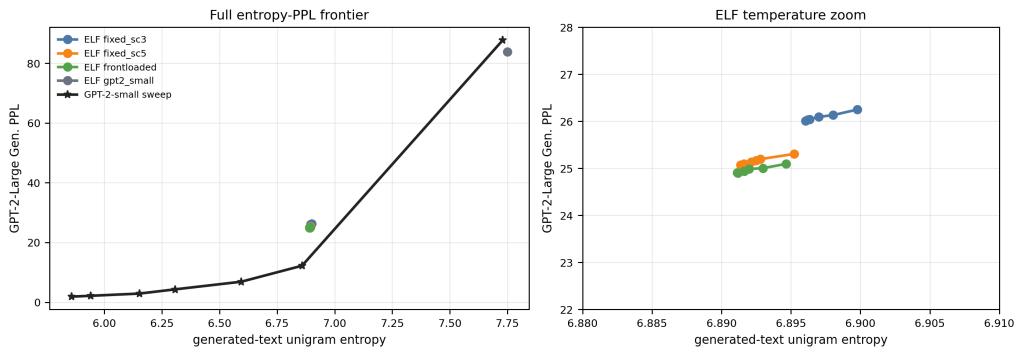


Figure 39: Entropy-calibrated ELF vs. GPT-2-small. Left: full temperature sweep in the PPL-entropy plane. Right: zoom near the closest entropy-matched operating points. ELF final decoding is nearly argmax-like across temperatures; the comparison is not an ELF win claim, but a demonstration of the frontier hidden by PPL-only reporting.

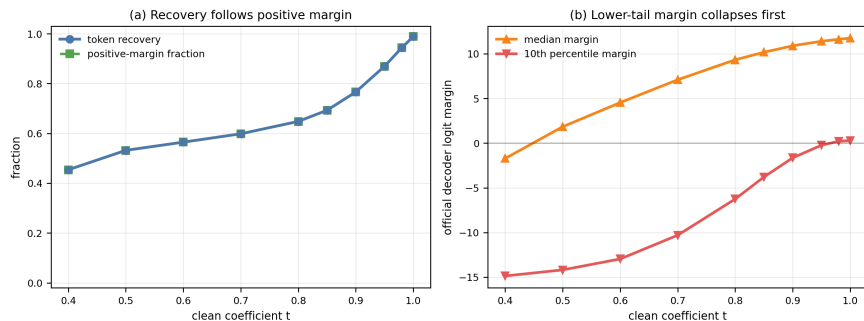


Figure 40: Decoder-margin basin test. Left: token recovery and positive-margin fraction as final ELF latents are corrupted away from the clean endpoint. Right: median and 10th-percentile native logit margins under the same corruption. Recovery and margin collapse together, empirically matching the decoder-margin bound.

error norm. Low-margin tokens collapse quickly: recovery falls from 0.94 for errors below 0.96 to below 0.10 for errors above 11.9. High-margin tokens remain stable under much larger errors: recovery is still 0.981 in the largest error bin. This is exactly the operational content of Theorem 1. The latent error alone is not predictive; the same error has different effects depending on local decoder margin.

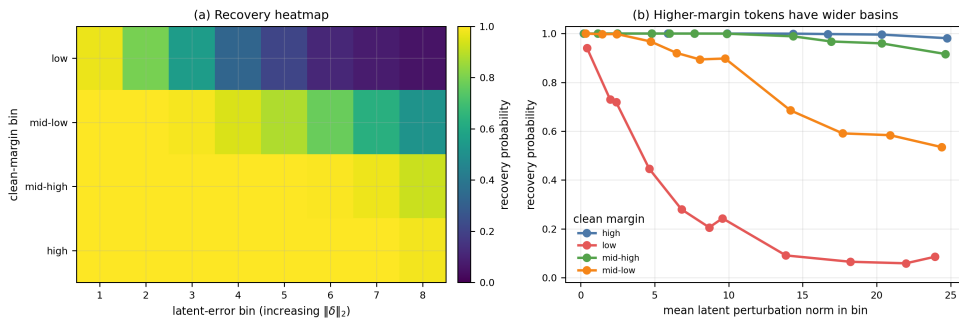


Figure 41: Per-token decoder-margin evidence. Left: token recovery as a function of latent error and clean decoder margin. Right: empirical recovery curve grouped by margin/error regime. For the same latent error, high clean margins preserve tokens while low margins collapse, turning the decoder-margin bound into a measurable diagnostic.

5.12 Cola-DLM Boundary Case

Boundary case. Cola-DLM provides an architectural contrast rather than a parallel benchmark. It learns a VAE latent space and trains a DiT prior over it, whereas ELF uses a frozen T5 encoder with a shared denoiser and decoder. Despite these differences, both systems face the same diagnostic question: can a continuous state be safely handed to a decoder after a noisy trajectory? In Cola, clean VAE latents reconstruct with very high fidelity—a clean reconstruction metric alone would suggest the interface is safe. The noise sweep reveals otherwise: recovery remains high near $t = 0.9$ but collapses rapidly between $t = 0.7$ and $t = 0.5$. A balanced four-GPU DiT trajectory sweep sharpens the interpretation. Across 512 samples per classifier-free guidance (CFG) [20] setting, decoder entropy drops from about 5.7 nats to 0.49/0.32/0.15/0.19 for CFG 0/1/3/7, and CFG 3–7 reaches a stable entropy ≤ 1 basin around steps 12–13. But teacher-forced target-token recovery under our diagnostic remains only 0.8–4.4%, so this is prior transport into a decoder-confident basin, not recovery of our held-out teacher target. This teacher-forced diagnostic does not evaluate Cola-DLM’s full free-generation benchmark quality. The boundary case reinforces the broader point: latent diffusion language models should report decoder-basin robustness under realistic noise levels, not only clean reconstruction fidelity.

5.13 Training-Side Validation: Widening the Basin

Training-side prediction. The basin view makes a training-side prediction: decoder training should not only classify clean latents, but widen the native basin around plausible noisy latents. The released ELF training recipe [22],

implemented in PyTorch, already contains such a mechanism. In OWT training, 20% of examples take a decoder branch, and decoder inputs are sampled by mixing clean T5 latents with scaled Gaussian noise. We test this directly with short ablations using the official implementation on four RTX 3090 GPUs.

The result is interventional in the limited but useful sense that we vary one training ingredient at a time. With no decoder-input noise, clean recovery is high (0.951), but retention collapses under mid-noise: only 47.0% of clean recovery remains at $t = 0.6$. With the official-like noise scale of 5, clean recovery is still high (0.995), but retention rises to 94.4% at $t = 0.6$ and 81.7% at $t = 0.5$. Too much noise is not monotone: scale 10 weakens the interface. Varying the decoder-branch frequency separates transport from basin widening. A pure denoising run cannot decode; a decoder-only run creates a broad synthetic basin but learns no flow objective. The mixed objective balances the two.

We also test a tempting repair suggested by Theorem 1: add an explicit hinge-style margin penalty to the decoder CE branch. In this limited-scale exploration, the penalty preserves clean recovery and is optimized during training, but after both 5k and 10k steps it still does not beat the noisy-CE baseline on mid-noise retention or clean margin tail. The result does not rule out all margin objectives; it shows that, in these short runs with the official implementation, directly maximizing a scalar logit gap is not a drop-in replacement for training the decoder on the neighborhood the denoiser must actually visit. This completes the training-side check: decoder-input noise widens the basin in practice, while the tested margin penalty does not, reinforcing the distinction between training a decoder on the local neighborhood of expected noisy latents and directly maximizing per-sample scalar margins.

5.14 Summary of Ruled-Out Explanations

The experiments collectively rule out five simple stories. First, continuous diffusion is not explained by Gaussianity alone, because covariance controls can be denoisable without being recoverable. Second, it is not explained by token identity alone, because word-shuffled embeddings preserve token identities but fail the order-sensitive diagnostics. Third, ELF’s final step is not merely a linear readout, because small decoders change calibration and reduce agreement. Fourth, sampler gains should not be summarized by PPL alone, because MAUVE, entropy, and repetition expose different frontier movements. Fifth, clean latent reconstruction is insufficient, because Cola’s decoder basin collapses under the noise levels that a prior must traverse.

These controls are small by design. The relevant baseline for linear denoising is a covariance-matched control, not a competing DLM. The relevant baseline for the decoder is a small learned decoder trained to imitate the official decoder, not direct unembedding alone. The relevant baseline for trajectory reliability is a shuffled or time-reversed signal, not a stronger policy. Each control preserves a superficial statistical property while removing the linguistic property the diagnostic is meant to test. Small negative or boundary results carry weight because they remove plausible but incorrect explanations, and each control is tailored to a specific confound: covariance preserves second-order statistics while removing linguistic content, and shuffled controls preserve bag-of-words structure while breaking contextual order.

6 Discussion

Continuous language diffusion is a property of an interface, not a latent space alone. This reframes several design questions. A better encoder is not necessarily the one with the lowest linear denoising MSE: a covariance-matched Gaussian can be denoisable but linguistically vacuous, so the axes must be reported jointly. A stronger decoder is not necessarily the one with the lowest external PPL; it must preserve calibration, diversity, and fidelity to the intended interface. A better sampler should not be judged only by PPL, because stronger churn or guidance can improve fluency at the cost of diversity and semantic accuracy, moving samples along trade-off frontiers rather than toward an absolute optimum.

Resolving the two hypotheses. The evidence does not reduce ELF to either the network hypothesis or the interface hypothesis. Linear denoisers and low-rank bottlenecks fail in ways that show capacity and trajectory computation matter. The trajectory audits then show what that computation is aligned to: transporting noisy predictions into a decoder-readable region made readable by the pretrained T5 interface and its native decoder. After entry, ZSBD and MDP reveal that most token decisions are simple on the generated final manifold, while the residual tail still needs native decoder calibration. The success of ELF is therefore a cooperation between a structured pretrained interface and a denoising network that learns a safe transport path through it.

The front-loaded schedule and BGEE are minimal by design. Their purpose is to demonstrate that internal trajectory signals carry actionable information. They are not optimized systems results: BGEE reports algorithmic NFE savings under a margin monitor, and an optimized wall-clock implementation would need either a cheap margin proxy, sparse monitoring, or dynamic batching. The larger contribution is a protocol that can be applied before expensive training: if a candidate representation–decoder pair fails the multi-axis test, scaling the denoiser is unlikely to resolve the underlying mismatch.

A unified view: denoising as basin navigation. The closest conceptual analogy is a “propose, compare, and enter basin” view of generation. In ELF, early denoising proposes diverse candidate clean states with low margins. In the middle trajectory, self-conditioning disagreement is largest, and candidate predictions become readable but are not yet in the final-token basin; this pattern is statistically consistent with revision, but it is not a direct observation of the denoiser’s internal algorithm. Late denoising enters the native decoder’s high-margin basin, where final-token agreement approaches one and decoder entropy collapses. In Cola-DLM, the VAE decoder is highly reliable near the clean manifold but rejects mid-noise latents sharply. This view suggests that future latent DLMs should report not only prior quality or reconstruction quality, but also the geometry of the transition region where the prior must hand states to the decoder.

The interface phase diagram sharpens this view without changing the scope of the paper. A static basin says which final states are decoder-readable; the phase diagram asks when alignment begins, how wide the competition region is, and which tokens fail to lock early. The contribution is the measurement program: turn decoder-basin entry into a time-resolved diagnostic with crossing phases, transition widths, token-wise tails, sampler/scale checks, and readout probes. We use the phase language empirically, not as a claim of a thermodynamic phase transition.

From diagnostic to minimal probes. BGEE, ZSBD, and MDP follow a representation–first diagnostic style: before training a new generator, ask what the representation already makes easy. In our setting, the native decoder margin tells us when the denoising trajectory has reached a usable textual basin, and generated final latents tell us whether that basin is simple enough for a token lookup or minimal readout. BGEE uses the first signal to stop early. ZSBD tests the no-newly-trained-readout limit by decoding through frozen T5 token-embedding nearest neighbors. MDP then quantifies how much decoder complexity remains after basin entry. These probes are intentionally small, and their role is measurement. They expose concrete control variables that future samplers, decoders, or training objectives can optimize, from margin-thresholded early stopping to token-level routing and lightweight margin proxies. Table 4 condenses the three probes into their measured basin property, key result, and interpretation.

Table 4: Basin report for the three minimal probes. The probes measure timing, token alignment, and linear recoverability within the same basin-navigation mechanism.

Probe	Exploits	Key result	Interpretation
BGEE	Basin-entry timing	Held-out Margin-12 gate saves 16.6/23.4/27.6% NFEs on B/M/L	Stopping probe, not a tuned sampler
ZSBD	Token-embedding alignment	Frozen lookup recovers 93–96% native tokens with no newly trained readout	Readout probe; decoder still calibrates tail
MDP	Local basin linearity	4k linear readout recovers about 94% agreement; 32k reaches 97.9%	Interface-complexity probe, not replacement

The companion stress tests in Table 5 explain why the probes are credible but bounded: they test basin sharing, intervention direction, token-wise entry, ZSBD geometry, and residual-tail predictability without turning the paper into a new sampler or decoder proposal.

Stress tests around the probes. The three probes above are minimal, so we add stress tests that ask whether the basin is shared, intervenable, token-wise, and geometrically identifiable (Table 5). Cross-decoder transfer is the cleanest generality check available inside the public ELF family: final latents generated by one checkpoint can be decoded by another checkpoint’s decoder with very high agreement to the source checkpoint’s native tokens. This argues against the strongest artifact explanation, namely that the denoiser merely navigates to a private decoder quirk. The supported claim is narrower: the basin is largely shared across ELF-B/M/L decoders that use the same T5-small latent and token interface. We do not extrapolate this result to independently trained decoders with different architectures or vocabularies.

The paired intervention test gives the most direct intervention evidence. At a mid-trajectory step, we replace the predicted clean latent with a token-basin projection, an anti-basin perturbation, or a random direction matched in scale,

Table 5: Additional fixed-checkpoint stress tests around the three minimal probes. Each row reports the measured effect and the corresponding interpretation.

Stress test	Key result	Interpretation
Cross-decoder transfer	B/M/L final latents decoded by the other two ELF decoders retain high source-native agreement: B→M/L gives 0.988/0.987, M→B/L gives 0.996/0.996, and L→B/M gives 0.995/0.996.	Evidence for shared ELF-family basins under the same T5-small interface, not for universal T5 geometry.
Causal basin intervention	At step 16 with $\alpha = 0.5$ on 512 samples, projection gives $\Delta p10 = +0.085$ and $\Delta PPL = -0.49$; anti-basin gives -0.186 and $+0.49$; random-matched is near zero ($+0.009, -0.08$).	The basin direction behaves like a controllable variable, but this pilot is not a tuned guidance policy.
Same-start multi-path SDE	For 256 fixed initial states with four independent SDE streams each, final token agreement across paths is only 29.9% on average, while the mean final 10th-percentile margin remains 12.37.	SDE sampling enters high-margin basins, but the selected token basin is path-dependent; the claim is not a unique attractor.
Long-form topic boundary	On 1000 unconditional ELF-B samples, adjacent-sentence cosine is OWT-like (0.413/0.396 for SDE64/SDE32 vs. 0.386), but first-to-last cosine is far lower (0.064/0.067 vs. 0.292). ODE32 improves first-to-last cosine to 0.110, still far below OWT. SDE64 improves geometric PPL over SDE32 (20.3 vs. 25.1) without improving this drift.	Decoder-basin entry supports local token readability and semantic families, but it does not certify document-level discourse planning.
Mid-SC causal intervention	On 256 matched-noise samples, zeroing or freezing mid-window self-conditioning worsens PPL from 24.47 to 42.63/32.69 and lowers margins; shuffling lowers PPL to 21.18 but collapses entropy and repetition.	Mid-trajectory self-conditioning is intervention-sensitive, but PPL alone can validate collapsed text.
Token-wise entry	On 512 samples and 523,578 tokens, persistent native-token entry reaches 99.96%; persistent entry with margin at least 8 reaches 94.7%, but numeric and rare tokens are much weaker (79.8% and 81.4%).	Basin entry is token-wise, so sample-level BGEE has a natural ceiling and suggests easy-token freezing.
ZSBD geometry	Frozen-embedding cosine gives 93.4% agreement; unnormalized dot-product lookup gives 81.7%; Euclidean lookup gives 3.4%; cosine after whitening gives 4.3%; permuted labels are nearly zero.	ZSBD relies on labeled angular token geometry, not vector norm, Euclidean proximity, or frequency alone.
Residual tail targeting	A ZSBD-wrong gate covers 6.63% of positions but contains 73.4% of 32k MDP errors; the rare-token quintile contains 76.3%.	The native decoder remains important for the hard tail; targeted repair should focus on few positions rather than replace the decoder wholesale.
Sampler extension checks	ZSBD confidence routing, a 4.7k-parameter margin proxy, and equal-budget SC-update rejection expose useful signals; local token-wise latent freezing and one-step projection from noise fail.	These are compiler and future-sampler signals, not production samplers.

then continue denoising with the same noise stream. On a 512-sample four-shard expansion with $\alpha = 0.5$, projection improves the final margin tail and lowers GPT-2-Large PPL on a 256-text audit ($\Delta p10 = +0.085$, $\Delta PPL = -0.49$), while the anti-basin perturbation worsens both ($\Delta p10 = -0.186$, $\Delta PPL = +0.49$). The matched random control remains close to neutral ($\Delta p10 = +0.009$, $\Delta PPL = -0.08$). Projection is not a competitive sampler–token agreement to the unedited baseline is only about 0.72—but it shows that basin direction is not merely a retrospective correlation.

Two additional trajectory stress tests bound the phase-diagram interpretation. First, we fix each initial noise state and run four independent SDE noise streams. On 256 starts, the final paths agree on only 29.9% of valid tokens on average (10th percentile 21.4%), even though each path ends in a confident basin with mean 10th-percentile margin 12.37. Thus stochastic ELF sampling should be described as path-selected entry into high-margin token basins, not convergence to

one unique attractor that is determined solely by the initial noise state. Re-exporting all four paths gives a semantic counterpart: the median cross-path document cosine is 0.222, far above random cross-start pairs (0.023), but still far from a unique shared document. This path-selection result raises a document-level question: do high-margin token basins also certify coherent discourse? They do not under the tested unconditional settings. On 1000 ELF-B samples, adjacent-sentence similarity is close to OWT (median cosine 0.413 for SDE64 and 0.396 for SDE32, versus 0.386 for OWT), but first-to-last sentence similarity is much lower (0.064 and 0.067 versus 0.292). The available ODE32 samples improve first-to-last cosine to 0.110, but remain much closer to SDE than to OWT; deterministic sampling therefore changes the boundary modestly without closing it. A gamma and self-conditioning sweep improves some local transition metrics, but no tested setting restores OWT-like first-to-last topic stability. Per-sample GPT-2-Large PPL confirms that this is a distinct blind spot: SDE64 improves geometric PPL over SDE32 (20.3 versus 25.1) while preserving nearly the same first-to-last drift, and ZSBD has worse geometric PPL (32.6) but slightly better first-to-last stability (0.088). Within generated groups, first-to-last sentence cosine has only weak correlation with log PPL (Spearman $\rho \approx -0.16$ to -0.22). More denoising steps therefore refine local token likelihood within a selected basin family, but they do not choose a more coherent document-level family under these settings. Likewise, ZSBD’s geometrically smoother nearest-neighbor mapping yields marginally better topic continuity than the native decoder (first-to-last cosine 0.088 vs. 0.064) at the cost of calibration (geometric PPL 32.6 vs. 20.3), suggesting that sharper per-token decision boundaries may amplify semantic drift introduced by SDE noise during the competition phase. High-margin basin entry supports local token readability and path-selected semantic families; it does not certify document-level discourse planning.

Second, we corrupt self-conditioning only in the mid-window where the audit shows strongest disagreement. On 256 matched-noise samples, zeroing the mid-window SC state worsens PPL from 24.47 to 42.63 and lowers the 10th-percentile margin from 12.14 to 9.90; freezing it worsens PPL to 32.69 and lowers the 10th-percentile margin to 10.54. Shuffling SC across the batch lowers geometric PPL to 21.18, but sample unigram entropy collapses to 3.84 and repeated 4-gram fraction rises to 24.2%. The mid-SC phase is therefore intervention-sensitive and temporally localized, but lower PPL can still be a collapse artifact, reinforcing the necessity of multi-metric evaluation when perturbing internal trajectory states.

Finally, token-wise entry and geometry ablations explain why the probes work and where they should fail. Most positions enter the native basin before the final step, but they do so at different phases; a 512-sample audit shows that persistent native-token entry reaches 99.96% of token positions, while persistent entry with margin at least 8 reaches 94.7% and leaves a sequence-level tail. The p90 sample still has 453 positions that enter the margin-8 basin late or never, and the longest late span has p90 length 17. This makes a token-wise “freeze easy, continue hard” policy more promising than adding another sample-level gate. ZSBD’s strength is also specific: cosine nearest-neighbor lookup in the labeled T5 token table works, while Euclidean distance, whitening, or label permutation destroys it. This does not mean that the frozen token table itself carries word order. The denoising trajectory supplies contextual, ordered latent states; the token table supplies labeled angular anchors for reading out those states. The remaining MDP errors concentrate in ZSBD-wrong, rare, numeric, and subword positions, so the natural repair target is the tail rather than a larger bulk readout.

Several additional fixed-checkpoint analyses, summarized in Figure S8, refine this boundary without adding another probe. Clean T5 states are deeper than generated ELF final states in the lower margin tail, same-start SDE paths select different high-margin basins, mid-trajectory self-conditioning is intervention-sensitive, and cheap confidence or proxy signals identify many tail cases. Together with the token-wise and residual-tail audits above, these signals suggest a shared fragile-token phenotype: late basin entry, low native margins, ZSBD disagreement, and MDP residuals repeatedly concentrate on rare, numeric, subword, and boundary-near cases. A final overlap audit within the held-out 32k residual-tail sample supports this reading: low native-margin rows are almost always MDP-hard and usually ZSBD-hard, while MDP errors are frequently rare or ZSBD-wrong. This is not a claim that every diagnostic selects the same token positions, and the document-level topic audit is not token-aligned; rather, the recurring tail structure identifies where future interfaces should allocate calibration or verification. The negative counterparts are equally useful: local token-wise freezing and one-step projection show that simple readout after basin entry does not imply simple transport into the basin.

We also tested an additional boundary case: using a sentiment direction in the final latent basin with a margin gate. The first version was essentially negative: final-basin editing shifted target success only marginally while random-direction controls remained close. Directional RBN refined the interpretation. The sentiment direction is not rejected by a tiny basin; it is a safe direction that mostly preserves token identity. We therefore ran an adaptive line-search version that pushes the same direction until the native margin lower tail reaches a safety threshold. Inside the high-quality basin,

the edit is still mostly absorbed: with safety margin 2, target success rises from 68.5% to 72.9%, token agreement remains 95.9%, and PPL stays near the baseline. At the boundary, the attribute can be forced: safety margin 0 reaches 99.7% target success, but token agreement falls to 61.6% and PPL jumps to 51.0.

How to interpret the probes. BGEE, ZSBD, and MDP should be interpreted as measurements of one mechanism rather than as separate optimized methods. BGEE measures *when* a trajectory enters the basin, ZSBD measures whether final states are *geometrically aligned* with token embeddings, and MDP measures how *linearly recoverable* the native interface is on generated states. None is presented as a replacement for a tuned sampler or the native decoder. This is also why we keep BCD as a boundary result: the same basin that makes readout simple can make post-hoc semantic editing hard.

We then tried a stronger repair: use the native decoder Jacobian itself. Instead of moving along an encoder-space Yelp Polarity direction, we backpropagate through the ELF decoder to increase logits of positive sentiment tokens, and we apply the same margin line search. This direction is more efficient, but it exposes the same basin trade-off. At safety margin 4, target success improves from 65.6% to 76.6% while PPL rises mildly from 24.9 to 26.8 and only 2.6% of tokens change. At safety margin 2, target success reaches 99.2%, but PPL rises to 41.7 and 10.8% of tokens change. At the boundary, the classifier is fully controlled but text quality collapses. A token-selective variant that perturbs only the top 6.7% sentiment-evidence positions is almost completely absorbed by the basin: target success stays at 65.6% and token agreement remains above 99.4%. Thus final-basin editing is not impossible, but clean control requires moving a nontrivial portion of the sequence through the decoder Jacobian. This is a useful boundary for representation-first readout claims. ELF final states are not a generic editable semantic canvas. Reliable control likely needs trajectory-level or training-time conditioning, whereas the final basin is best used for stopping and interface probing.

We test this with a trajectory-level repair. Instead of editing only the final state, we apply the decoder-gradient direction at one denoising step, replace the predicted clean latent, and continue the trajectory with the same SDE noise stream. This controlled repair asks whether earlier intervention is less constrained by the final basin. On 128 ELF-B samples, intervening at step 16 with a loose margin threshold raises target success from 64.1% to 69.5% while keeping PPL essentially unchanged (24.6 to 24.4), but it changes 23.7% of tokens. Later or more margin-conservative interventions are mostly absorbed. This supports the boundary interpretation: trajectory-level guidance can move the attribute frontier slightly without immediate PPL collapse, but clean controllable generation will likely require training-time conditioning or a guidance objective designed for control, not post-hoc final-basin editing.

The diagnostic suggests a practical pretraining question: can we design encoders whose representations are explicitly diffusion-ready under all axes, not only good for masked prediction or next-token prediction? T5 contextual embeddings appear strong because they combine denoisability, contextual order, and decoder compatibility in the ELF interface, and their span-corruption pretraining may be unusually well matched to local corruption and recovery. This is a feature of the studied interface, not a universal theorem about all continuous language states. The protocol also reveals why blindly swapping encoders is risky. BERT-like, RoBERTa-like, GPT-like, token-level, byte-level, and compressed-tokenizer representations may each fail on different axes. A future compressed-tokenizer study for DLMs should therefore measure not only compression ratio and LM loss, but also decoder margin and recoverability under Gaussian corruption.

A central scope limitation is that ELF depends on a frozen pretrained T5 encoder. This makes it important to distinguish representation modeling from fully self-contained language modeling. ELF demonstrates that flow transport can work well once a strong contextual interface is given; it does not by itself show that a continuous language space can be self-bootstrapped at frontier scale. The diagnostic protocol turns this dependency into a measurable object. It does not assume the state space is frozen: it can be applied to frozen T5 embeddings, learned VAE latents, compressed tokenizers, or future co-evolved semantic encoders. ELF succeeds because T5 contextual embeddings happen to satisfy the interface well. Cola-DLM asks a more upstream question: can the representation itself be learned and co-adapted with the prior? Our Cola boundary results show why reconstruction alone is not enough for that path. A learned latent should be evaluated by denoisability, semantic recovery, order sensitivity, decoder-basin width, and prior compatibility, not by clean VAE recovery alone. From this perspective, token budget accounting is incomplete unless the representation interface is also characterized.

On the decoder side, ELF’s shared decoder is sometimes described as a simplification, but our results suggest a more nuanced view. The final decoder step is a nonlinear interface trained under a CE objective; it is not merely the last flow step and not merely a matrix multiplication. Sharing weights may be useful because the denoiser and decoder learn compatible hidden states, but the benefit should be evaluated against fair separate decoders with sufficiently broad hyperparameter ranges. Our small-decoder results show that even when a decoder is trained directly on final ELF latents, PPL and token agreement can diverge. This motivates future work on decoder-aware flow objectives, margin

regularization, or explicit basin widening.

Training-time basin widening. The diagnostic also predicts which training tricks should matter. Decoder-input noise should help because it trains the decoder on a neighborhood rather than only on the clean manifold; MSE auxiliary losses can prevent the latent from becoming easy to classify but hard to denoise; adaptive timestep sampling should focus compute where decoder compatibility changes fastest. The released ELF training recipe [22] already follows this principle: OWT training uses a decoder branch on 20% of examples and constructs its decoder input by mixing clean T5 latents with Gaussian noise at scale 5.0. This is the basin-widening training predicted by the margin view, not an incidental implementation detail. LDLM’s joint-training recipe independently uses related decoder-input-noise and decoder-stabilization losses [40]. In this sense, LDLM is convergent empirical evidence rather than a competing explanation: once the representation is allowed to co-evolve with the prior, the decoder basin must be widened during training. Draft-conditioned refinement [66] is another indication that decoder readability matters, but our main evidence is the fixed-checkpoint measurement of when ELF basin entry happens, how it changes with trajectory phase, and which operations become reliable after entry.

We also ran a small 4-GPU training ablation with the official PyTorch ELF-B code to test this prediction directly. Holding the architecture and training length fixed, a clean-only decoder branch reaches high clean token recovery (0.951) but retains only 47.0% of that recovery at a mid-noise state ($t = 0.6$) and 42.1% at $t = 0.5$. Adding decoder-input noise widens the basin substantially. A mild scale of 1 reaches nearly perfect clean recovery (0.999) and retains 76.4% at $t = 0.6$, while the official-like scale of 5 reaches 0.995 clean recovery and retains 94.4% at $t = 0.6$ and 81.7% at $t = 0.5$. Very large noise is not monotonic: scale 10 weakens clean recovery (0.917) and has lower retention than scale 5. Thus the official-style decoder-noise branch is not merely a robustness trick. It trains a decoder-compatible neighborhood around clean T5 latents, exactly the basin-widening effect predicted by the interface view.

Varying the frequency of the decoder branch sharpens the same conclusion. With the noise scale fixed at 5, a pure denoising run learns the L2 branch but has essentially zero clean token recovery, showing that transport training alone does not create a token interface. A tiny 5% decoder branch already creates a usable decoder (clean recovery 0.962), but its 10th-percentile margin is much smaller than the official-like 20% branch (1.87 vs. 6.11). At the other extreme, a decoder-only run has the strongest synthetic noisy-latent basin (retention 0.981 at $t = 0.6$), but no denoising loss at all. This separates two competencies that are often conflated: the decoder branch can widen the basin, but the flow branch is needed to transport Gaussian states into it. The useful training recipe is therefore not “more decoder” or “more denoising” in isolation, but a balance between transport and basin widening.

We also tested the most literal repair suggested by Theorem 1: add an explicit top-1-vs-runner-up margin penalty to the decoder branch while keeping the decoder-input noise scale at 5 and the decoder branch at 20% of examples. At 5k steps, clean token recovery remains unchanged (0.9946 vs. 0.9948), but retention under corrupted latents drops from 0.944 to about 0.912 at $t = 0.6$ and from 0.817 to about 0.787 at $t = 0.5$; the clean 10th-percentile margin also decreases. We then extended the official-like baseline and the strongest margin run to 10k steps. The margin objective is clearly optimized—its training margin loss decreases from about 0.85 to 0.56 and clean recovery reaches 0.998—but it still does not surpass the noisy-CE baseline: retention at $t = 0.6$ is 0.973 vs. 0.979, retention at $t = 0.5$ is 0.880 vs. 0.894, and the 10th-percentile margin is 7.76 vs. 8.40. The negative result is useful but limited: in these short runs with the official implementation, decoder robustness did not improve under the tested scalar margin penalty. Noisy CE trains a local calibrated basin around states the denoiser is likely to visit, while the blunt margin penalty can optimize its own objective without producing the widest off-manifold basin.

The same basin constraint applies to few-step and one-step language generation. Methods such as FMLM and CDLM reduce sampling depth directly [1, 29]. Drifting Models [11] raise an even sharper question: can the iterative process be moved from inference into training? Our results suggest a language-specific constraint. A direct map from noise to text latents is useful only if it lands inside the decoder-compatible basin, not merely near the clean latent under MSE. A natural follow-up experiment is a small drift head trained on ELF trajectories and evaluated by the same margin, entropy, and recovery diagnostics used here.

PPL remains useful because it is sensitive, well understood, and cheap, but it should not be the sole metric for latent or embedded DLMs. We treat it as necessary but not sufficient: a method that worsens PPL under matched entropy is unlikely to be useful, but a method that improves PPL alone has not been adequately validated. A sampler can improve PPL by reducing entropy, increasing repetition, or moving closer to high-frequency reference text. MAUVE, JS divergence, repetition, and entropy provide complementary views, and decoder agreement is needed when the sampler changes the final-state distribution. The diagnostic framing therefore changes the usual sampler question from “which curve has the lowest PPL” to “which part of the interface frontier has moved, and what was traded away?”

Tri-mode systems such as NemoTron-Labs-Diffusion [14] make continuous-diffusion diagnostics more relevant. If diffusion is one inference mode inside a larger autoregressive model, the system may inherit the AR backbone’s fluency while still exposing diffusion-specific interface risks. Trajectory reliability signals could become a routing criterion: use diffusion when the trajectory is stable, fall back to AR or self-speculative verification when decoder margins are small. Conversely, if tri-mode diffusion lacks such internal reliability signals, that would mark an important boundary beyond which the ELF-style mechanism does not cleanly generalize.

ELF’s design naturally favors fast parallel generation over sequential deliberation. A fixed-step sampler can produce an entire sequence at roughly fixed denoising depth, which is attractive for latency-bound generation. But this is not the same capability as chain-of-thought reasoning or long-horizon planning. Autoregressive models condition on their own intermediate tokens and can externalize computation through a written chain [61]; embedded diffusion compresses this process into a continuous trajectory that is later discretized. Hybrid systems such as block diffusion [2] and tri-mode AR/diffusion/self-speculation models [14] explore this design space from the architecture side. Our diagnostic clarifies the interface trade-off. Parallel denoising is plausible only if the representation-decoder interface is reliable enough that the model does not need token-by-token verification. For tasks that require global consistency or reasoning, the most likely path is hybrid: continuous denoising for fast local fluency and semantic organization, followed by AR-style verification, correction, or self-speculation for long-horizon decisions.

Discrete DLMS avoid the Gaussian-noise puzzle by keeping corruption in token space, usually through masking or remasking [3, 44]. But they do not avoid the interface question. They cross a continuous-to-discrete boundary at every denoising step through logits, softmax probabilities, and sampling or argmax decisions. Our axes have discrete analogues: denoisability becomes mask-recovery accuracy; recoverability becomes whether intermediate distributions preserve semantic and syntactic constraints; decoder compatibility becomes whether intermediate logits remain inside stable token basins; trajectory reliability becomes whether confidence, entropy, or agreement predicts final correctness before the last step. Testing these analogues is outside this paper, but the broader point is the same: generation quality is an interface property, and any model that crosses a continuous-to-discrete boundary must solve the same margin and compatibility questions that we diagnose here.

CCDD [69] frames continuous diffusion as expressive but practically difficult to train and decode. Our experiments give a complementary mechanism for this gap. A continuous state space may be expressive, but if its off-manifold states are not recoverable, if order information is compressed away, or if the decoder basin is narrow, the expressive latent can still fail at the token interface. This explains why hybrid continuous-discrete systems are plausible: the continuous component can carry semantic organization, while the discrete component can anchor token realization and verification.

Several questions remain open. First, the diagnostic should be scaled: can readiness scores predict training efficiency for larger jointly trained systems? Second, decoder basins need to be engineered rather than merely measured: how can training widen the basin without inducing low-entropy collapse? Third, future systems should test whether the representation and decoder can co-evolve a readable basin instead of inheriting one from a frozen encoder. Fourth, the probes here should be converted into practical systems only after cheaper monitors, token-wise policies, or dynamic batching remove their diagnostic overhead. Fifth, cross-architecture validation should move beyond boundary checks to independently trained continuous, latent, and hybrid DLMS. Finally, the local margin analysis should be extended into a theory of nonlinear, anisotropic decoder basins. Directional RBN already shows that the most fragile principal direction is checkpoint-dependent—ELF-M is most fragile along its first principal component, whereas ELF-L is more fragile along its second. The ELF-M follow-up audit points to punctuation and token-boundary anisotropy rather than a named semantic axis, but a full explanation requires local decoder-Jacobian or logit-level sensitivity analysis rather than token-neighbor inspection alone. Our online delta-gating controls, decoder-noise ablations, and margin-loss negative result define useful starting points, but they also argue for the same discipline as the rest of the paper: establish the diagnostic evidence before optimizing the method.

Higher-level extensions. Several extensions fall outside the present claim. An information-theoretic *interface capacity* could measure how much token information a decoder preserves under a constrained perturbation distribution, turning noise-sweep retention curves into a global analogue of the local margin bound. A pretraining-readiness score could combine denoisability, order sensitivity, clean margin depth, and lightweight readout agreement before training a DLM. An interface compiler could use the measured phase diagram to generate sparse margin monitors, confidence routers, SC-update candidate selectors, or SDE-gamma schedules automatically. ZSBD confidence routing, the lightweight margin proxy, and equal-budget SC rejection provide initial evidence for this direction, while Token-wise Early Commitment (TEC) and one-step projection show that local compilation rules can fail. A cross-architecture basin taxonomy could compare ELF, LDLM, RePlaid, DiHAL-style hidden-state replacement, TEncDM, LangFlow, and

discrete DLMs under normalized readiness axes. These directions require additional checkpoints, adapters, human or task evaluation, and training runs. We treat them as implications of the diagnostic protocol rather than completed contributions; each requires validation against the same readiness axes.

A practical checklist for future DLMs. The results suggest a reporting checklist, summarized in Table 6: This

Table 6: A minimal diagnostic checklist for future continuous or latent DLM papers. The checklist translates the paper’s failure modes into reporting requirements before claiming a new state space, decoder, sampler, internal signal, or training recipe.

Before claiming ...	Report ...
a new state space is diffusion-ready	linear denoising NMSE, semantic recovery, order sensitivity, native-decoder margin under corruption, and at least one trajectory reliability signal.
a decoder is a harmless readout	native-decoder agreement, margin recovery under latent corruption, and entropy calibration.
a sampler is better	PPL together with entropy, repetition/distinctness, MAUVE or another distributional metric.
an internal signal is useful	shuffled-signal, delayed-signal, and time-region controls.
a latent autoencoder is enough	clean reconstruction and decoder-basin robustness under the prior’s noise range.

checklist is modest, but it would have caught most of the misleading shortcuts exposed in our experiments.

7 Limitations

The study uses existing checkpoints and diagnostic interventions rather than training a new DLM. This choice limits claims about ultimate generation quality. ELF-M and ELF-L are used for trend confirmation rather than a scaling law, because local PyTorch checkpoints and sampling settings may differ from Tensor Processing Unit (TPU)-scale evaluation. The shard-level SEM bars use four independent sampling shards under fixed public checkpoints; they are appropriate for robustness visualization but not for formal training-seed hypothesis tests. Raw cross-decoder probing between ELF and Cola is not a meaningful native test because their latent dimensions, tokenizers, scaling conventions, and decoder targets differ; learning a bridge would test adapter capacity rather than native decoder compatibility. The new cross-decoder transfer results are also restricted to ELF-B/M/L decoders that share the same T5-small interface and public checkpoint family; they do not support a universal claim about T5 geometry or independent training seeds. Finally, MAUVE is computed with 2048 samples and a GPT-2 featurizer for practicality, so we use it as a complementary signal rather than a definitive quality metric.

There are also methodological limitations. Linear probes can underestimate nonlinear linguistic information, although this bias is acceptable here because the goal is to test minimal recoverability. GPT-2-Large PPL is an imperfect proxy for human judgments and can reward low-entropy text. Our entropy-matched decoder and GPT-2-small temperature sweeps address this issue directly, but they do not replace human evaluation, task-specific evaluation, or downstream reasoning benchmarks. The basin definition is operational rather than a full global theory: it is a decoder-margin super-level set measured along generated trajectories, not a claim that the high-dimensional set is convex, spherical, or architecture-independent. Directional RBN shows that the basin is strongly anisotropic, so future theory should use local directional sensitivities or anisotropic norms rather than only isotropic Gaussian bounds. The paired basin intervention is a fixed-checkpoint test at one model size and one main intervention phase; it validates the sign of the control variable but does not replace a trained guidance objective.

Token-wise entry, ZSBD geometry ablation, and residual-tail targeting explain where the current probes work, and the 512-sample sequence-level audit identifies numeric, rare, ZSBD-wrong, and late-margin tokens as stress cases. They still do not constitute a full out-of-distribution (OOD) suite over code, long contexts, numeric exact match, prompt shift, or domain shift; the residual-tail pattern could change on domains such as Yelp Polarity reviews, AG News, or code. Long-form coherence is also outside the current certificate: decoder margins and readout agreement measure local interface readability, and our topic audit shows that local sentence coherence, low PPL, and high decoder margin can coexist with first-to-last topic drift. MDP is also a generated-manifold interface probe: its token-position training examples are drawn from generated sequences and are therefore correlated within samples, so the linear

readout should not be interpreted as an independent and identically distributed (IID) token classifier or a universal decoder. The external checks are too few and too heterogeneous to support a rank correlation between basin width and PPL across architectures. The GPT-2-small comparison is an unconditional sampling comparison rather than a full AR benchmark suite. The Cola-DLM analysis focuses on VAE and trajectory boundary behavior rather than full benchmark reproduction. Finally, our front-loaded schedule and BGEE provide evidence that trajectory signals are usable, but they are not competitive decoding algorithms. BGEE in particular reports NFE savings under an expensive diagnostic monitor; the direct monitored implementation is slower in wall-clock time than unmonitored sampling. We will release the phase-labeled diagnostic scripts, table outputs, and plotting code with the public manuscript; until then, reproducibility relies on the released ELF/Cola/LangFlow/Bitstream checkpoints and the implementation details documented in the appendix.

The additional sampler-extension checks are also bounded. The SC-update rejection experiment uses an equal $K = 3$ candidate budget, but it is a candidate selector rather than an optimized wall-clock sampler; its PPL gains trade off against entropy, distinctness, and repetition. The lightweight margin proxy is a cheap pre-filter for native-margin monitoring, not a formal certificate. Token-wise Early Commitment and one-step projection are negative controls under the tested implementations, not impossibility results for all token-wise freezing or few-step projection methods. They show that the interface phase diagram cannot be compiled into a sampler by local thresholding alone.

8 Conclusion

Our evidence suggests that continuous language diffusion depends on whether a continuous state can be denoised, linguistically recovered, and decoded through a compatible interface. ELF succeeds because the representation, denoising trajectory, and decoder form an interface with measurable reliability signals; those signals are strongest for local token decisions and do not by themselves certify long-form discourse coherence. A denoising Transformer or a smooth embedding space alone is insufficient. This does not settle the larger self-bootstrapping problem for continuous language representations. It specifies what such a representation must provide: a decoder-readable basin that the denoising dynamics can enter and the token interface can calibrate. Cola-DLM shows the complementary boundary: clean reconstruction can be strong while decoder-basin robustness remains narrow. The practical message is to test the interface before training a larger continuous DLM. A small diagnostic suite, applied before committing to large-scale training, can reveal whether the proposed state space is genuinely ready for diffusion or easy under a misleading scalar metric that hides a latent interface failure.

Acknowledgments

This work was supported in part by the Development and Reform Commission of Shenzhen Municipality (grant no. F-2024-Z99503929), the Shenzhen Medical Research Fund (grant no. C2401007), and the State Key Laboratory of Chemical Oncogenomics, Institute of Biomedical Health Technology and Engineering, Shenzhen Bay Laboratory. We thank the ELF authors for releasing the checkpoints and code studied here, and refer readers to the ELF release for the compute resources used to train those checkpoints. We thank the Cola-DLM team at ByteDance, the LangFlow team at UIUC, and the BitstreamDiffusion authors for releasing their models and code under open-source licenses. We also thank the creators of OpenWebText, Yelp Polarity, AG News, and the T5, BERT, RoBERTa, and GPT-2 pretrained models for making their datasets and checkpoints publicly available. Our diagnostic experiments ran on consumer GPU workstations with no additional large-scale training.

References

- [1] Hasan Amin, Yuan Gao, Yaser Souri, Subhojit Som, Ming Yin, Rajiv Khanna, and Xia Song. Consistent diffusion language models. *arXiv preprint arXiv:2605.00161*, 2026. doi: 10.48550/arXiv.2605.00161. URL <https://arxiv.org/abs/2605.00161>.
- [2] Marianne Arriola, Aaron Gokaslan, Justin T. Chiu, Zhihan Yang, Zhixuan Qi, Jiaqi Han, Subham Sekhar Sahoo, and Volodymyr Kuleshov. Block diffusion: Interpolating between autoregressive and diffusion language models.

- arXiv preprint arXiv:2503.09573*, 2025. doi: 10.48550/arXiv.2503.09573. URL <https://arxiv.org/abs/2503.09573>.
- [3] Jacob Austin, Daniel D. Johnson, Jonathan Ho, Daniel Tarlow, and Rianne van den Berg. Structured denoising diffusion models in discrete state-spaces. In *Advances in Neural Information Processing Systems*, volume 34, pages 17981–17993, 2021. doi: 10.48550/arXiv.2107.03006. URL <https://proceedings.neurips.cc/paper/2021/hash/958c530554f78bcd8e97125b70e6973d-Abstract.html>.
- [4] Georgios Batzolis, Mark Girolami, and Luca Ambrogioni. Towards closing the autoregressive gap in language modeling via entropy-gated continuous bitstream diffusion. *arXiv preprint arXiv:2605.07013*, 2026. doi: 10.48550/arXiv.2605.07013. URL <https://arxiv.org/abs/2605.07013>.
- [5] Lukas Lao Beyer, Tianhong Li, Xinlei Chen, Sertac Karaman, and Kaiming He. Highly compressed tokenizer can generate without training. In *Proceedings of the 42nd International Conference on Machine Learning*, volume 267 of *Proceedings of Machine Learning Research*, pages 4096–4114. PMLR, 2025. doi: 10.48550/arXiv.2506.08257. URL <https://arxiv.org/abs/2506.08257>.
- [6] James Bradbury, Roy Frostig, Peter Hawkins, Matthew James Johnson, Chris Leary, Dougal Maclaurin, and Skye Wanderman-Milne. JAX: Composable transformations of python+numpy programs, 2018. URL <https://github.com/google/jax>.
- [7] Ciprian Chelba, Tomas Mikolov, Mike Schuster, Qi Ge, Thorsten Brants, Phillipp Koehn, and Tony Robinson. One billion word benchmark for measuring progress in statistical language modeling. In *Interspeech*, pages 2635–2639, 2014. doi: 10.21437/INTERSPEECH.2014-564. URL https://www.isca-archive.org/interspeech_2014/chelba14_interspeech.html.
- [8] Yuxin Chen, Chumeng Liang, Hangke Sui, Ruihan Guo, Chaoran Cheng, Jiaxuan You, and Ge Liu. Langflow: Continuous diffusion rivals discrete in language modeling. *arXiv preprint arXiv:2604.11748*, 2026. doi: 10.48550/arXiv.2604.11748. URL <https://arxiv.org/abs/2604.11748>.
- [9] Zigeng Chen, Gongfan Fang, Xinyin Ma, Ruonan Yu, and Xinchao Wang. DMax: Aggressive parallel decoding for dLLMs. *arXiv preprint arXiv:2604.08302*, 2026. doi: 10.48550/arXiv.2604.08302. URL <https://arxiv.org/abs/2604.08302>.
- [10] Oscar Davis, Anastasiia Filippova, Pierre Ablin, Victor Turrisi, Amitis Shidani, Marco Cuturi, and Louis Béthune. Scaling categorical flow maps. *arXiv preprint arXiv:2605.07820*, 2026. doi: 10.48550/arXiv.2605.07820. URL <https://arxiv.org/abs/2605.07820>.
- [11] Mingyang Deng, He Li, Tianhong Li, Yilun Du, and Kaiming He. Generative modeling via drifting. *arXiv preprint arXiv:2602.04770*, 2026. doi: 10.48550/arXiv.2602.04770. URL <https://arxiv.org/abs/2602.04770>.
- [12] Jacob Devlin, Ming-Wei Chang, Kenton Lee, and Kristina Toutanova. BERT: Pre-training of deep bidirectional transformers for language understanding. In *Proceedings of the 2019 Conference of the North American Chapter of the Association for Computational Linguistics: Human Language Technologies*, pages 4171–4186, 2019. doi: 10.18653/v1/N19-1423. URL <https://aclanthology.org/N19-1423/>.
- [13] Kawin Ethayarajh. How contextual are contextualized word representations? comparing the geometry of BERT, ELMo, and GPT-2 embeddings. In *Proceedings of the 2019 Conference on Empirical Methods in Natural Language Processing and the 9th International Joint Conference on Natural Language Processing*, pages 55–65, 2019. doi: 10.18653/v1/D19-1006. URL <https://aclanthology.org/D19-1006/>.
- [14] Yonggan Fu, Lexington Whalen, Abhinav Garg, Chengyue Wu, Maksim Khadkevich, Nicolai Oswald, Enze Xie, Daniel Egert, Sharath Turuvekere Sreenivas, Shizhe Diao, Chenhan Yu, Ye Yu, Weijia Chen, Sajad Norouzi, Jingyu Liu, Shiyi Lan, Ligeng Zhu, Jin Wang, Jindong Jiang, Morteza Mardani, Mehran Maghoubi, Song Han, Ante Jukic, Nima Tajbakhsh, Jan Kautz, and Pavlo Molchanov. Nemotron-labs-diffusion: A tri-mode language model unifying autoregressive, diffusion, and self-speculation decoding. Technical report, NVIDIA, 2026. URL https://research.nvidia.com/publication/2026-05_nemotron-labs-diffusion-tri-mode-language-model-unifying-autoregressive. Technical report.

- [15] Aaron Gokaslan and Vanya Cohen. Openwebtext corpus, 2019. URL <https://skylion007.github.io/OpenWebTextCorpus/>.
- [16] Shansan Gong, Mukai Li, Jiangtao Feng, Zhiyong Wu, and Lingpeng Kong. Diffuseq: Sequence to sequence text generation with diffusion models. In *International Conference on Learning Representations*, 2023. doi: 10.48550/arXiv.2210.08933. URL <https://arxiv.org/abs/2210.08933>. ICLR 2023 camera ready.
- [17] Hongcan Guo, Qinyu Zhao, Yian Zhao, Shen Nie, Rui Zhu, Qiushan Guo, Feng Wang, Tao Yang, Hengshuang Zhao, Guoqiang Wei, and Yan Zeng. Continuous latent diffusion language model. *arXiv preprint arXiv:2605.06548*, 2026. doi: 10.48550/arXiv.2605.06548. URL <https://arxiv.org/abs/2605.06548>.
- [18] Xiaochuang Han, Sachin Kumar, and Yulia Tsvetkov. SSD-LM: Semi-autoregressive simplex-based diffusion language model for text generation and modular control. In *Proceedings of the 61st Annual Meeting of the Association for Computational Linguistics (Volume 1: Long Papers)*, pages 11575–11596, 2023. doi: 10.18653/v1/2023.acl-long.647. URL <https://aclanthology.org/2023.acl-long.647/>.
- [19] Michael Hersche, Nicolas Menet, Ronan Tanios, and Abbas Rahimi. Locally coherent parallel decoding in diffusion language models. *arXiv preprint arXiv:2603.20216*, 2026. doi: 10.48550/arXiv.2603.20216. URL <https://arxiv.org/abs/2603.20216>.
- [20] Jonathan Ho and Tim Salimans. Classifier-free diffusion guidance. *arXiv preprint arXiv:2207.12598*, 2022. doi: 10.48550/arXiv.2207.12598. URL <https://arxiv.org/abs/2207.12598>.
- [21] Jonathan Ho, Ajay Jain, and Pieter Abbeel. Denoising diffusion probabilistic models. In *Advances in Neural Information Processing Systems*, volume 33, pages 6840–6851, 2020. doi: 10.48550/arXiv.2006.11239. URL <https://proceedings.neurips.cc/paper/2020/hash/4c5bcfec8584af0d967f1ab10179ca4b-Abstract.html>.
- [22] Keya Hu, Linlu Qiu, Yiyang Lu, Hanhong Zhao, Tianhong Li, Yoon Kim, Jacob Andreas, and Kaiming He. Embedded language flows. *arXiv preprint arXiv:2605.10938*, 2026. doi: 10.48550/arXiv.2605.10938. URL <https://arxiv.org/abs/2605.10938>.
- [23] Jiaxiu Jiang, Jingjing Ren, Wenbo Li, Bo Wang, Haoze Sun, Yijun Yang, Jianhui Liu, Yanbing Zhang, Shenghe Zheng, Yuan Zhang, Haoyang Huang, Nan Duan, and Wangmeng Zuo. TextLDM: Language modeling with continuous latent diffusion. *arXiv preprint arXiv:2605.07748*, 2026. doi: 10.48550/arXiv.2605.07748. URL <https://arxiv.org/abs/2605.07748>.
- [24] Diederik P. Kingma and Max Welling. Auto-encoding variational bayes. In *International Conference on Learning Representations*, 2014. URL <https://openreview.net/forum?id=33X9fd2-9FyZd>.
- [25] Zahar Kohut, Severyn Shykula, Dmytro Khamula, Mykola Vysotskyi, Taras Rumezhak, and Volodymyr Karpiv. Just on time: Token-level early stopping for diffusion language models. *arXiv preprint arXiv:2602.11133*, 2026. doi: 10.48550/arXiv.2602.11133. URL <https://arxiv.org/abs/2602.11133>.
- [26] Injin Kong, Hyounghoon Lee, and Yohan Jo. Where should diffusion enter a language model? geometry-guided hidden-state replacement. *arXiv preprint arXiv:2605.14368*, 2026. doi: 10.48550/arXiv.2605.14368. URL <https://arxiv.org/abs/2605.14368>.
- [27] Daniel J. Korchinski, Alessandro Favero, and Matthieu Wyart. Learn from your own latents and not from tokens: A sample-complexity theory. *arXiv preprint arXiv:2605.27734*, 2026. doi: 10.48550/arXiv.2605.27734. URL <https://arxiv.org/abs/2605.27734>.
- [28] Simon Kornblith, Mohammad Norouzi, Honglak Lee, and Geoffrey Hinton. Similarity of neural network representations revisited. In *Proceedings of the 36th International Conference on Machine Learning*, volume 97 of *Proceedings of Machine Learning Research*, pages 3519–3529. PMLR, 2019. doi: 10.48550/arXiv.1905.00414. URL <https://proceedings.mlr.press/v97/kornblith19a/kornblith19a.pdf>.

- [29] Chanhyuk Lee, Jaehoon Yoo, Manan Agarwal, Sheel Shah, Jerry Huang, Aditi Raghunathan, Seunghoon Hong, Nicholas M. Boffi, and Jinwoo Kim. Flow map language models: One-step language modeling via continuous denoising. *arXiv preprint arXiv:2602.16813*, 2026. doi: 10.48550/arXiv.2602.16813. URL <https://arxiv.org/abs/2602.16813>.
- [30] Jean-Marie Lemerrier, Tomas Geffner, Karsten Kreis, Morteza Mardani, Arash Vahdat, and Ante Jukić. DiLaDiff: Distilled latent-augmented diffusion for language modeling. *arXiv preprint arXiv:2605.23605*, 2026. doi: 10.48550/arXiv.2605.23605. URL <https://arxiv.org/abs/2605.23605>.
- [31] Jiwei Li, Michel Galley, Chris Brockett, Jianfeng Gao, and Bill Dolan. A diversity-promoting objective function for neural conversation models. In *Proceedings of the 2016 Conference of the North American Chapter of the Association for Computational Linguistics: Human Language Technologies*, pages 110–119, 2016. doi: 10.18653/v1/N16-1014. URL <https://aclanthology.org/N16-1014/>.
- [32] Pengxiang Li, Yefan Zhou, Dilxat Muhtar, Lu Yin, Shilin Yan, Li Shen, Soroush Vosoughi, and Shiwei Liu. Diffusion language models know the answer before decoding. *arXiv preprint arXiv:2508.19982*, 2025. doi: 10.48550/arXiv.2508.19982. URL <https://arxiv.org/abs/2508.19982>.
- [33] Xiang Lisa Li, John Thickstun, Ishaan Gulrajani, Percy Liang, and Tatsunori B. Hashimoto. Diffusion-lm improves controllable text generation. In *Advances in Neural Information Processing Systems*, 2022. doi: 10.48550/arXiv.2205.14217. URL https://papers.nips.cc/paper_files/paper/2022/hash/1be5bc25d50895ee656b8c2d9eb89d6a-Abstract-Conference.html.
- [34] J. Lin. Divergence measures based on the shannon entropy. *IEEE Transactions on Information Theory*, 37(1):145–151, 1991. doi: 10.1109/18.61115. URL <https://ieeexplore.ieee.org/abstract/document/61115>.
- [35] Yaron Lipman, Ricky T. Chen, Heli Ben-Hamu, Maximilian Nickel, and Matt Le. Flow matching for generative modeling. In *International Conference on Learning Representations*, 2023. doi: 10.48550/arXiv.2210.02747. URL <https://arxiv.org/abs/2210.02747v2>.
- [36] Yinhan Liu, Myle Ott, Naman Goyal, Jingfei Du, Mandar Joshi, Danqi Chen, Omer Levy, Mike Lewis, Luke Zettlemoyer, and Veselin Stoyanov. RoBERTa: A robustly optimized BERT pretraining approach. *arXiv preprint arXiv:1907.11692*, 2019. doi: 10.48550/arXiv.1907.11692. URL <https://arxiv.org/abs/1907.11692>.
- [37] Justin Lovelace, Varsha Kishore, Chao Wan, Eliot Shekhtman, and Kilian Q. Weinberger. Latent diffusion for language generation. In *Advances in Neural Information Processing Systems*, 2023. doi: 10.48550/arXiv.2212.09462. URL https://proceedings.neurips.cc/paper_files/paper/2023/hash/b2a2bd5d5051ff6af52e1ef60aefd255-Abstract-Conference.html.
- [38] Harry Lu. Measuring temporal linguistic emergence in diffusion language models. *arXiv preprint arXiv:2604.23235*, 2026. doi: 10.48550/arXiv.2604.23235. URL <https://arxiv.org/abs/2604.23235>.
- [39] Lizhuo Luo, Zhuoran Shi, Jiajun Luo, Zhi Wang, Shen Ren, Wenya Wang, and Tianwei Zhang. DAWN: Dependency-aware fast inference for diffusion LLMs. *arXiv preprint arXiv:2602.06953*, 2026. doi: 10.48550/arXiv.2602.06953. URL <https://arxiv.org/abs/2602.06953>.
- [40] Viacheslav Meshchaninov, Alexander Shabalin, Egor Chibulatov, Nikita Gushchin, Ilya Koziev, Alexander Korotin, and Dmitry Vetrov. How to train your latent diffusion language model jointly with the latent space. *arXiv preprint arXiv:2605.07933*, 2026. doi: 10.48550/arXiv.2605.07933. URL <https://arxiv.org/abs/2605.07933>.
- [41] Amr Mohamed, Yang Zhang, Michalis Vazirgiannis, and Guokan Shang. Fast-decoding diffusion language models via progress-aware confidence schedules. *arXiv preprint arXiv:2512.02892*, 2025. doi: 10.48550/arXiv.2512.02892. URL <https://arxiv.org/abs/2512.02892>.
- [42] Nasrin Mostafazadeh, Nathanael Chambers, Xiaodong He, Devi Parikh, Dhruv Batra, Lucy Vanderwende, Pushmeet Kohli, and James Allen. A corpus and cloze evaluation for deeper understanding of commonsense stories. In *Proceedings of the 2016 Conference of the North American Chapter of the Association for Computational Linguistics: Human Language Technologies*, pages 839–849, 2016. doi: 10.18653/v1/N16-1098. URL <https://aclanthology.org/N16-1098/>.

- [43] Shen Nie, Fengqi Zhu, Chao Du, Tianyu Pang, Qian Liu, Guangtao Zeng, Min Lin, and Chongxuan Li. Scaling up masked diffusion models on text. *arXiv preprint arXiv:2410.18514*, 2024. doi: 10.48550/arXiv.2410.18514. URL <https://arxiv.org/abs/2410.18514>.
- [44] Shen Nie, Fengqi Zhu, Zebin You, Xiaolu Zhang, Jingyang Ou, Jun Hu, Jun Zhou, Yankai Lin, Ji-Rong Wen, and Chongxuan Li. Large language diffusion models. *arXiv preprint arXiv:2502.09992*, 2025. doi: 10.48550/arXiv.2502.09992. URL <https://arxiv.org/abs/2502.09992>.
- [45] Adam Paszke, Sam Gross, Francisco Massa, Adam Lerer, James Bradbury, Gregory Chanan, Trevor Killeen, Zeming Lin, Natalia Gimelshein, Luca Antiga, Alban Desmaison, Andreas Kopf, Edward Yang, Zachary DeVito, Martin Raison, Alykhan Tejani, Sasank Chilamkurthy, Benoit Steiner, Lu Fang, Junjie Bai, and Soumith Chintala. PyTorch: An imperative style, high-performance deep learning library. In *Advances in Neural Information Processing Systems*, volume 32, 2019. URL https://papers.nips.cc/paper_files/paper/2019/hash/bdbca288fee7f92f2bfa9f7012727740-Abstract.html.
- [46] Arjun Patrawala, Jiahai Feng, Erik Jones, and Jacob Steinhardt. Llm layers immediately correct each other. In *The Thirty-ninth Annual Conference on Neural Information Processing Systems*, 2025. URL <https://neurips.cc/virtual/2025/poster/119727>.
- [47] William Peebles and Saining Xie. Scalable diffusion models with transformers. In *Proceedings of the IEEE/CVF International Conference on Computer Vision*, pages 4195–4205, 2023. doi: 10.48550/arXiv.2212.09748. URL https://openaccess.thecvf.com/content/ICCV2023/papers/Peebles_Scalable_Diffusion_Models_with_Transformers_ICCV_2023_paper.pdf.
- [48] Fred Zhangzhi Peng, Alexis Fox, Anru R. Zhang, and Alexander Tong. Don’t retrain, align: Adapting autoregressive lms to diffusion lms via representation alignment. *arXiv preprint arXiv:2605.06885*, 2026. doi: 10.48550/arXiv.2605.06885. URL <https://arxiv.org/abs/2605.06885>.
- [49] Krishna Pillutla, Lang Liu, John Thickstun, Sean Welleck, Swabha Swayamdipta, Rowan Zellers, Sewoong Oh, Yejin Choi, and Zaid Harchaoui. Mauve scores for generative models: Theory and practice. *Journal of Machine Learning Research*, 24(356):1–92, 2023. URL <https://jmlr.org/papers/v24/23-0023.html>.
- [50] Alec Radford, Jeffrey Wu, Rewon Child, David Luan, Dario Amodei, and Ilya Sutskever. Language models are unsupervised multitask learners. Technical report, OpenAI, 2019. URL https://cdn.openai.com/better-language-models/language_models_are_unsupervised_multitask_learners.pdf.
- [51] Colin Raffel, Noam Shazeer, Adam Roberts, Katherine Lee, Sharan Narang, Michael Matena, Yanqi Zhou, Wei Li, and Peter J. Liu. Exploring the limits of transfer learning with a unified text-to-text transformer. *Journal of Machine Learning Research*, 21(140):1–67, 2020. URL <https://jmlr.org/papers/v21/20-074.html>.
- [52] Nils Reimers and Iryna Gurevych. Sentence-bert: Sentence embeddings using siamese bert-networks. In *Proceedings of the 2019 Conference on Empirical Methods in Natural Language Processing and the 9th International Joint Conference on Natural Language Processing*, pages 3982–3992, 2019. doi: 10.18653/v1/D19-1410. URL <https://aclanthology.org/D19-1410/>.
- [53] Robin Rombach, Andreas Blattmann, Dominik Lorenz, Patrick Esser, and Björn Ommer. High-resolution image synthesis with latent diffusion models. In *Proceedings of the IEEE/CVF Conference on Computer Vision and Pattern Recognition*, pages 10684–10695, 2022. doi: 10.1109/CVPR52688.2022.01042. URL https://openaccess.thecvf.com/content/CVPR2022/papers/Rombach_High-Resolution_Image_Synthesis_With_Latent_Diffusion_Models_CVPR_2022_paper.pdf.
- [54] Daan Roos, Oscar Davis, Floor Eijkelboom, Michael Bronstein, Max Welling, İsmail İlkan Ceylan, Luca Ambrogioni, and Jan-Willem van de Meent. Categorical flow maps. *arXiv preprint arXiv:2602.12233*, 2026. doi: 10.48550/arXiv.2602.12233. URL <https://arxiv.org/abs/2602.12233>.
- [55] Subham Sekhar Sahoo, Marianne Arriola, Yair Schiff, Aaron Gokaslan, Edgar Marroquin, Justin T. Chiu, Alexander Rush, and Volodymyr Kuleshov. Simple and effective masked diffusion language models. In *Advances in Neural Information Processing Systems*, 2024. doi: 10.

- 48550/arXiv.2406.07524. URL https://proceedings.nips.cc/paper_files/paper/2024/hash/eb0b13cc515724ab8015bc978fdde0ad-Abstract-Conference.html.
- [56] Junzhe Shen, Jieru Zhao, Ziwei He, and Zhouhan Lin. CoDAR: Continuous diffusion language models are more powerful than you think. *arXiv preprint arXiv:2603.02547*, 2026. doi: 10.48550/arXiv.2603.02547. URL <https://arxiv.org/abs/2603.02547>.
- [57] Bian Sun, Kevin Zhai, Mubarak Shah, and Zhenyi Wang. Dystruct: Dynamically structured diffusion language model decoding via bayesian inference. *arXiv preprint arXiv:2605.09820*, 2026. doi: 10.48550/arXiv.2605.09820. URL <https://arxiv.org/abs/2605.09820>.
- [58] Qiao Sun, Zhicheng Jiang, Hanhong Zhao, and Kaiming He. Is noise conditioning necessary for denoising generative models? In *International Conference on Machine Learning*, 2025. URL <https://proceedings.mlr.press/v267/sun25g.html>.
- [59] Atula Tejaswi, Litu Rout, Constantine Caramanis, Sanjay Shakkottai, and Sujay Sanghavi. Entropy aware reward guidance for diffusion language model alignment. *arXiv preprint arXiv:2602.05000*, 2026. doi: 10.48550/arXiv.2602.05000. URL <https://arxiv.org/abs/2602.05000>.
- [60] Runqian Wang and Kaiming He. Diffuse and disperse: Image generation with representation regularization. *arXiv preprint arXiv:2506.09027*, 2025. doi: 10.48550/arXiv.2506.09027. URL <https://arxiv.org/abs/2506.09027>.
- [61] Jason Wei, Xuezhi Wang, Dale Schuurmans, Maarten Bosma, Brian Ichter, Fei Xia, Ed H. Chi, Quoc Le, and Denny Zhou. Chain-of-thought prompting elicits reasoning in large language models. In *Advances in Neural Information Processing Systems*, volume 35, pages 24824–24837, 2022. doi: 10.48550/arXiv.2201.11903. URL https://proceedings.neurips.cc/paper_files/paper/2022/hash/9d5609613524ecf4f15af0f7b31abca4-Abstract.html.
- [62] Thomas Wolf, Lysandre Debut, Victor Sanh, Julien Chaumond, Clement Delangue, Anthony Moi, Pierric Cistac, Tim Rault, Remi Louf, Morgan Funtowicz, Joe Davison, Sam Shleifer, Patrick von Platen, Clara Ma, Yacine Jernite, Julien Plu, Canwen Xu, Teven Le Scao, Sylvain Gugger, Mariama Drame, Quentin Lhoest, and Alexander M. Rush. Transformers: State-of-the-art natural language processing. In *Proceedings of the 2020 Conference on Empirical Methods in Natural Language Processing: System Demonstrations*, pages 38–45, 2020. doi: 10.18653/v1/2020.emnlp-demos.6. URL <https://aclanthology.org/2020.emnlp-demos.6/>.
- [63] Chengyue Wu, Hao Zhang, Shuchen Xue, Zhijian Liu, Shizhe Diao, Ligeng Zhu, Ping Luo, Song Han, and Enze Xie. Fast-dllm: Training-free acceleration of diffusion LLM by enabling KV cache and parallel decoding. *arXiv preprint arXiv:2505.22618*, 2025. doi: 10.48550/arXiv.2505.22618. URL <https://arxiv.org/abs/2505.22618>.
- [64] Zhihan Yang, Wei Guo, Shuibai Zhang, Subham Sekhar Sahoo, Yongxin Chen, Arash Vahdat, Morteza Mardani, and John Thickstun. Continuous diffusion scales competitively with discrete diffusion for language. *arXiv preprint arXiv:2605.18530*, 2026. doi: 10.48550/arXiv.2605.18530. URL <https://arxiv.org/abs/2605.18530>.
- [65] Sihyun Yu, Sangkyung Kwak, Huiwon Jang, Jongheon Jeong, Jonathan Huang, Jinwoo Shin, and Saining Xie. Representation alignment for generation: Training diffusion transformers is easier than you think. In *The Thirteenth International Conference on Learning Representations*, 2025. doi: 10.48550/arXiv.2410.06940. URL <https://arxiv.org/abs/2410.06940>.
- [66] De Shuai Zhang. When latent geometry is not enough: Draft-conditioned latent refinement for non-autoregressive text generation. *arXiv preprint arXiv:2605.15557*, 2026. doi: 10.48550/arXiv.2605.15557. URL <https://arxiv.org/abs/2605.15557>. Technical report v1.
- [67] Xiang Zhang, Junbo Zhao, and Yann LeCun. Character-level convolutional networks for text classification. In *Advances in Neural Information Processing Systems*, volume 28, 2015. URL <https://proceedings.neurips.cc/paper/2015/hash/250cf8b51c773f3f8dc8b4be867a9a02-Abstract.html>.

- [68] Kaiwen Zheng, Yongxin Chen, Hanzi Mao, Ming-Yu Liu, Jun Zhu, and Qinsheng Zhang. Masked diffusion models are secretly time-agnostic masked models and exploit inaccurate categorical sampling. In *International Conference on Learning Representations*, 2025. doi: 10.48550/arXiv.2409.02908. URL <https://arxiv.org/abs/2409.02908v6>.
- [69] Cai Zhou, Chenxiao Yang, Yi Hu, Chenyu Wang, Chubin Zhang, Muhan Zhang, Lester Mackey, Tommi Jaakkola, Stephen Bates, and Dinghuai Zhang. Coevolutionary continuous discrete diffusion: Make your diffusion language model a latent reasoner. *arXiv preprint arXiv:2510.03206*, 2025. doi: 10.48550/arXiv.2510.03206. URL <https://arxiv.org/abs/2510.03206>.
- [70] Zhanhui Zhou, Lingjie Chen, Hanghang Tong, and Dawn Song. dLLM: Simple diffusion language modeling. *arXiv preprint arXiv:2602.22661*, 2026. doi: 10.48550/arXiv.2602.22661. URL <https://arxiv.org/abs/2602.22661>.
- [71] Yichen Zhu, Xiaoming Shi, Peng Zhao, Weiyu Chen, Debing Zhang, and James Kwok. Dynamic chunking for diffusion language models. *arXiv preprint arXiv:2605.15676*, 2026. doi: 10.48550/arXiv.2605.15676. URL <https://arxiv.org/abs/2605.15676>.
- [72] Shun Zou, Yong Wang, Zehui Chen, Lin Chen, Chongyang Tao, Feng Zhao, and Xiangxiang Chu. Breaking block boundaries: Anchor-based history-stable decoding for diffusion large language models. *arXiv preprint arXiv:2604.08964*, 2026. doi: 10.48550/arXiv.2604.08964. URL <https://arxiv.org/abs/2604.08964>.

A Reproducibility Details

Code organization. The diagnostic suite is split into phases. Phase 0 verifies checkpoint loading and local generation. Phase 1 evaluates representation readiness and order sensitivity. Phase 2 audits ELF trajectories. Phase 3 runs self-conditioning schedule sweeps. Later phases add Cola-DLM boundary tests, fair decoder calibration, MAUVE/reference-distribution metrics, ELF-L confirmation, and decoder margin analysis. This staged organization mirrors the scientific argument: later experiments are only meaningful if earlier diagnostic signals exist.

Terminology. We use *state space* for the continuous vectors being denoised, *native decoder* for the decoder trained with that state space, and *interface* for the pair. We reserve *diffusion-ready* for the full interface property, not merely for smooth latent geometry. This terminology matters because several negative controls are smooth but not linguistically meaningful, or decodable when clean but not robust under corruption.

Evidence hierarchy. We separate three evidence levels throughout the paper. *Core mechanism* claims are supported by representation controls, PCA controlled degradation, and fixed-checkpoint trajectory audits with shard-level robustness. *Minimal probes* such as BGEE, ZSBD, and MDP are used to test whether the mechanism exposes actionable variables; they are not presented as tuned production methods. *External architecture* checks on Cola-DLM, LangFlow, and BitstreamDiffusion are boundary diagnostics rather than full benchmark reproductions. The appendix keeps this hierarchy explicit, so that sample counts, shard counts, and checkpoint/training-seed assumptions are documented rather than inferred.

Tool disclosure. Language-model tools were used for proofreading, reference checks, and consistency checks. The authors reviewed all edits and are responsible for all claims, citations, experiments, and text.

Checkpoint loading. We use the official PyTorch [45] ELF code and public Hugging Face Transformers checkpoints [62]. The ELF-B, ELF-M, and ELF-L checkpoints are loaded with strict key matching against the official model definitions. The JAX [6] checkpoints are kept for reference, but all hidden-state and trajectory diagnostics in this manuscript use the PyTorch implementation because it exposes intermediate states more conveniently on local GPUs. We do not compare PyTorch and JAX numerics; the claims concern the released checkpoints and the representation–decoder interface, not framework-specific implementation differences.

Trajectory extraction. The official generation loop is scan-like and does not expose intermediate signals by default. Our audit wrapper runs the same SDE/ODE updates explicitly and records selected state summaries. We record per-sample final decoder entropy, self-conditioning delta, agreement with zero-self-conditioned predictions, and effective-rank proxies. To keep memory bounded, full hidden states and centered kernel alignment (CKA) [28] is computed only at selected time steps or on subsampled rows.

Basin-navigation audit. For the mechanism audit, we run ELF-B with 32-step SDE and SC=3 on 512 samples split evenly across four RTX 3090 GPUs. At every step we decode the predicted clean latent \hat{x}_t and record top1-top2 margins, decoder entropy, self-conditioning disagreement, and token-level delta-margin correlations. A second 64-sample audit stores selected-step logits to measure margins to the final decoded tokens and agreement with the final sequence. This two-pass design keeps the full mechanism audit cheap while still giving a direct final-basin crossing test.

Cross-scale and sampler audits. The same audit is repeated for ELF-B SDE64, ELF-M SDE64, ELF-L SDE64, and ELF-B ODE32 with 512 samples per run. The plots use normalized denoising phase rather than raw step index so that 32-step and 64-step trajectories can be compared directly. For external checks, LangFlow is audited with the same step-margin interface where available, and BitstreamDiffusion is evaluated through a sigma sweep over structured proxy codes and a repaired-tokenizer subset of 512 real OWT code sequences.

Basin-Guided Early Exit. BGEE uses the native decoder’s 10th-percentile predicted-clean margin as a stopping signal. We evaluate fixed exits and margin-threshold exits on the same 512 ELF-B SDE64 samples and on 256-sample ELF-M/L SDE64 confirmations. Quality is reported with geometric PPL, arithmetic mean PPL, sample entropy, distinct-2, repetition, and token agreement to the full 64-step decode. Main plots show simple interpretable margin levels. As protocol-rigor checks, we split generated samples in half, select a gate on the validation half subject to token agreement and geometric-PPL constraints, and report held-out test metrics. We also run a 512-sample random-time control that shuffles eligible denoising steps before applying the same margin or margin-plus-entropy rule; this separates temporal ordering from the threshold itself. The wall-clock timing smoke test uses four 32-sample GPU shards and three repeats per shard. It compares unmonitored 64-step sampling, full per-step margin monitoring, and conservative batch-level Margin-12 early exit; it is not an optimized dynamic-batching implementation.

Minimal Decoder Protocol. MDP uses generated ELF-B final latents rather than ground-truth T5 latents. For each sample, we store the final state z_T , the last predicted clean latent \hat{x}_T , the average of the last two clean predictions, and the native decoder’s argmax tokens. We then train a single token-wise linear readout on a train split and evaluate on held-out generated latents. The 1k experiment uses 1024 generated samples with a 768/256 train/eval split; the 4k experiment uses 4096 generated samples with a 3072/1024 split and caps training at 1.2M valid token positions; the 8k, 16k, and 32k saturation checks use 6144/2048, 12288/4096, and 24576/8192 splits, respectively. The 16k and 32k runs are loaded one readout at a time to avoid duplicating CPU memory; the 32k run caps training at 9.6M valid token positions and evaluates GPT-2-Large PPL on 4096 held-out texts. We report agreement to the native decoder, GPT-2-Large PPL, sample entropy, distinct-2, repetition, and margin. Small Gaussian noise augmentation is applied only to the readout input during training, not to the ELF denoiser or native decoder. Figure S1 gives the fuller 4k readout frontier behind the compact MDP panels in the main text.

The paired clean-manifold audit in Figure 35 reuses the 1024-sample generated MDP shards but does not train a readout or resample trajectories. For each native-decoded token sequence, we feed the same token ids to the frozen T5 encoder with the stored valid-token mask, normalize by ELF’s latent standard deviation, and decode this clean interface state with the same native ELF decoder used for z_T , \hat{x}_T , and the average of the last two clean predictions. The reported margins are target margins against the native argmax tokens from the generated sample, so the comparison isolates a same-token clean-vs-generated basin-depth gap rather than a text-distribution or tokenizer mismatch.

Zero-shot and reverse-basin tests. ZSBD reuses the same generated ELF-B final latents as MDP. We decode z_T , \hat{x}_T , and the average of the last two clean predictions by cosine nearest-neighbor lookup against the frozen T5 token-embedding table, with no learned readout parameters. The main figure uses 4096 samples; 8192- and 16384-sample checks are reported as stability controls. We evaluate GPT-2-Large PPL on 1024 decoded samples. RBN uses 1024 generated final latents. For each late-state variant, we add isotropic Gaussian noise with relative standard deviations $\{0, 0.005, 0.01, 0.02, 0.05, 0.1, 0.2, 0.5, 1.0\}$, decode with the native ELF decoder, and report token agreement to the clean native decode, 10th-percentile margin, decoder entropy, and PPL at selected noise levels. Both experiments are post-hoc analyses of generated states; no ELF weights are changed.

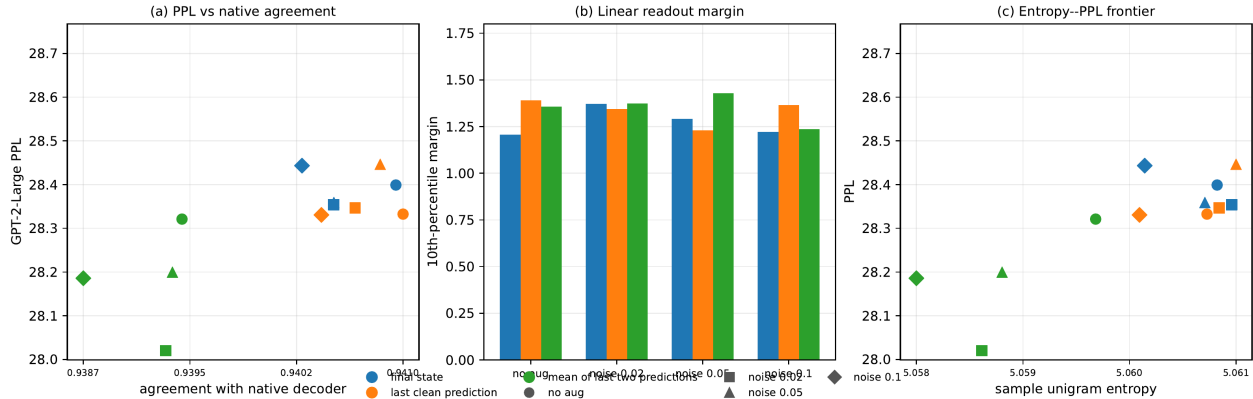


Figure S1: Full MDP readout frontier on 4096 generated latents. Left: GPT-2-Large PPL versus native-token agreement for different generated-latent readouts and noise augmentations. Middle: 10th-percentile native margin for the same readout family. Right: PPL versus generated-text unigram entropy. The best linear readouts approach the native decoder’s operating region while retaining a remaining PPL gap.

B Additional Basin Stress Tests

Cross-decoder basin transfer. We test whether generated final basins are private to one decoder or shared within the ELF checkpoint family. We generate 128 32-step SDE samples from each of ELF-B, ELF-M, and ELF-L, take the final latents from the source checkpoint, and decode them with ELF-B, ELF-M, and ELF-L decoders. Agreement is measured against the source checkpoint’s own native decoded tokens for the same source latents. This protocol avoids a ground-truth text comparison; it asks whether a different ELF decoder assigns the same token labels to states that the source denoiser has navigated into. B final latents decoded by M/L agree with B-native tokens at 0.9875/0.9870, M final latents decoded by B/L agree with M-native tokens at 0.9960/0.9957, and L final latents decoded by B/M agree with L-native tokens at 0.9952/0.9956. Figure S2 shows the resulting transfer matrix. The result indicates that ELF-family decoders share a large portion of the same final-token basin under the common T5-small interface. It does not address independent training seeds or arbitrary T5-space decoders.

Paired basin intervention. To test whether the basin signal is only correlational, we intervene on the predicted clean latent at step 16 of a 32-step ELF-B SDE trajectory and then continue denoising with the same initial noise and SDE noise stream. The projection intervention moves each position toward its nearest frozen T5 token embedding direction; the anti-basin intervention moves away from that direction; the random-matched control uses a random direction with matched norm. We expand the original pilot to 512 samples across four GPU shards. With $\alpha = 0.5$, projection increases the final margin tail by $\Delta p_{10} = +0.085 \pm 0.045$ and lowers GPT-2-Large PPL by 0.49 on a 256-text audit, while anti-basin perturbation decreases the margin tail by 0.186 ± 0.064 and raises PPL by 0.49. A random-matched perturbation is near neutral ($\Delta p_{10} = +0.009 \pm 0.024$, $\Delta PPL = -0.08$). Figure S3 visualizes the paired changes in margin, entropy, and edit size. A smaller $\alpha = 0.1$ 512-sample stability check preserves high token agreement but is too weak to cleanly separate projection from matched random noise. This is an interventional mechanism check, not a tuned guidance sampler: at $\alpha = 0.5$, token agreement to the unedited baseline is only about 0.72–0.78.

Token-wise basin entry. Sample-level early exit hides the fact that token positions enter the basin at different times. We therefore record all 32 predicted-clean states on 512 ELF-B samples and compute, for each valid final-token position, the first and persistent phase at which native-token match, ZSBD match, or a margin threshold is reached. Across 523,578 valid positions, persistent native-token entry reaches 99.96% with mean phase 0.533 and shard-mean p90 phase 0.794. Persistent ZSBD entry reaches 93.17%, and persistent entry with margin at least 8 reaches 94.69% with mean phase 0.580. Figure S4 shows the average entry timing, while Figure S5 shows why sequence-level hard tails remain. Together they explain both the value and the ceiling of BGEE: many easy positions are ready early, but a late hard tail remains, dominated by numeric tokens, rare subwords, and margin-borderline cases.

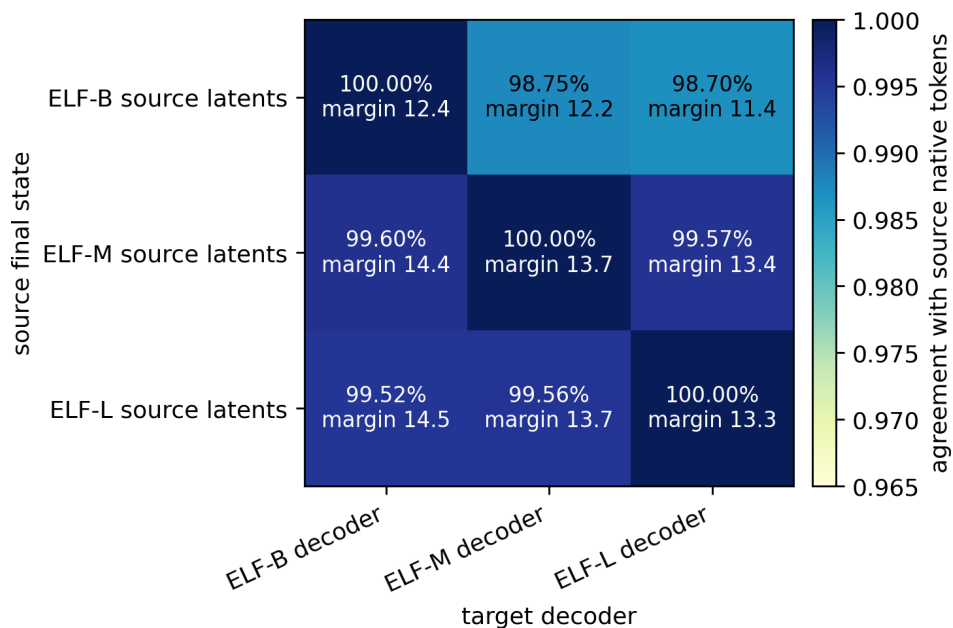


Figure S2: Cross-decoder basin transfer inside the ELF family. Rows indicate the source denoiser that generated the final latents; columns indicate the target decoder used for readout. Each cell reports agreement with the source model’s native decoded tokens and the corresponding source-label margin. High off-diagonal agreement indicates that generated final basins are largely shared across these checkpoint decoders under the same T5-small interface.

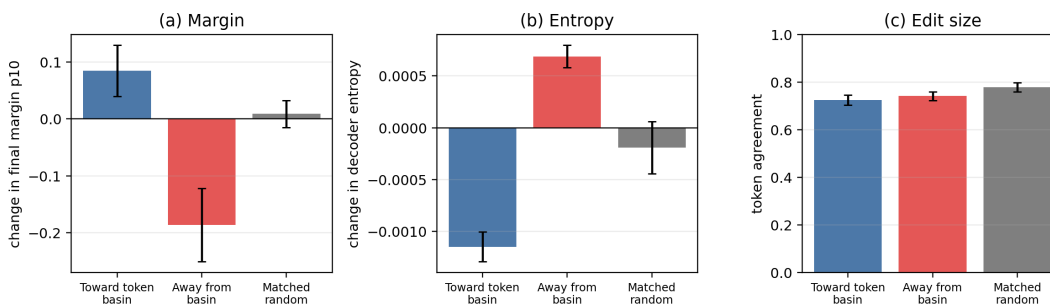


Figure S3: Paired basin intervention at 512 samples. Left: change in final 10th-percentile margin after a step-16 intervention. Middle: change in decoder entropy. Right: token agreement to the unedited baseline, which measures edit size. The same trajectory is continued after projecting toward token-embedding basins, pushing away from them, or applying a matched random perturbation; error bars are shard-level SEM.

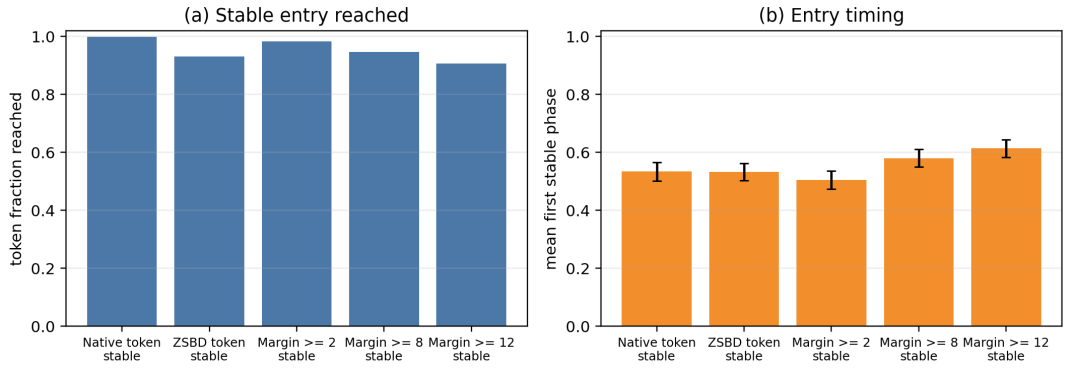


Figure S4: Token-wise basin entry on 512 ELF-B 32-step SDE trajectories. Left: fraction of valid token positions that ever satisfy each persistent-entry criterion. Right: mean first persistent phase for the same criteria, with shard-level SEM. Entry is staggered across positions: many positions stabilize before the final step, but margin-strict and ZSBD criteria retain a late hard tail.

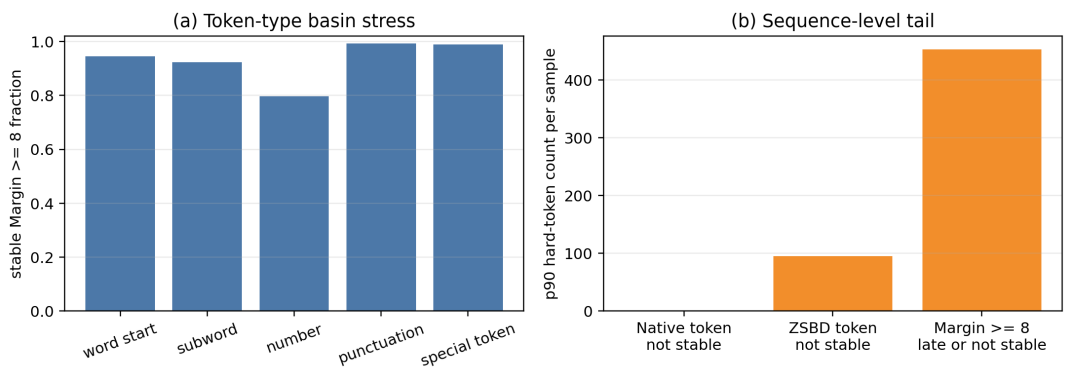


Figure S5: Token-wise basin stress at 512 samples. Left: persistent entry fraction with margin at least 8, grouped by token type. Right: p90 hard-token count per sample under native-token, ZSBD-token, and margin-at-least-8 criteria. Token-average agreement hides a sequence-level tail; numeric/subword-heavy samples keep many positions late or unstable.

ELF-M PC1 axis audit. Directional RBN exposes one especially sharp anomaly: a matched perturbation along ELF-M’s first principal component leaves only 1.5% native-token agreement, while isotropic, random, and sentiment directions all stay near 99.4%. To interpret this axis without turning it into a new method, we compare the same PC1 projection against token type, sample-level surface statistics, and the frozen T5 token-embedding projection. Figure S6 summarizes the result and gives the missing readout for this anomaly. The left panel establishes the specificity of the failure: the same perturbation budget is harmless in random and sentiment directions but catastrophic along PC1. The middle panel shows what dominates the axis: punctuation has much larger absolute projection than numbers, word starts, or ordinary subwords. The right panel explains why this is an interface effect rather than a semantic edit direction: generated-latent PC1 projection is strongly aligned with the T5 token table ($r = 0.82$ at the token-label level). At the sample level, the projection is also moderately associated with punctuation and quote density. Thus the ELF-M anomaly is best read as a decoder-sensitive token-boundary axis. Normal trajectories can remain on its valid generated manifold, but a global perturbation along that axis crosses many punctuation and boundary decisions at once. The conclusion is narrow but useful: anisotropy here is not just “some principal component is fragile,” but a concrete mismatch between high-variance generated-state directions and the decoder’s token-boundary geometry.

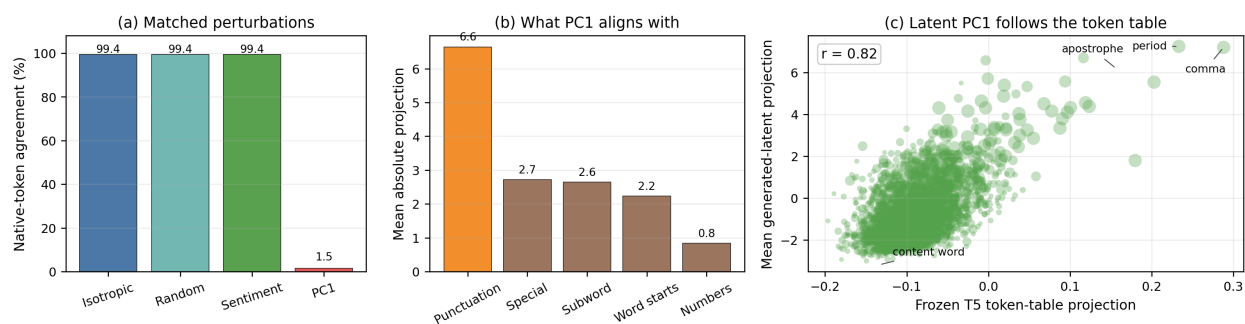


Figure S6: ELF-M PC1 axis audit. Left: matched perturbations at scale 1.0 show that isotropic, random, and sentiment directions remain inside the final basin, while the first principal component nearly destroys native-token agreement. Middle: the same PC1 projection is dominated by punctuation tokens rather than by numbers, word starts, or ordinary subwords. Right: mean generated-latent projection by token label is strongly aligned with the frozen T5 token-table projection ($r = 0.82$), with punctuation tokens at the high-projection edge. This identifies the fragile direction as a token-boundary anisotropy rather than a named semantic direction.

ZSBD geometry ablation. ZSBD uses cosine nearest neighbors in the frozen T5 token-embedding table. To test what part of this geometry matters, we rerun the lookup on 1024 ELF-B final latents with unnormalized dot-product lookup, Euclidean nearest-neighbor lookup, cosine lookup after whitening, small frequency-biased cosine variants, and a permuted-label embedding table. Figure S7 summarizes the ablation. Cosine reaches 93.41% agreement with the native decoder. Unnormalized dot-product lookup drops to 81.67%, Euclidean lookup to 3.44%, cosine after whitening to 4.29%, and permuted labels to near zero. A small frequency bias reaches about 94.03%, only slightly above pure cosine. The result identifies the useful structure as labeled angular token geometry, not vector norm, Euclidean proximity, or frequency alone. This also resolves an apparent tension with the order-sensitivity controls: bare token embeddings are order-blind, but ZSBD is applied to contextual final latents whose directions have already been shaped by the denoising trajectory. Cosine lookup reads out that contextual angular alignment; it does not make the token table itself an order-sensitive representation.

Residual-tail repair target analysis. We reuse the 32k MDP residuals and ask which cheap gates capture the remaining disagreement with the native decoder. The MDP error rate is 2.11%. A ZSBD-wrong gate covers only 6.63% of token positions but contains 73.4% of MDP errors. The rare-token quintile covers 20% of positions and contains 76.3% of errors, while a native low-margin quintile is an oracle-style diagnostic that contains 91.7% of errors. Numerics and subwords are smaller but sharper stress cases: numeric tokens cover only 0.65% of positions but have an 8.69% error rate, and subwords cover 13.0% with a 5.21% error rate. The tail-gated readout check in the main text uses the same 24576/4096 32k MDP split and evaluates GPT-2-Large PPL on the held-out 4096 texts. Its practical confidence gates use the learned linear readout’s top-1-vs-top-2 margin; the ZSBD-disagreement gate compares the linear readout to frozen T5 nearest-neighbor lookup; and the broad tail gate adds predicted rare, numeric, or subword positions. These gates are evaluated as diagnostics of tail predictability, not as a deployed partial-native decoder.

Sampler-extension boundary checks. The same diagnostics suggest several training-free or small-training sampler extensions, but the fixed-checkpoint results separate promising monitors from unsafe shortcuts. Pure ZSBD has its own

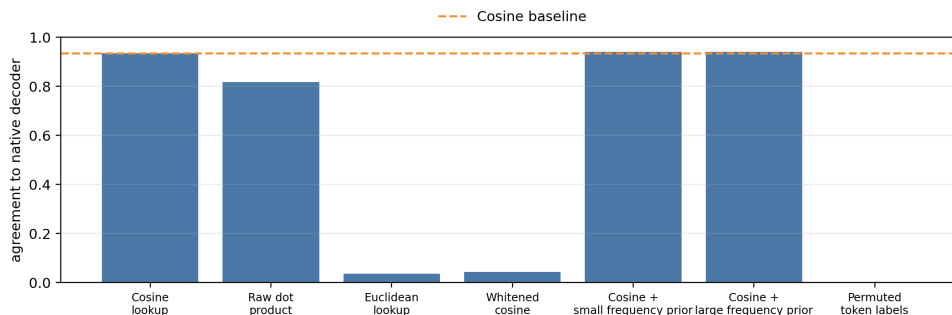


Figure S7: Geometry ablation for Zero-Shot Basin Decoding. Bars compare nearest-neighbor lookup rules on the same final ELF-B states; the dashed line marks the pure cosine baseline. Cosine lookup in the labeled T5 token-embedding table is strong, while Euclidean distance, whitening, or label permutation destroys agreement. Frequency gives a small calibration boost but does not explain the effect.

confidence signal: routing only the lowest 10% of ZSBD cosine-gap positions to the native decoder raises agreement from 93.37% to 96.77%, and routing the lowest 20% reaches 99.73%. A lightweight margin proxy is also promising. A 4.7k-parameter MLP using only online non-decoder features predicts the sequence 10th-percentile margin with test Spearman 0.985 and MAE 0.53; a conservative margin-8 proxy gate has 0.5% false-safe rate and 75.7% recall. These results support a cheap pre-filter followed by occasional native-margin verification. Equal-budget SC-update rejection gives a second training-free signal. We set the threshold on a held-out fixed-SC audit, using the normal sampler’s free update delta rather than the more expensive zero-vs-SC disagreement. With $K = 3$ candidates on 128 new samples, the random equal-budget baseline has PPL 23.45, threshold rejection reaches 22.08, and best-score selection reaches 20.96; however, entropy and distinctness fall and repetition rises, so this is a PPL-diversity frontier, not a solved sampler.

Two natural shortcuts fail and are therefore kept as negative controls. Token-wise Early Commitment freezes positions once their native margin exceeds a threshold. At 128 samples, margin-8 TEC commits 91.9% of tokens and estimates 45.4% token-step savings, but PPL worsens from 23.83 to 38.67, the 10th-percentile margin falls from 12.33 to 2.56, and agreement to the matched baseline falls to 28.9%; margin-12 is less aggressive but still poor. Token-wise basin entry is real, but local clean-latent freezing breaks later global consistency. One-step projection from noise also fails. A token-level ridge map from initial noise to final clean states, trained on held-out generated trajectories, agrees with the full ELF sampler on only 3.42% of tokens. The oracle token-embedding projection reaches 97.83% agreement, showing that the token embeddings can represent the final labels; what is missing is the nontrivial, path-dependent transport from noise into contextual basins.

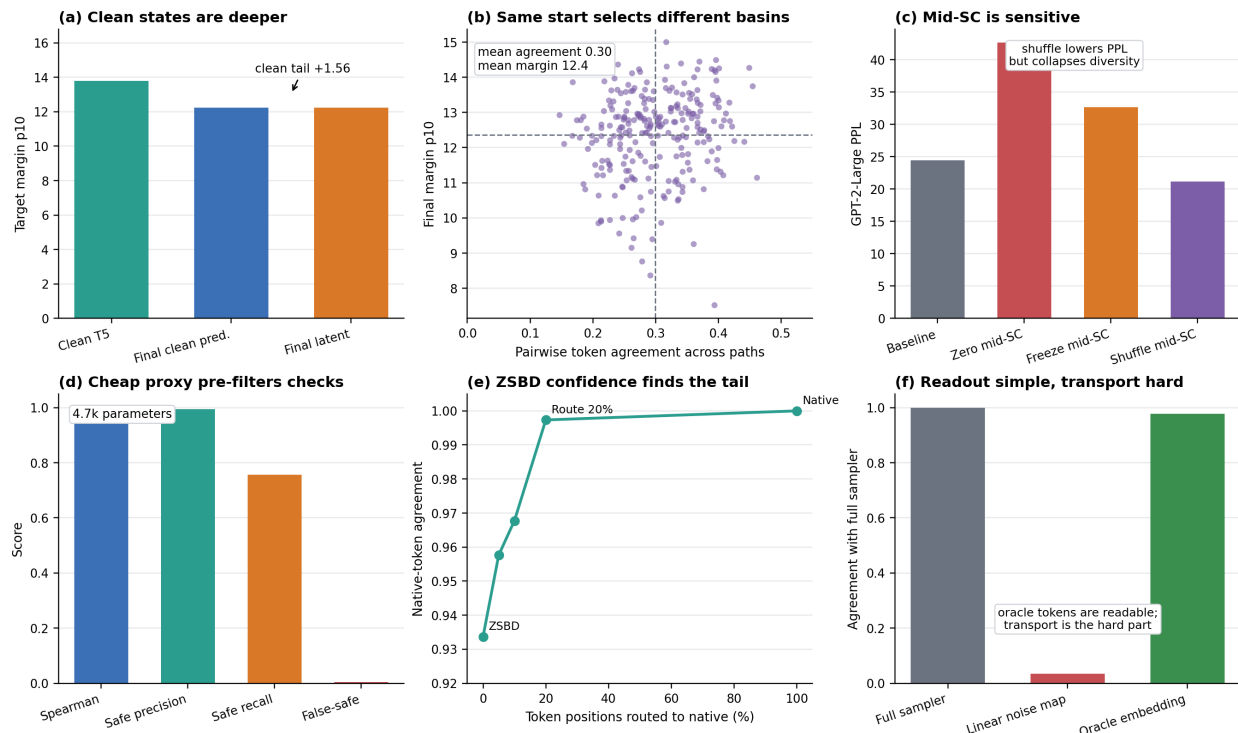


Figure S8: Additional insights mined from completed experiments. (a) Clean T5 interface states are deeper than generated final states in the lower margin tail, so ELF reaches a readable generated basin rather than exactly reproducing the clean manifold. (b) Same-start SDE paths end in high-margin basins but choose different token basins, showing path-selected rather than unique attraction. (c) Mid-trajectory self-conditioning interventions change PPL and margins; shuffling can lower PPL while collapsing diversity. (d) A small online proxy can pre-filter native-margin checks with high precision. (e) ZSBD cosine-gap confidence identifies much of the token tail without a learned readout. (f) One-step projection fails even though oracle token embeddings are readable, separating simple readout from nontrivial transport.

Final-basin latent editing. As a boundary test for latent editing, we estimate a sentiment direction from Yelp Polarity embeddings and add it to ELF final latents under a native-margin acceptance gate. This experiment tests whether the final decoder basin remains a linearly editable semantic canvas. It does not under conservative margins: target success changes only modestly because most tokens remain inside the native decision basin. We then run an adaptive line search along the same sentiment direction. This converts the failure into a sharper boundary test. Figure S9 shows that a safety margin of 2 changes only 4.1% of tokens and raises target success from 68.5% to 72.9% with little PPL change; forcing the margin down to zero raises target success to 99.7% but changes 38.4% of tokens and raises PPL to 51.0. Finally, we test two stronger final-state repairs on 128 samples across four GPU shards: a native decoder-gradient direction that directly increases positive sentiment-token logits, and a token-selective variant that applies the same direction only to the top sentiment-evidence positions. Figure S10 shows that the all-position decoder-gradient direction is more effective but still margin-limited; at safety margin 4 it changes 2.6% of tokens and raises target success to 76.6% with PPL 26.8, while at safety margin 2 it reaches 99.2% target success but raises PPL to 41.7. Token-selective variants remain absorbed by the basin, changing only about 0.6% of tokens and leaving target success unchanged. Figure S11 shows that a trajectory-level repair is more benign but still not a clean editor: step-16 decoder-gradient intervention raises target success from 64.1% to 69.5% with similar PPL (24.6 vs. 24.4), but requires changing 23.7% of tokens. BCD is therefore a boundary result rather than a probe contribution.

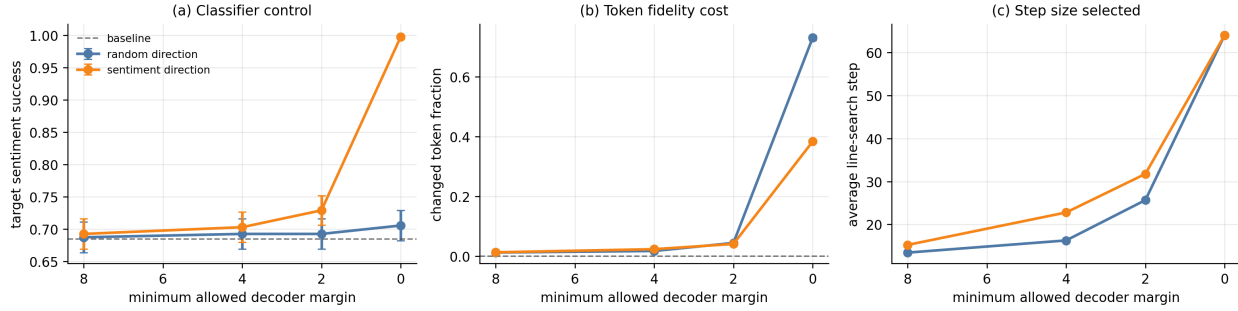


Figure S9: Final-basin BCD sentiment editing. Left: target sentiment success under adaptive line search. Middle: changed-token fraction relative to the unedited decode. Right: average line-search step selected by the margin constraint. Safe-margin edits are largely absorbed by the native decoder basin, whereas boundary-level edits can force target sentiment only by taking large steps that sacrifice token fidelity.

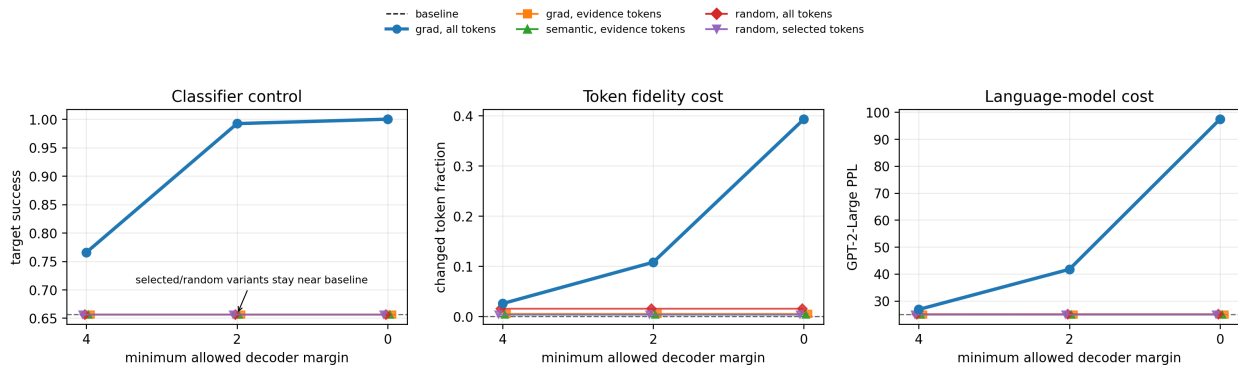


Figure S10: Decoder-gradient and token-selective BCD repairs. Left: target classifier success as the minimum allowed decoder margin is relaxed. Middle: changed-token fraction relative to the unedited decode. Right: GPT-2-Large PPL of the edited outputs. Decoder-gradient directions can control the target classifier, but the quality/fidelity cost rises sharply as the margin lower tail is relaxed. Perturbing only sentiment-evidence positions is almost completely absorbed by the final basin.

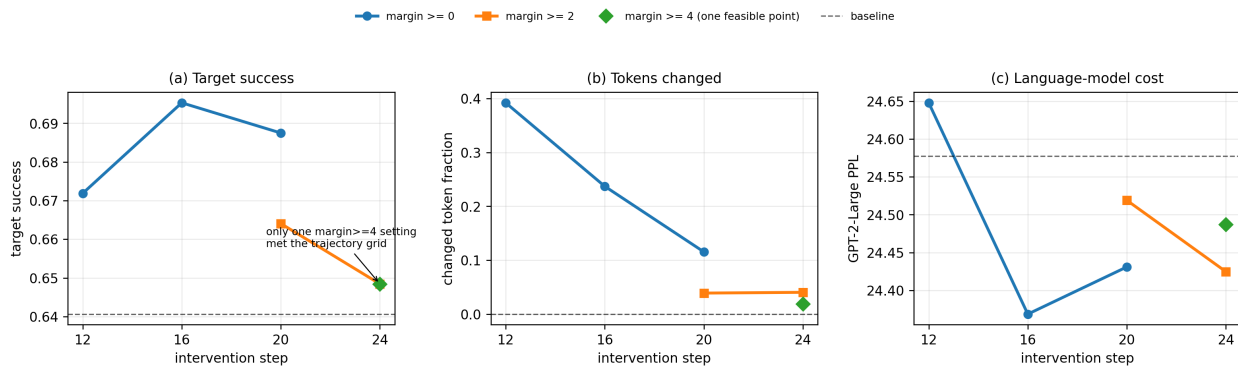


Figure S11: Trajectory-level BCD repair. Left: target sentiment success when the decoder-gradient intervention is applied at steps 12, 16, 20, and 24. Middle: fraction of tokens changed relative to the unedited decode. Right: GPT-2-Large PPL of the edited outputs; dashed lines mark the unedited baseline. Earlier intervention can slightly improve the target classifier at similar PPL, but the gain comes from changing a substantial fraction of tokens. Late or margin-conservative interventions are absorbed by the basin.

Layer-wise decoder-basin sweep. For T5 [51], we extract layers 0–6 and the final hidden state, normalize them using ELF’s latent mean and standard deviation, and decode them with ELF’s native decoder at several corruption levels. For BERT [12], RoBERTa [36], and GPT-2 [50], we use each model’s native LM head instead of cross-decoding through ELF. GPT-2 hidden states predict the next token, so same-position recovery is treated as a negative-control sanity check rather than a fair encoder ranking.

PPL evaluation. GPT-2-Large [50] PPL is computed with fixed truncation length 1024, using per-sample negative log likelihoods and token counts. We report corpus-level PPL from aggregated NLL rather than averaging per-sample PPL. Per-sample PPL is used only for scatter plots and Spearman correlations.

Long-form topic audit. The long-form boundary audit uses 1000 OpenWebText reference samples with at least 200 words, 1000 ELF-B SDE64 samples, 1000 ELF-B SDE32 samples, 512 available ELF-B ODE32 samples, 1000 MDP-B 32k linear-readout samples, and 1000 ZSBD-B 16k lookup samples. We split each document into sentence-like spans with a punctuation-and-capitalization heuristic, discard spans shorter than five words, and keep at most the first 32 spans. Each span is embedded with a locally stored sentence-embedding model using mean pooling over the final hidden states followed by L2 normalization, following the Sentence-BERT protocol [52]. We then report adjacent-sentence cosine, first-to-last sentence cosine, embedding dispersion, and the fraction of adjacent transitions below the 5th percentile of the OWT adjacent-cosine distribution. These metrics are used only as boundary diagnostics for document-level topic drift; they are not a replacement for human evaluation or task-specific discourse metrics.

MAUVE and reference distribution metrics. MAUVE [49] is computed on generated samples against OpenWebText [15] reference samples using a GPT-style feature extractor. JS divergence is computed over token unigram distributions. Both metrics are complementary rather than decisive: MAUVE is sensitive to sample count and feature choice, while token JS captures only shallow distributional shifts.

Decoder calibration. For learned decoder baselines, we generate final ELF latents, split them into train and held-out subsets, and train small token-level decoders to imitate the official decoder’s argmax tokens. We evaluate official decoder, direct unembedding, learned linear decoder, two-layer MLP decoder, and three-layer MLP decoder. Entropy-matched variants sample from small decoders at a temperature chosen to approach the official decoder’s logit entropy.

Decoder margin analysis. For each final latent h and official token i , we compute the margin between the logit of i and the largest competing logit. We then corrupt h with increasing noise and measure positive-margin fraction and token recovery. A subset of token positions is also used for a first-order boundary estimate $m/\|\nabla_h(g_i - g_j)\|_2$, where j is the strongest competitor. This estimate is not an exact distance for the nonlinear contextual decoder, but it makes Theorem 1 operational and reveals whether many tokens are close to a decision boundary.

Decoder-noise training ablation. We used the official PyTorch ELF training pipeline to train short ELF-B ablations on four RTX 3090 GPUs. We varied only the decoder-input noise scale in the decoder branch, keeping architecture, data path, and training length fixed. The basin evaluation uses held-out T5 latents and the native decoder from each checkpoint. For a fair noisy-basin comparison, we report both absolute token recovery at each corruption level and retention relative to the checkpoint’s own clean recovery.

Decoder-branch frequency ablation. We also vary the decoder-branch probability while fixing the decoder-input noise scale at 5. This separates decoder-basin learning from flow learning. The pure-denoising run has no CE branch and therefore cannot decode. The decoder-only run has no L2 branch and therefore cannot learn the transport task, even though its synthetic corrupted-latent basin is broad. Intermediate settings test how much decoder exposure is needed to form a robust native interface.

Explicit margin-loss ablation. We add a hinge-style penalty on the gap between the correct-token logit and the strongest competing logit in the decoder branch, using weights 0.05 and 0.10 with the official-like decoder-input noise scale 5 and decoder-branch probability 0.2. The goal is not to propose a new training recipe, but to test the natural hypothesis that the fragile margin tail can be repaired by directly maximizing logit margins. The evaluation uses the same basin sweep as the decoder-noise ablation.

10k margin-loss extension. Because a short 5k run could understate the effect of the margin objective, we extend the official-like baseline and the 0.10 margin-loss run to 10k steps. Both use the same OWT data path, global batch size, optimizer, decoder noise scale, and decoder branch frequency. The 10k comparison is evaluated with raw weights and the same 1024-sample basin sweep. This extension tests whether the direct margin penalty eventually becomes a basin-widening objective once clean decoding and CE loss have improved.

PCA controlled degradation. For the PCA bottleneck experiment, we fit PCA on contextual T5 latents from OpenWebText, project to ranks $r \in \{512, 256, 128, 64, 32\}$, and reconstruct back to the native 512-dimensional ELF

interface. Decoder diagnostics are computed on held-out clean T5 latents. Generation uses the official ELF-B SDE sampler with either a final-only bottleneck or an every-step bottleneck. This experiment intentionally keeps the checkpoint fixed; it tests whether the diagnostic flags a controlled interface failure without retraining.

Cola-DLM boundary tests. The Cola-DLM experiments use the released VAE and DiT components only to probe interface behavior. The key test corrupts clean VAE latents as $z_t = tz + (1 - t)\epsilon$ and decodes them with the native VAE decoder. The resulting recovery curve measures the width of the decoder-compatible basin, not the full quality of Cola’s trained prior. We also run a balanced DiT trajectory audit on four RTX 3090 GPUs: classifier-free guidance (CFG) [20] values 0/1/3/7 each use 512 OpenWebText samples, 16 Euler steps, prefix length 16, block size 16, and batch size 64. The batch-size probe reached out-of-memory (OOM) at 128 and used about 18GB/GPU at 64. The audit records decoder entropy, decoded-token change, token recovery to the held-out target block, and latent cosine to the held-out target latent. These target metrics are teacher-forced diagnostics; low target recovery is not a failure of free generation, but a boundary showing that Cola’s DiT enters a decoder-confident basin without reproducing the next block’s teacher tokens, precisely the interface gap predicted by the margin-basin diagnostic: decoder confidence and ground-truth token alignment are distinct signals.

C Additional Objective Metrics

Training-free and decoder-calibration controls. The first appendix figures in this section document why the main text treats simple interventions as probes rather than mature methods. Figure S12 collects the one-line controls that use late clean-prediction averaging, margin-aware temperature, and shuffled-margin baselines. Figure S13 gives the corresponding decoder-calibration view: learned readouts can move PPL, entropy, and agreement in different directions, so a low PPL point is not by itself evidence of a faithful interface. Together, the two figures justify the paper’s restraint: the trajectory and margin signals are information-bearing, but local post-hoc rules and low-PPL learned decoders are not reliable replacements for the native denoising/decoding interface.

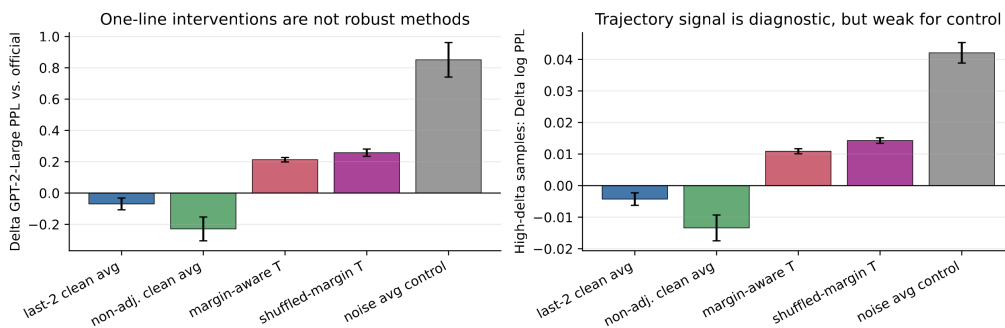


Figure S12: Training-free one-line controls across four runs. Left: late clean-prediction averaging produces small smoothing gains, while averaging with initial noise fails. Right: separating high-delta from low-delta samples shows that the trajectory signal is diagnostic, but margin-aware temperature is no better than a shuffled-margin control. The diagnostic signals are real; local rules alone are not robust samplers.

Sampler metric frontiers. The next group of figures records objective frontier behavior that would be hidden by a single PPL table. Figure S14 pairs PPL with repeated n-gram statistics, Figure S15 and Figure S16 show how sampler noise and schedule choices move along quality-diversity frontiers, and Figure S17 adds a reference-distribution distance axis. Figure S18 then separates readable intermediate samples from final-token basin compatibility. The shared lesson is that a sampler change should be interpreted as a movement on several coupled frontiers, not as a scalar improvement unless PPL, diversity, repetition, reference distance, and decoder compatibility move coherently.

Training-side basin checks. The final group supports the training-side discussion in Section 5.13. Figure S19 shows that decoder-input noise widens the noisy-latent basin; Figure S20 separates decoder exposure from transport learning; Figure S21, Figure S22, and Figure S23 show that our tested scalar margin penalty does not replace noisy decoder training in this short-run setting, and the baseline noisy-CE recipe remains the more effective practical choice. The insight is not that margin is irrelevant, but that basin widening is a neighborhood-training problem: the decoder must see the kind of corrupted states the denoiser will visit, whereas a blunt per-token margin penalty can optimize a visible logit gap without producing the widest usable off-clean basin.

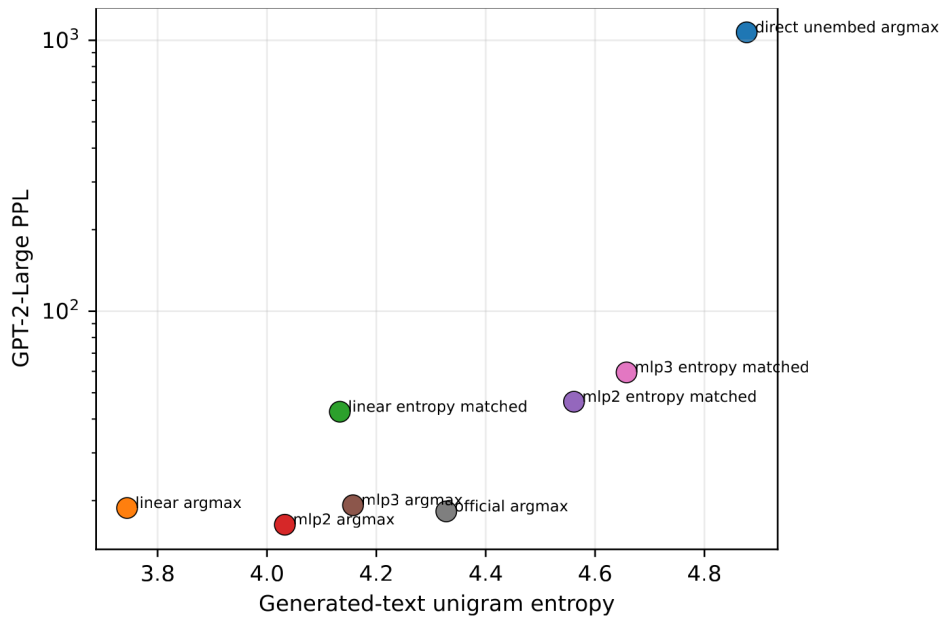


Figure S13: Large matching-set decoder calibration. Each point is a decoder variant evaluated by generated-text unigram entropy on the x-axis and GPT-2-Large PPL on the y-axis. Labels distinguish argmax and entropy-matched variants. Small decoders can reduce PPL, while PPL, entropy, and agreement to the official decoder move independently.

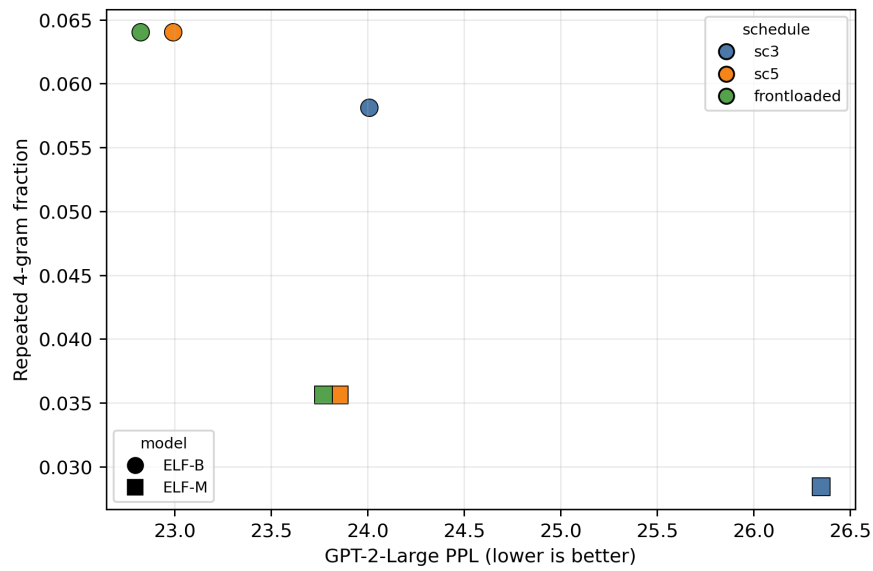


Figure S14: PPL–repetition trade-off. Each point is a sampler setting, with marker shape indicating model size and color indicating the self-conditioning schedule. The plot pairs GPT-2-Large PPL with repeated 4-gram fraction, showing that lower PPL is not automatically better if it is obtained by moving toward repetitive or low-diversity text.

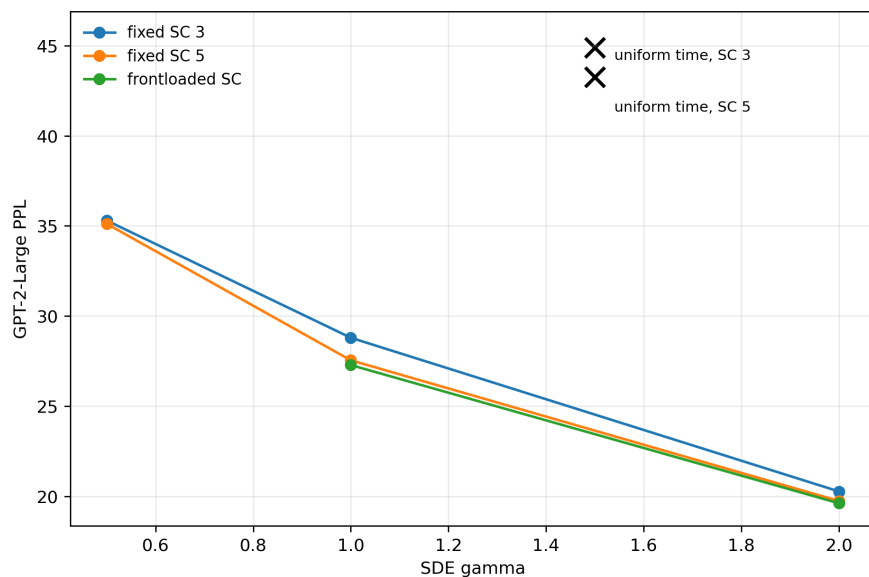


Figure S15: SDE gamma and time-schedule sweep. The curves vary sampler noise strength under fixed self-conditioning schedules, while the black crosses mark uniform-time controls. Gamma and schedule jointly control PPL rather than acting as a single monotone quality knob.

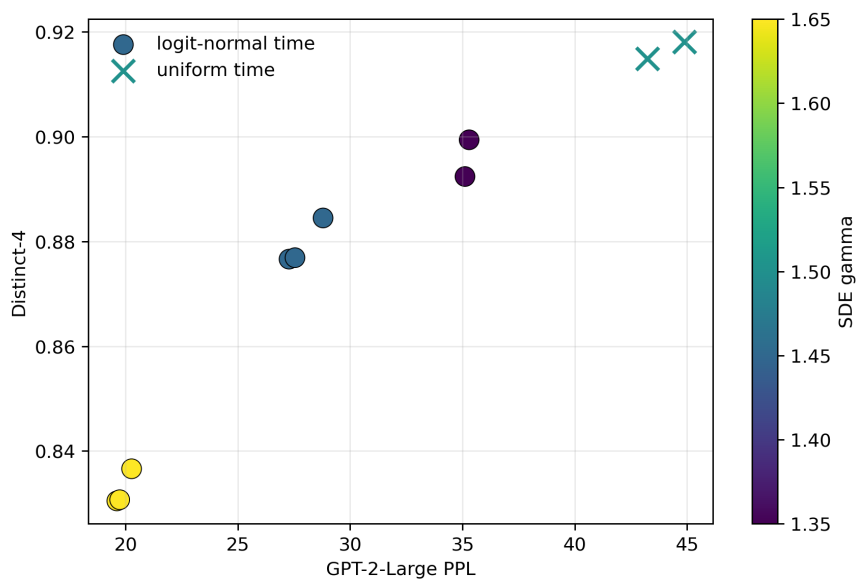


Figure S16: Gamma diversity frontier. Each point is a sampler configuration, colored by SDE gamma and marked by time schedule. Higher gamma can lower PPL while moving distinctness and repetition; the improvement should therefore be read as a frontier movement, not a free quality gain.

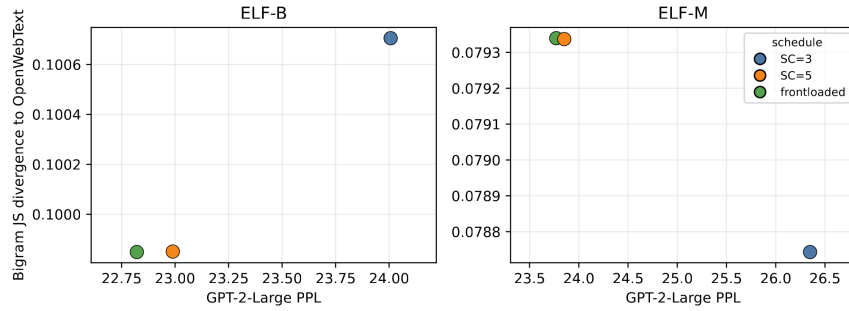


Figure S17: Reference-distribution distance. Left: ELF-B schedules plotted by GPT-2-Large PPL and bigram JS divergence to OpenWebText references. Right: the same diagnostic for ELF-M. This adds another objective frontier axis beyond fluency and diversity.

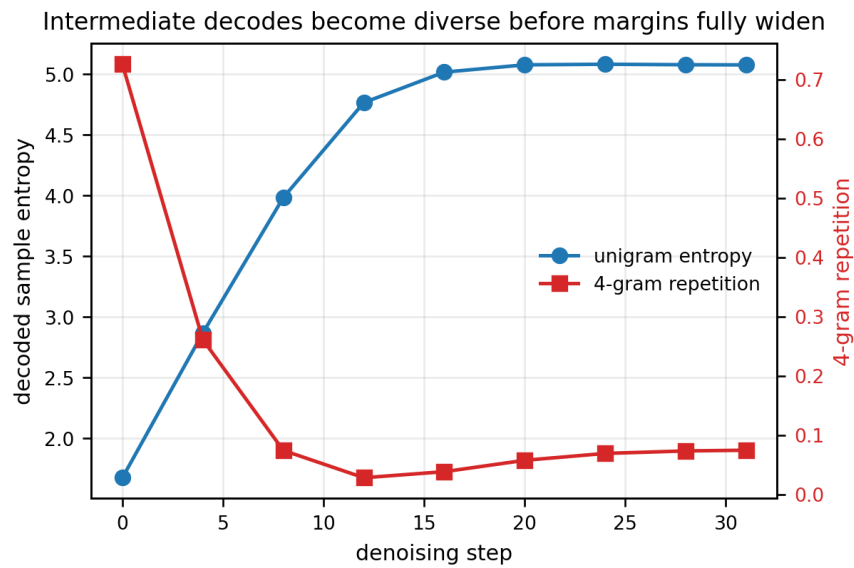


Figure S18: Intermediate decode readability. Decoded sample entropy rises and repetition collapses before the trajectory fully enters the final-token margin basin, showing that readability and basin compatibility are distinct.

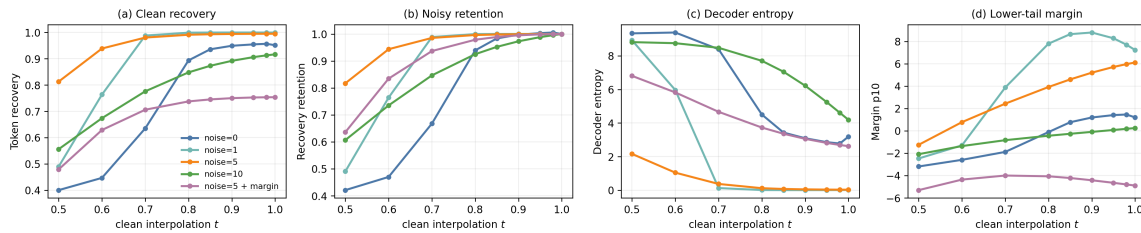


Figure S19: Official implementation decoder-noise training ablation on four RTX 3090 GPUs. The panels report (a) clean token recovery, (b) noisy-latent retention relative to each checkpoint's clean recovery, (c) decoder entropy, and (d) lower-tail native margin as the decoder-input noise scale changes. Clean-only decoder training attains high clean recovery but a narrow noisy-latent basin. An official-like decoder-input noise scale preserves clean recovery while greatly widening mid-noise retention; too much noise is non-monotonic and weakens the interface again.

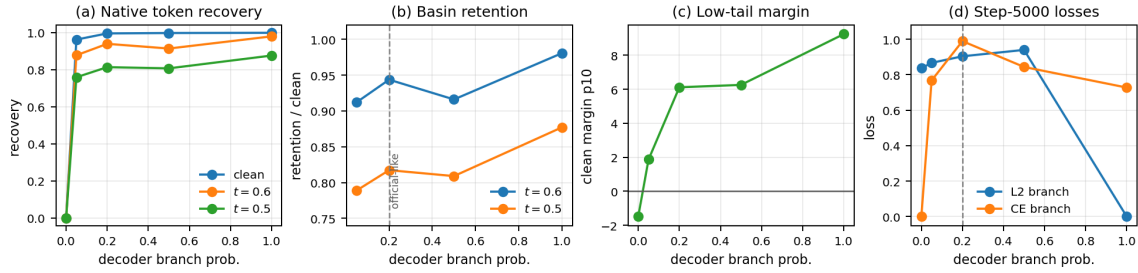


Figure S20: Decoder-branch frequency ablation with fixed decoder-input noise. From left to right, the panels report native token recovery, noisy-basin retention, lower-tail margin, and L2/CE branch losses. Pure denoising does not learn a token interface, while decoder-only training creates a broad synthetic basin but removes the flow objective. The official-like mixed objective balances transport competence and decoder-basin widening.

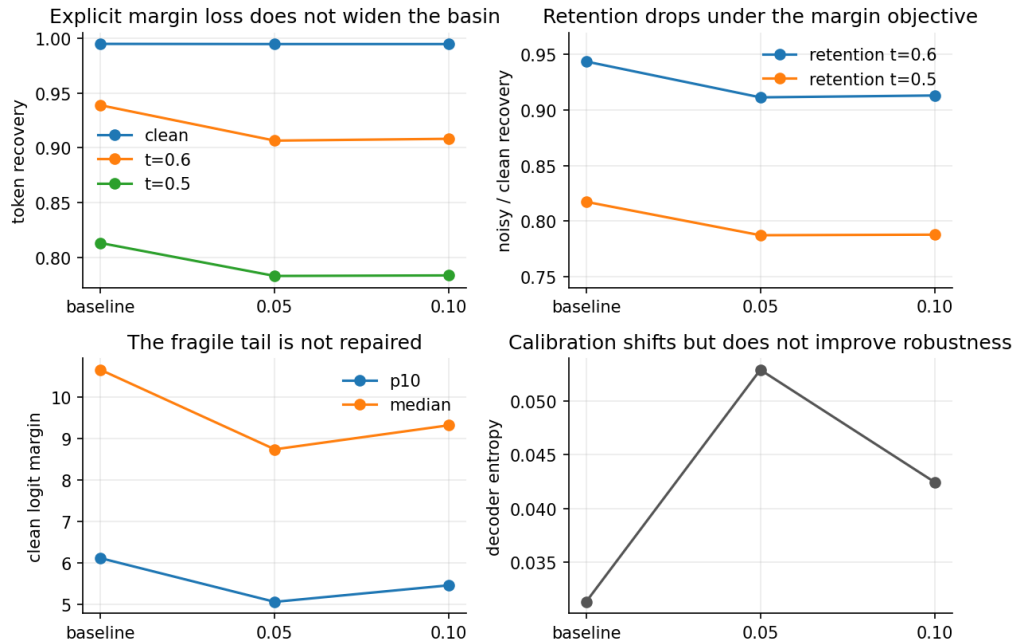


Figure S21: Explicit margin-loss ablation. Top-left: clean and corrupted token recovery. Top-right: noisy-latent retention normalized by clean recovery. Bottom-left: clean lower-tail and median margins. Bottom-right: decoder entropy. In this short ELF-B run with the official implementation, the tested scalar margin penalty preserves clean recovery but lowers retention under corruption and reduces the margin tail relative to the noisy-CE baseline.

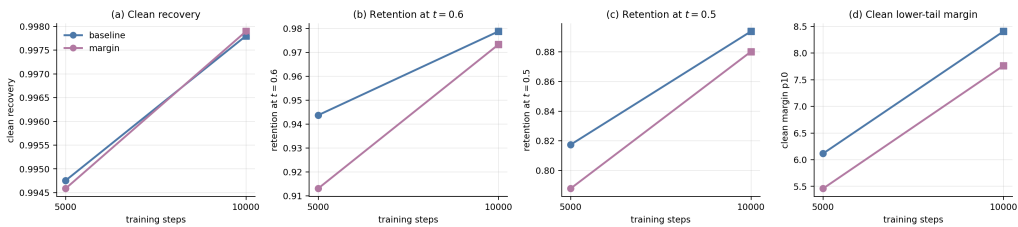


Figure S22: 10k extension of the explicit margin-loss ablation. From left to right, the panels track clean recovery, retention at $t = 0.6$, retention at $t = 0.5$, and clean lower-tail margin as the short-run margin experiment is extended. Longer training narrows the 5k gap, but the margin-loss run still does not beat the noisy-CE baseline on noisy-latent retention or the clean margin tail. In this limited setting, the tested scalar margin penalty is not a drop-in substitute for decoder-input-noise basin training.

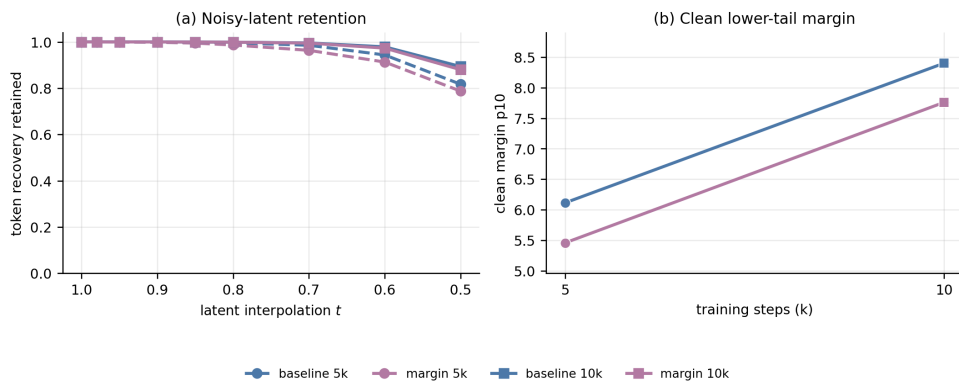


Figure S23: Zoomed basin-retention and margin check for the same 5k and 10k margin-loss extension shown in Figure S22. Left: token-recovery retention under the full latent-corruption sweep, normalized by each checkpoint’s clean recovery; this panel expands the selected $t = 0.6$ and $t = 0.5$ snapshots in the previous figure. Right: clean lower-tail decoder margin for the same objectives. Extending the margin-loss run improves its noisy-latent retention over the 5k version, but the official-like noisy-CE baseline remains the wider decoder-compatible basin.

D Full Diagnostic Heatmap

Figure S24 is the full diagnostic heatmap behind the compact readiness discussion in the main text. It shows all candidate state spaces and controls under the same axes, making clear which failures are denoising failures, which are linguistic-recovery failures, and which are decoder-interface failures. Figure S25 gives the companion Cola-DLM trajectory boundary audit: stronger guidance enters a low-entropy decoder-confident basin, but this basin is not the teacher target basin measured by held-out token recovery, highlighting the gap between decoder confidence and ground-truth alignment. Taken together, these two appendix figures state the scope boundary most explicitly: the diagnostic is not an ELF-only scorecard, but it also does not turn every external system into independent proof of ELF’s mechanism.

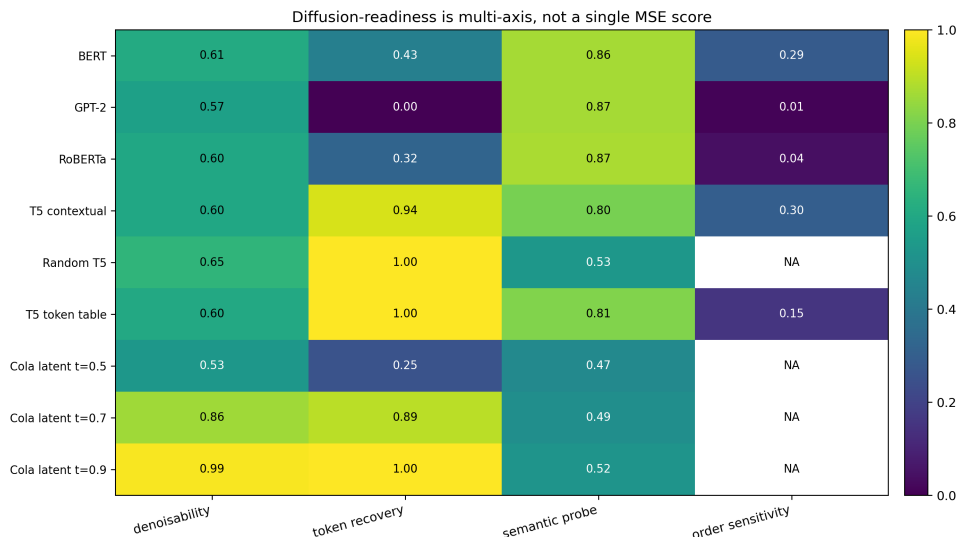


Figure S24: Detailed readiness heatmap across encoders and Cola latents. Rows correspond to candidate state spaces or controls; columns report denoisability, semantic recovery, order sensitivity, decoder-facing compatibility, and trajectory reliability. The heatmap is the appendix version of the readiness protocol summarized in the main text.

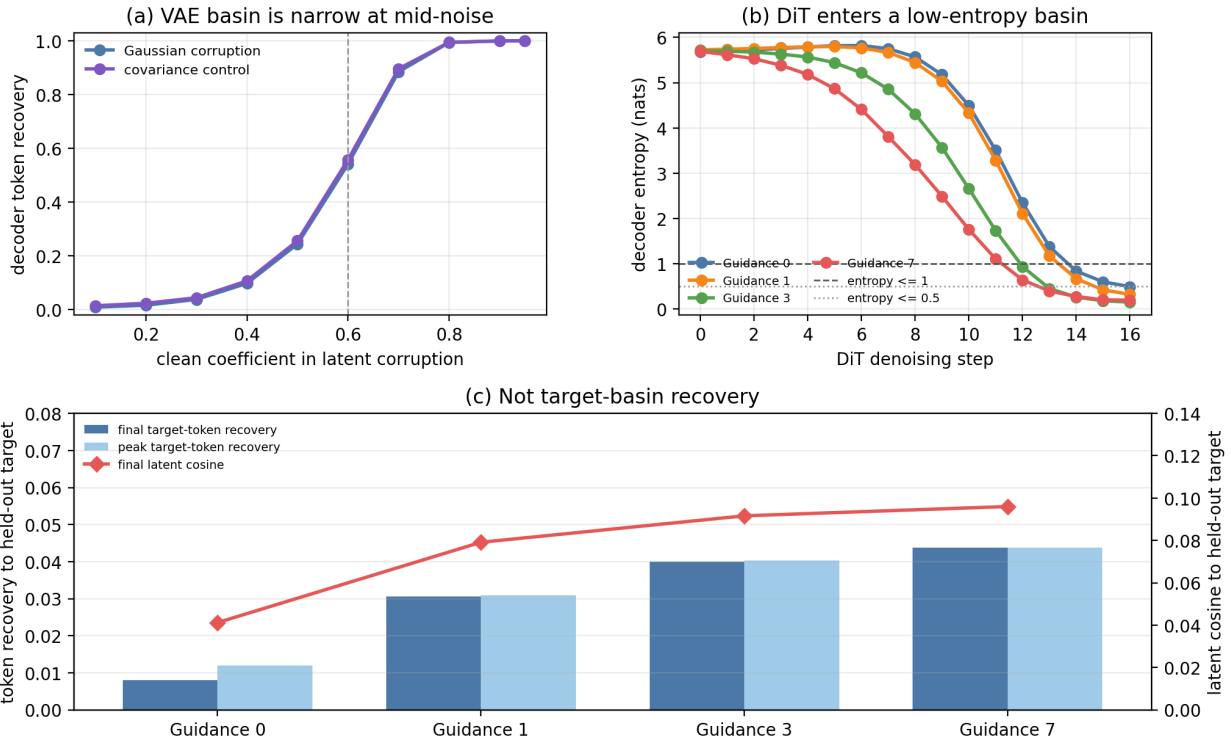


Figure S25: Balanced Cola-DLM boundary audit. Left: clean VAE latents decode reliably, but token recovery collapses under mid-noise corruption. Middle: the DiT prior transports noisy block latents into a low-entropy decoder-confident basin, with stronger guidance entering earlier. Right: final and peak recovery to the held-out target block remain below 5%, while latent cosine to the held-out target stays small; the trajectory reaches a decoder-confident basin, not the teacher target basin.